Hyperspectral Imaging Applications in the Mining Industry: Refining Alteration Footprints

by

Philip Lypaczewski

A thesis submitted in partial fulfillment of the requirements for the degree of

Doctor of Philosophy

Department of Earth and Atmospheric Sciences

University of Alberta

Abstract

The mining industry generates vast amounts of geological material and diamond drill core throughout the life-cycle of any exploration or mining project. This material needs to be examined, logged, and assayed where appropriate. Currently this is generally performed through visual observations by professional geologists. However, as hydrothermal alteration often produces fine-grained alteration, it may be difficult to correctly identify mineralogy with the unaided eye. Geological descriptions are therefore relatively subjective, as differences may exist between geologists investigating the same material.

Hyperspectral imaging is a spectroscopic method that acquires reflectance spectra of a sample in a spatially contiguous manner, generating high-resolution imagery (e.g., at 1 mm/pixel) of a target sample. Reflectance spectra can be used to uniquely identify mineralogy, and in some cases can also provide information on mineral chemistry. In this thesis, the use of hyperspectral imaging is investigated, with emphasis on practical applications to the mining industry. Three specific research areas are examined: 1) the spectral response of biotite and chlorite is investigated for pure samples, and correlations are established to their respective mineral chemistries, 2) applied use of hyperspectral imaging is investigated at the Canadian Malartic disseminated gold deposit, with emphasis on vectoring towards mineralization using spectral parameters, and 3) applied use of hyperspectral imaging is investigated at the Highland Valley Copper porphyry deposits, with emphasis on detection of mineralized sample, which would allow for efficient ore-sorting.

In Chapter 2, shortwave infrared (SWIR, 1000-2500 nm) reflectance spectra of biotite and chlorite are investigated to establish quantitative relationships between spectral metrics and

mineral chemistry, determined by electron microprobe analysis (EMPA). Samples spanning a broad range of mineral compositions are used to establish regression equations to Mg#, which can be estimated to ±3 and ±5 Mg#, and to Al^{VI} content, which can be estimated to ±0.044 Al^{VI} (11 O) and ±0.09 Al^{VI} (14 O), respectively for biotite and chlorite. As both minerals have several absorptions at common positions (1400, 2250, 2330 nm), spectral interference may occur in mineral mixtures. For an equivalent Mg#, absorptions of chlorite are offset to 1-15 nm higher wavelengths relative to those of biotite. If the incorrect mineral is identified, errors in the estimation of composition may occur. Recommendations to mitigate these issues are presented.

In Chapter 3, applied use of hyperspectral imaging is investigated at the Canadian Malartic gold deposit, located in the Abitibi region of Québec, Canada. High-resolution hyperspectral imagery (0.2-1.0 mm/pixel) in both shortwave infrared (SWIR, 1000-2500 nm) and longwave infrared (LWIR, 8000-12000 nm) is acquired for over two thousand meters of drill core and is used to visualize changes in mineralogy and mineral chemistry related to metamorphism and hydrothermal alteration. Unaltered metasedimentary rocks contain metamorphic white mica with Al^{VI} contents varying between 1.90 and 1.75 apfu (2195-2203 nm), depending on metamorphic grade. Hydrothermal alteration is characterized by white mica which becomes progressively more phengitic with increasing alteration intensity, with Al^{VI} contents ranging from 1.70 to 1.50 apfu (2204 to 2212 nm). LWIR hyperspectral data is used in drill core to estimate the degree of silicification, and was generally in good agreement with the silicification abundance estimated by core logging.

In Chapter 4, applied use of hyperspectral imaging is investigated at the Highland Valley Copper (HVC) district in British Columbia, Canada. Hyperspectral imagery is acquired on 755 rock samples and several hundred meters of continuous drill core. Simple spectral metrics

(absorption depths and spectral slopes) are utilized to identify and quantify the relative abundance of 12 minerals commonly present in HVC samples. Coarse-grained white mica occurs as vein selvages and is closely associated with mineralization, and can regionally be detected up to 4 km away from the deposits. Kaolinite is present within 2 km of the mineralized centers, but does not necessarily occur within strongly mineralized intervals. Prehnite occurs as veinlets and vein selvages and is ubiquitous 4 to 8 km from the deposits. Prehnite is the most distant spectrally detectable alteration mineral, and may serve as an effective pathfinder mineral towards mineralized centers. A simple and easily adjustable spectral alteration score based on the presence or absence of a set of minerals could serve as a vector towards mineralization on regional scales.

Preface

This thesis is part of the Natural Sciences and Engineering Research Council (NSERC)-Canadian Mining Innovation Council Mineral (CMIC) Footprints project, which ran between April 2013 and March 2019 and involved over 80 professors, researchers and students working on a common sample suite from Canadian mine sites (https://cmic-footprints.laurentian.ca/). In this thesis, hyperspectral imagery is acquired for samples from the disseminated Au (Canadian Malartic) and porphyry Cu (Highland Valley Copper) subprojects, totaling over 1250 samples and over 2400 meters of drill core. A number of additional mineral samples (crystals) were selected from various sources to investigate the spectral response of pure minerals (Chapter 2). At the Au site (Chapter 3), all field samples were collected and investigated by myself and the Footprints team, and an additional two thousand meters of drill core were selected exclusively for this thesis. At the Cu site (Chapter 4), all field samples were collected by Guillaume Lesage, Kevin Byrne and Mike D'Angelo during their respective research, and were sent for hyperspectral analysis as part of the Footprints project. An additional 400 meters of drill core was selected exclusively for this thesis. All hyperspectral data analysis was performed by myself. Three papers (two published to date) result of this thesis:

Chapter 2 has been published as: Lypaczewski, P. and Rivard, B., 2018. Estimating the Mg# and Al^{VI} content of biotite and chlorite from shortwave infrared reflectance spectroscopy: Predictive equations and recommendations for their use. International Journal of Applied Earth Observation and Geoinformation, 68, pp.116-126.

Chapter 3 has been published as: Lypaczewski, P., Rivard, B., Gaillard, N., Perrouty, S., Piette-Lauzière, N., Bérubé, C.L. and Linnen, R.L., 2019. Using hyperspectral imaging to vector towards mineralization at the Canadian Malartic gold deposit, Québec, Canada. Ore Geology Reviews, 111, p.102945.

Chapter 4 will be submitted for publication as: Lypaczewski, P., Rivard, B., Lesage, G., Byrne, K., D'Angelo, M., Lee, R., G., Characterisation of mineralogy in the Highland Valley porphyry Cu district using hyperspectral imaging, and potential applications.

Acknowledgements

I would in a first place like to offer my sincerest thanks to my supervisor, Dr. Benoit Rivard for in a first place having allowed me to initiate research with a world-class instrument, and for his continued support, guidance and patience during this long-overdue, nearly 6 years in the making Ph.D. Particular thanks to Dr. Jilu Feng, who has provided guidance and assistance in data acquisition, particularly at the initial stages of my then M.Sc., as well as to Dr. Iman Entezari, who has greatly helped during data acquisition.

As this research was part of a large, multi-institution research project (NSERC-CMIC Footprints) involving two mine sites and a total of over 80 researchers, not all can be named, but I am grateful for the participation of all. Particular thanks to Dr. Robert L. Linnen, Dr. Stéphane Perrouty and Dr. Nicolas Gaillard on the Canadian Malartic site, and to Dr Robert Lee, Dr. Guillaume Lesage and Dr. Kevin Byrne on the Highland Valley site for insightful discussions on all aspects of geology. I also wish to acknowledge the support of the Canadian Malartic mine staff, particularly François Bouchard, Kayla Helt, Carl Corriveau, Matthieu Dessureault, and Alain Hébert who have provided tremendous support during field work, and to staff at Teck Resources Limited for providing access to the mine site and the drill core database. Special thanks to Dr. Carl Guilmette at Laval University who has allowed me access to facilities during my time in Quebec City. I am grateful for the help of Professor Jeanne Paquette of McGill University, Andrew Locock, Lisa Budney and Marilyn Huff of the University of Alberta for access to samples. Funding for this study was provided by the Natural Sciences and Engineering Research Council of Canada (NSERC) and the Canadian Mining Innovation Council (CMIC) through the NSERC Collaborative Research and Development Program.

Table of Contents

List of Tables

List of Figures

List of Appendices

Glossary of Terms

Al^{IV}: Al in tetrahedral coordination. Not directly linked to OH^- groups in phyllosilicates.

Al^{VI}: Al in octahedral coordination. Directly linked to OH^- groups in phyllosilicates, affecting their spectral response.

Apfu: Atoms per formula unit, used to highlight the stoichiometry of a given mineral.

Combination (absorption): Absorption that results of the addition of two or more fundamental absorptions. The resulting frequency (wavenumber) is the sum of the fundamental absorptions.

Continuum (spectrum): The overall shape of the spectrum, which can be approximated by fitting a convex hull over the entirety of the spectrum. Used for continuum removal.

EPMA: Electron probe micro-analyzer, an instrument used for the quantitative chemical analysis of minerals.

Line-scanning camera: Image acquisition device that generates images by contiguously acquiring and stitching thin (e.g., 1 mm) images of a sample.

LWIR: Longwave infrared (generally 8000 to 12000 nm)

Mg#: Molar Mg/[Mg+Fe].

MWIR: Midwave infrared (generally 3000 to 5000 nm)

Muscovitic (white mica): White mica nearing muscovite compositions, with Al^{VI} contents nearing 2.0 apfu, and presenting low absorption wavelengths (near 2195 nm).

Overtone (absorption): Absorption at a frequency that is an integral multiple of the fundamental frequency, in wavenumbers.

Phengitic (white mica): White mica (muscovite) showing some extent of Tschermack substitution, towards aluminoceladonite compositions. Contains lower Al^{VI} than pure muscovite, and presents longer absorption wavelengths (near to 2215 nm).

SNR: Signal-to-noise ratio, the ratio of signal over the noise, where higher numbers indicate better quality data.

SWIR: Shortwave infrared (generally 1000 to 2500 nm)

VNIR: Visible and near infrared (generally 400 to 1000 nm)

White mica: Any of the dioctahedral micas, including paragonite, muscovite, margarite (i.e., with interlayer occupancy ≈ 1 apfu), and illite (with an interlayer occupancy <0.85 apfu).

Chapter 1 - Introduction

1.1 Context for hyperspectral imaging of drill core

The mining industry generates vast amounts of diamond drill core throughout the life-cycle of any mining project. Drilling, however, is an expensive and time-consuming task. In easily accessible regions (e.g., Abitibi, Québec) drilling costs average $140 per meter in an exploration environment, decreasing to $100 per meter in a production environment (Institut de la statistique du Québec, 2019). In 2018, in the province of Québec alone, the mining industry has generated over 2.3 million meters of drill core, which needs to be examined, logged, and assayed where appropriate. Drill core logging is generally performed though visual observations by professional geologists, at significant additional costs. Hydrothermal alteration near several types of ore deposits, however, often produces fine-grained alteration mineralogy that may be difficult to correctly identify with the unaided eye. Core logging is therefore often a subjective task, as it involves some degree of interpretation, and differences may exist between geologists logging the same core.

Hyperspectral imaging is a spectroscopic method that acquires reflectance spectra of a sample in a spatially contiguous manner, generating high resolution imagery (e.g., at 1 mm/pixel) of a target sample. Every pixel of a hyperspectral image contains a reflectance spectrum, which in this study spans the shortwave infrared (SWIR, 1000-2500 nm) and longwave infrared (LWIR, 8000-12000 nm) regions. In SWIR reflectance spectra of hydrated minerals commonly present in hydrothermally altered rocks, cation-OH bonds produce characteristic absorption features that can be used to uniquely identify several minerals (Hunt, 1977; Clark et al., 1990). In many cases, the exact position of specific absorptions can also be used to estimate mineral chemistry. Unlike conventional analytical techniques (e.g., electron microprobe), SWIR reflectance spectroscopy is not negatively impacted by the fine-grained (micron-sizes) nature of alteration mineralogy (Hunt and Salisbury, 1970), and is therefore an ideal tool for the rapid identification and characterization of alteration zones in hydrothermal systems. The LWIR range is used in limited portions of this thesis to identify minerals that are spectrally inactive in the SWIR. Because hyperspectral imagery can be acquired from rock surfaces in seconds, and requires no sample preparation, spectral datasets can be far more extensive than datasets obtained using conventional analytical techniques. Complete drill core boxes (containing up to 4.5 meters of core) can be scanned using commercially available hyperspectral imagers in under 90 seconds, at a resolution of 1 mm/pixel. Entire drill holes (hundreds to thousands of meters of drill core) can therefore be scanned, analyzed, and quantified with turnaround times conducive to uptake of this technology by the mining industry.

1.2 Reflectance spectroscopy of minerals

Research in reflectance spectroscopy of minerals has been ongoing since at least the early 1960's, and a thorough understanding of the spectral response of common minerals was developed and summarized in the seminal Hunt (1970) and subsequent papers. Much of these early spectral datasets are available online in a spectral library maintained by the United States Geological Survey (USGS) (Kokaly et al., 2017).

In reflectance spectra of minerals, absorption features are caused by two distinct processes, namely electronic processes or vibrational processes. In electronic processes, broad absorption features are produced (several hundred nm in width), and result from direct interaction between photons and electrons of a given atom. In common geological materials, these absorptions are mainly caused by Fe^{2+} or Fe^{3+}, and mostly appear in the lower wavelength regions from 400 nm to 1000 nm (Hunt, 1977). These processes are not investigated in this thesis.

Vibrational processes, on the other hand, produce absorptions features resulting from interactions with molecular bonds in minerals, such as the OH^- or the Si-O bond (Hunt, 1977; Clark et al., 1990). These absorptions typically occur at longer wavelengths, and are generally narrow and well defined (<100 nm in width). Because they are affected by both the nature of the atoms forming the bond (e.g., Al-OH vs. Mg-OH), as well as by the local crystal structure of the mineral, vibrational absorptions can in many cases be used to uniquely identify mineralogy, and in some cases can be used to estimate mineral chemistry (Vedder 1964; Farmer 1968; Hunt 1970; Besson and Drits 1997a; Besson and Drits 1997b).

Vibrational absorptions that arise from the OH^- bond in hydrated minerals are commonly investigated in infrared studies of minerals. Two types of fundamental vibrational motions can occur from this bond; a fundamental stretching motion (denoted υOH) and a fundamental bending motion (δOH). For each of these motions, overtones can occur at integral multiples of their fundamental energy (e.g., 2υOH, 3υOH, etc.), with each overtone being progressively weaker in intensity. Combinations can occur when multiple types of motions combine, for example υOH+ δOH, with each combination also being much weaker in intensity than its constituent fundamentals (Vedder, 1964; Farmer, 1974; Hunt, 1977; Clark, 1990). Depending on the specific cations forming the bond, as well as the surrounding mineral structure, most hydrated minerals have their fundamental stretching frequencies (υOH) between 2600-3000 nm, and fundamental bending frequencies (δOH) between 10500-16700 nm, as summarized in Farmer (1974). That is, all fundamental absorptions of minerals occur either in the midwave infrared (MWIR) or longwave infrared (LWIR) ranges, which to date remain relatively sparsely studied in hyperspectral imaging studies. In the commonly investigated SWIR range, all absorption features are therefore overtones or combinations of the fundamentals occurring at longer wavelengths. In phyllosilicates, ubiquitous in hydrothermally altered rocks, the main observed absorptions are the first overtone of the OH- stretch (2υOH), occurring between 1330-1470 nm, and various combination features (υOH+ δOH) occurring between 2100-2500 nm (Farmer, 1974; Beran, 2002). For white mica, a major combination feature occurs near 2200 nm, but its exact position varies with Al^{VI} content, from 2190 nm for Al-rich (muscovitic) white mica, to 2215 nm for Al-poor (phengitic) white micas (Post and Noble, 1993; Duke, 1994; Swayze et al., 2014). Similarly, a major absorption feature occurs near 2250 nm for biotite and chlorite, and can be used to estimate their respective Mg# (molar Mg/[Mg+Fe]), as the exact position varies from 2240 nm for high-Mg# to 2260 nm for low-Mg# (Besson and Drits, 1997b; Martinez-Alonso et al., 2002; Bishop et al., 2008).

1.3 Applied reflectance spectroscopy

Some of the earlier applied research publications making use of reflectance spectroscopy datasets include McLeod et al. (1987), who investigated changes in chlorite chemistry in a VMS deposit using SWIR point data, and found that chlorite becomes Mg-rich (low-wavelength) near ore zones. Duke (1994) also made use of a large number of SWIR point measurements in an area over 1000 sq. km in size, and mapped changes in the position of the 2200 nm absorption of white mica as a proxy for Al^{VI} content, which reflected changes in metamorphic grade. Numerous researchers have since also investigated the use of SWIR point data at several mineral deposit types, and invariably reported mineralogical or mineral chemical characteristics that could be used to aid exploration. Bierwirth et al. (2002) investigated Archean gold deposits in Western Australia, and reported that ore zones were characterized by pyrophyllite and Al-rich (low-wavelength) white mica. Harraden et al. (2013) acquired a total of 3900 SWIR point measurements from 150 drill holes at the Pebble Cu-Au-Mo porphyry deposit in Alaska, and revealed that Cu mineralization also occurs in association to pyrophyllite and low-wavelength white mica. Line-scanning (but non-imaging) VNIR-SWIR reflectance spectrometers (e.g., the HyLogger instrument) were developed to acquire continuous spectral data on drill core (Schodlok et al. 2016), and intervals of several thousand or tens of thousands of meters have been investigated in numerous studies. Invariably, spectrally detectable changes have been reported near or within ore zones, and can serve as vectors to mineralization (e.g., Arne et al., 2016; Mauger et al., 2016; Wells et al., 2016).

Imaging spectrometers (or hyperspectral cameras) have the added benefit of providing spatial context to spectral measurements. The application of early imaging spectrometers for geological studies has been investigated in Cudahy et al. (2000), who made us of both SWIR and LWIR airborne hyperspectral data to map changes in garnet chemistry near a porphyry-Cu deposit, and showed that it becomes Fe-rich near the deposit. More recently, imaging spectrometers have been adapted for close-range usage, and have been employed to scan drill cores at high-resolution (e.g., 1 mm/pixel). Tappert et al. (2015) made use of both SWIR and LWIR hyperspectral core scanners to investigate 90 m of drill core from the Snap Lake diamond deposit, and reported that hyperspectral data could be used to quantify the amount of crustal dilution in kimberlite, a parameter required for ore processing. Mathieu et al. (2017) made use of SWIR imagery to investigate 16 core samples from the Cigar Lake unconformity-related uranium deposit, and were able to detect changes in alteration mineralogy, as well as textural features such as veining. Several other studies recently presented imaging data from various types of mineral deposits, including from porphyry-Cu deposits (Dalm et al., 2017; Graham et al., 2018), sapphire-bearing marbles (Turner et al., 2017), an orogenic gold deposit (Naleto et al., 2019), and oil sands (Speta et al., 2016).

1.4 Thesis outline

This thesis focuses on the applied use of hyperspectral imaging for the characterization of alteration in geological exploration and production contexts, and is presented as three research chapters published as stand-alone papers. The background context for the thesis is presented in Chapter 1, with the main body of the thesis in Chapters 2 and 3, published in peer-reviewed journals, and Chapter 4 ready for submission. A summary of the research presented in this thesis and possible avenues for future research are presented in Chapter 5.

Extensive research in reflectance spectroscopy of minerals has generated a thorough understanding of spectra of common minerals, but quantitative relationships to mineral chemistry have only recently been established for common minerals in the SWIR. For example, it has been known since at least Vedder (1964) that the mineral chemistry of white mica affects the exact position of its 2200 nm absorption feature, but a quantitative relationship was only reported in 1993 by Post and Noble, and high-quality regression equations were provided in Swayze et al. (2014). Similarly, Roache et al. (2011) recently characterized the spectral response of epidote, and provided regressions between its major 1540 nm absorption and Fe content, and Laukamp et al. (2012) investigated the tremolite-actinolite series, providing regressions to Mg#. Chapter 2 of this thesis therefore develops the spectroscopic knowledge required for the accurate and quantitative analysis of biotite and chlorite mineral chemistry from SWIR spectra, and presents regression equations to both their respective Mg# and Al^{VI} contents.

Chapter 2 has been published as NSERC-CMIC Mineral Exploration Footprints Project Contribution Number 163:

Lypaczewski, P. and Rivard, B., 2018. Estimating the Mg# and Al^{VI} content of biotite and chlorite from shortwave infrared reflectance spectroscopy: Predictive equations and recommendations for their use. International journal of applied earth observation and geoinformation, 68, pp.116-126.

Applications of reflectance spectroscopy to investigate hydrothermal alteration patterns has been demonstrated at various types of deposits, with the most commonly employed metric being the position of the 2200 nm absorption feature of white mica, reflecting its mineral chemistry. Most studies, however, make use of airborne hyperspectral data that provides large-scale data, but at a relatively low spatial resolution on the order of meters/pixel (e.g., Bierwirth et al., 2002; van Ruitenbeek et al., 2006; Laukamp et al., 2011; van Ruitenbeek et al., 2012; Swayze et al., 2014; Laakso et al., 2015), or make use of point data (i.e., a point on the order of 1 cm^2) acquired at regular intervals on drill core or in the field (e.g., typically every 1 meter on core, or every 200 to 500 meters in the field) (e.g., Jones et al., 2005; Biel et al., 2012, Harraden et al., 2013, Laakso et al., 2015). Large amounts of data points acquired in this way can provide information on large-scale mineralogical patterns, but yield limited information on the spatial continuity of alteration on meter-scales, between data points. Data can also be acquired continuously on drill core using line-scanners that provide data continuity (e.g., the HyLogger instrument; Tappert et al., 2011; Arne et al., 2016; Mauger et al., 2016; Wells et al., 2016), but do not provide textural context to the data, and yield limited information on centimeter-scale mineralogical variability, for example between fine sedimentary layers, veins, vein selvages, and host-rocks.

Several recent studies have investigated deposits in various geological settings using imaging spectrometers that provide high resolution (≈1 mm/pixel) hyperspectral data. The resulting imagery allows the examination of mineralogical changes within their petrographic context, which can reveal information that cannot be obtained from non-imaging, point or line-scanning measurements. For example, Speta et al. (2016) acquired high-resolution hyperspectral imagery on 136 meters of oil-saturated drill core, and identified small-scale (cm) sedimentary and biogenic features that were not visible to the naked eye. Although several studies have investigated gold deposits using point data and generally reported changes in white mica chemistry near ore zones (e.g., Arne et al., 2016; Mauger et al., 2016; Wells et al., 2016; Witt et al., 2016; Wang et al., 2017), few studies have made use of hyperspectral imaging, and uncertainties remain as to the scale of alteration near and within ore zone (i.e., the width or extent of white mica alteration in vein selvages, compositional changes between juxtaposed lithologies, etc.). Naleto et al., (2019) is among the few studies presenting hyperspectral imagery for gold deposits, having acquired high-resolution (0.15 mm/pixel) data for 118 field or core samples, and showed that large changes in mineralogy can occur on centimeter-scales.

Chapter 3 of this thesis therefore investigates the Canadian Malartic gold deposit using high-resolution hyperspectral imagery (0.2 to 1.0 mm/pixel), with emphasis on the generation of spectral metrics that can be applied by industry, both for exploration (vectoring towards mineralization) and ore processing (ore-sorting) purposes. As alteration selvages may not fully be captured by thin section-sized samples (2 cm x 4 cm) typically utilized in geological studies, in a first place, high-resolution imagery is acquired for over 500 field and core samples. This serves to determine the full extent of alteration in vein selvages, which may extend over several centimeters to decimeters. Imagery is also acquired at 1 mm/pixel over a series of drill holes totaling 2000 meters of core, and serves to determine the full extent, and continuity of alteration near mineralized intervals. Information obtained from these data serves to determine an appropriate sampling strategy for point data acquisition in the field. Using white mica chemistry from over 1500 SWIR point measurements collected in a 50 km by 15 km area around the deposit, both a large hydrothermal alteration halo and regional metamorphic isograds can be delineated.

Chapter 3 has been published as NSERC-CMIC Mineral Exploration Footprints Project Contribution Number 190:

> *Lypaczewski, P., Rivard, B., Gaillard, N., Perrouty, S., Piette-Lauzière, N., Bérubé, C.L. and Linnen, R.L., 2019. Using hyperspectral imaging to vector towards mineralization at the Canadian Malartic gold deposit, Québec, Canada. Ore Geology Reviews, 111, p.102945.*

In porphyry Cu deposits, mineral zonations generally occur in approximately concentric, well understood patterns (e.g., Seedorff et al., 2005; Sillitoe, 2010). If correctly identified, changes in mineralogy may therefore be used to vector towards mineralized centers. However as alteration often consists of fine-grained assemblages, and alteration is often telescoping, mineralogy can be difficult to identify with the unaided eye. As reflectance spectroscopy is not affected by the fine-grained nature of alteration, it may be an effective tool to characterize these types of deposits. Following the rationale described in the previous chapter, however, point or line reflectance data may not be sufficient to fully describe alteration patterns generated by multiple generations of superposed or crosscutting veins, veinlets and vein selvages.

Chapter 4 of this thesis therefore investigates the use of hyperspectral imaging at the Highland Valley Copper (HVC) district in British Columbia, Canada, again with emphasis on generating metrics useful to industry. Here, high-resolution (0.2-1.0 mm/pixel) SWIR hyperspectral imagery is acquired on 755 rock slabs as well as on several hundred meters of continuous drill core, and serves to, in a first place, identify mineralogy, and to determine the scale and extent of detectable alteration around veins and veinlets. Simple spectral metrics are then developed to quantify the relative abundance of the 12 spectrally detectable minerals present in HVC samples, and a simple and easily adjustable spectral alteration score is developed based on the presence or absence of this set of minerals. In an exploration setting, this alteration score could serve as a vector towards mineralization, while in a production environment, it could serve as an ore-sorting parameter.

Chapter 4 will be submitted for publication as NSERC-CMIC Mineral Exploration Footprints Project Contribution Number 214:

> *Lypaczewski, P., Rivard, B., Lesage, G., Byrne, K., D'Angelo, M., Lee, R., G., Characterisation of mineralogy in the Highland Valley porphyry Cu district using hyperspectral imaging, and potential applications.*

A summary of the thesis, with emphasis on the applied use of hyperspectral imaging in the mining industry, and potential avenues for future research are presented in Chapter 5.

Chapter 2 - Estimating the Mg# and Al^{VI} content of biotite and chlorite from shortwave infrared reflectance spectroscopy: Predictive equations and recommendations for their use

2.1 Introduction

Biotite and chlorite are ubiquitous alteration products in numerous types of hydrothermal ore deposits (MacLean and Kranidiotis, 1987; Sillitoe, 2010). Broad mineralogical zonations can often be defined around hydrothermal centers, and, if correctly recognized as such, can be used to target mineralized areas. In many instances, within each mineralogical zone, the chemistry of a given mineral also varies with alteration intensity. For example, biotite and chlorite in porphyry deposits (Selby & Nesbitt, 2000; Wilkinson et al., 2015), and chlorite in VMS deposits (MacLean and Kranidiotis, 1987) vary in composition with distance to mineralization, and can provide more refined vectors towards mineralization than mineralogical zonations.

Shortwave infrared (SWIR, 1000-2500 nm) reflectance spectroscopy is now commonly used to identify mineralogy in and around mineral deposits, either in the form of point data acquired using portable instruments (e.g., Biel et al., 2012; Harraden et al., 2013), or in the form of hyperspectral imagery acquired using lab-based or airborne hyperspectral sensors (e.g., Laakso et al., 2015; Dalm et al., 2017; van der Meer et al., 2018). Biotite and chlorite absorption positions are often used as proxies to qualitatively describe mineral composition, for example inferring Mg, Mg-Fe, or Fe-rich biotite or chlorite (e.g., Jones et al., 2005; Laakso et al., 2015). Conventional economic geology studies, on the other hand, report precise mineral compositions for given alteration zones. For example, Selby & Nesbitt (2000) report altered biotite in a porphyry-Cu deposit at Mg# 60-75, and background biotite around Mg# 45. Direct links between qualitative compositions derived from hyperspectral data and quantitative mineral compositions in existing studies are therefore difficult to establish, especially in instances where compositional changes are subtle (e.g., <15 Mg#).

For biotite, this stems from the lack of availability of quality regressions between mineral chemistry and SWIR responses. For chlorite, the displacement of absorption positions as a function of Mg# has been partially investigated, with descriptions and regressions reported in McLeod et al. (1987) and King & Clark (1989), but the effect of Al^{VI} content, which strongly influences the spectral response of chlorite, has not been characterised.

The primary goal of this study is therefore to refine the relationships between mineral chemistries (here Mg# and Al^{VI} content) and SWIR responses of biotite and chlorite, which to date exist in a mostly qualitative nature. Calibrated regressions are provided for all absorptions of these two minerals, some of which were not previously reported. For the absorptions that have previously been investigated, improvements in the precision of the regressions are presented, and will allow hyperspectral studies to link estimated mineral compositions to precisely measured compositions as produced by conventional economic geology studies. Finally, pitfalls that can be encountered in the use of such regressions are identified (e.g. in mineral mixtures), and recommendations are made to minimize errors in the prediction of composition.

2.2 Background

2.2.1 Mineral chemistry of phyllosilicates

In biotite ($K(Mg,Fe)_3[AlSi_3]O_{10}(OH)_2$) and chlorite ($(Mg,Fe)_5Al[AlSi_3]O_{10}(OH)_8$), mineral chemistry can vary significantly from end-member composition. The main chemical changes occur for the M-site cations (the octahedral layer), resulting from two substitution mechanisms; simple Mg↔Fe substitution, and a coupled Tschermak substitution ($Al^{IV}Al^{VI} \leftrightarrow Si,(Mg,Fe)$) (Bailey, 1986; Fleet, 2003; Deer et al., 2009). Shortwave infrared (SWIR

1000-2500 nm) absorption features observed in reflectance spectra are caused by OH^- groups that are directly bound to the octahedral layer (Farmer, 1968; Hunt, 1977; Clark, 1990), and are therefore influenced by its composition.

2.2.2 Hydroxyl absorption features in the SWIR

For biotite, numerous studies have investigated the effects of mineral chemistry on reflectance spectra, but focus has been on the longer wavelengths (above 2500 nm, 40-4000cm^{-1}, Vedder, 1964; Redhammer et al., 2000; Beran, 2002). In the SWIR, Post and Crawford (2014) showed a correlation between increasing FeO wt% (although they did not provide complete compositional data) and the increasing position of the 1390 nm absorption. The 2250 nm absorption is known to occur only in the presence of octahedral Al (Post & Noble, 1993), and although it is at times erroneously referred to as the biotite/chlorite "Fe-OH" absorption (Sun et al., 2001; Jones et al., 2005), it is assigned to Al(Mg,Fe)-OH (Besson & Drits, 1997; Martinez-Alonso, 2002; Bishop et al., 2008). The 2330 and 2390 nm absorptions are assigned to Mg-OH (Clark, 1990). Although correlations between composition and absorption positions are known to exist for the fundamental absorptions (>2500 nm), no such correlations have been quantitatively described for most absorptions in the SWIR.

For chlorite, because OH^- groups occur in additional M-sites (in the hydrated octahedral interlayer), its SWIR spectrum shows more absorptions than that of biotite. Main absorptions occur at 1400, 2250 and 2330 nm, and weaker absorptions occur near 1450, 1550, 2000, 2290, 2350 and 2400 nm. McLeod et al. (1987) reported a shift in wavelength of the main absorptions from 1385 to 1410 nm, 2245 to 2265 nm and 2320 to 2365 nm, for high to low (molar) Mg# respectively. King and Clark (1989) also indicated a correlation with Mg#, and provided high resolution spectra of the OH^- overtone region. More recently, Bishop et al. (2008) reported an Al(Mg,Fe)-OH absorption at 2248 nm for clinochlore (Mg# 88) and 2261 nm for chamosite (Mg# 23), which matches the previously reported data. However, no link has been made to variations with Al^{VI} content, which strongly influences the strength and position of absorptions observed in spectra of chlorite.

2.3 Methodology

2.3.1 Sample suite

A total of forty-six crystals or rock samples rich in a mineral of interest were selected for acquisition of infrared (IR) spectra, measured from 1000-2500 nm. Electron microprobe analysis (EMPA) data were acquired on corresponding polished grain mounts (crystal samples) or polished thin sections (rock samples).

For biotite (Bt), fourteen crystals from unknown localities (except Bt-9 and Bt-12 which are from Bancroft, Ontario, Canada) and eleven rock samples were analysed. The crystals ranged in size from 5 mm to 5 cm wide sheets, and were generally <1mm thick. The rock samples were biotite-rich greywackes from the Pontiac Group metasediments, near the town of Malartic, Quebec, Canada. In these samples, biotite occurs in modal abundances of at least 30%, in grains sizes from 50 µm to 2 mm. EMPA compositional data for the twenty-five biotites are reported in Table 2-1.

Table 2-1. Source and composition of biotite (apfu for 11 O) determined from EMPA

Sample	**Type/Source**	**Mg#**	**Si**	**Al^{IV}**	**Al^{VI}**	**Mg**	**Fe**	**Ti**	**Cr**	**Mn**	**Ca**	**Na**	**K**
Bt-8	Crystal (Unk.)	28.4	2.76	1.24	0.26	0.68	1.72	0.15	<0.01	0.03	<0.01	0.01	0.97
Bt-9	Crystal (Bancroft)	60.4	2.98	1.02	<0.01	1.65	1.08	0.13	<0.01	0.03	<0.01	0.05	0.95
Bt-12	Crystal (Bancroft)	59.7	2.98	1.02	<0.01	1.61	1.09	0.13	<0.01	0.06	<0.01	0.08	0.91
Bt-13	Crystal (Unk.)	28.4	2.76	1.24	0.25	0.68	1.72	0.16	<0.01	0.03	<0.01	0.01	0.97
Bt-14	Crystal (Unk.)	82.4	3.01	0.99	0.01	2.35	0.50	0.07	<0.01	0.01	<0.01	0.07	0.92
Bt-15	Crystal (Unk.)	70.5	2.95	1.05	<0.01	1.97	0.82	0.11	<0.01	0.02	<0.01	0.06	0.92
Bt-16	Crystal (Unk.)	58.9	2.98	1.02	<0.01	1.59	1.11	0.13	<0.01	0.06	<0.01	0.08	0.93
Phl-1	Crystal (Unk.)	99.0	2.99	1.01	0.02	2.94	0.03	<0.01	<0.01	<0.01	<0.01	0.19	0.79
Phl-2	Crystal (Unk.)	93.7	3.02	0.98	0.04	2.72	0.18	0.02	<0.01	<0.01	<0.01	0.04	0.95
Phl-3	Crystal (Unk.)	93.7	2.90	1.10	0.11	2.62	0.18	0.04	<0.01	<0.01	<0.01	0.02	0.96
Phl-5	Crystal (Unk.)	92.5	2.91	1.09	0.11	2.59	0.21	0.05	<0.01	<0.01	<0.01	0.02	0.96
Phl-6	Crystal (Unk.)	93.4	3.02	0.98	0.03	2.73	0.19	0.01	<0.01	<0.01	<0.01	0.03	0.95
Phl-7	Crystal (Unk.)	86.9	2.79	1.21	0.17	2.38	0.36	0.06	<0.01	<0.01	<0.01	0.09	0.87
Phl-8	Crystal (Unk.)	94.2	2.89	1.11	0.09	2.68	0.17	0.04	<0.01	<0.01	<0.01	0.04	0.94
P0111	Metased. (Malartic)	72.8	2.88	1.12	0.25	1.82	0.68	0.09	<0.01	0.01	<0.01	0.01	0.94
P0122	Metased. (Malartic)	88.1	2.92	1.08	0.26	2.22	0.30	0.06	0.02	<0.01	<0.01	0.01	0.93
P0906	Metased. (Malartic)	81.6	2.91	1.09	0.24	2.07	0.47	0.07	0.01	0.01	<0.01	0.01	0.96
P0907	Metased. (Malartic)	75.4	2.87	1.13	0.22	1.92	0.63	0.08	0.01	0.01	<0.01	0.01	0.95
K389048	Metased. (Malartic)	62.8	2.80	1.20	0.29	1.56	0.92	0.09	0.01	0.02	<0.01	0.01	0.91
K389056	Metased. (Malartic)	72.7	2.86	1.14	0.27	1.82	0.68	0.09	<0.01	0.01	<0.01	0.01	0.91
K389084	Metased. (Malartic)	54.3	2.77	1.23	0.31	1.35	1.14	0.09	0.01	0.02	0.01	0.02	0.87
K389090	Metased. (Malartic)	56.0	2.77	1.23	0.28	1.38	1.09	0.11	0.01	0.01	<0.01	0.01	0.89
K389202	Metased. (Malartic)	91.7	3.01	0.99	0.15	2.47	0.22	0.04	0.01	0.01	0.01	0.01	0.91
K389203	Metased. (Malartic)	90.6	3.03	0.97	0.09	2.52	0.26	0.04	<0.01	0.01	<0.01	0.01	0.93
K389208	Metased. (Malartic)	57.5	2.81	1.19	0.28	1.42	1.05	0.11	<0.01	0.02	<0.01	0.01	0.93
Representative sample		Total	SiO2	Al2O3		MgO	FeO	TiO2	Cr2O3	MnO	CaO	Na2O	K2O
Bt-16		92.96	38.28	11.03		13.67	17.01	2.22	0.03	0.88	0.01	0.51	9.34

Assumes all Fe as Fe^{2+}. Al^{IV} and Al^{VI} are calculated assuming full occupancy of the T-sites. Mg# is calculated as Mg/(Mg+Fe). Raw data are available in Appendix 1.

Twenty-one chlorite (Chl) samples were analysed. Of those, nine are from the same Pontiac metasediments where biotite samples were acquired, and contained 20-50 modal % chlorite in grain sizes between 50-200 µm. At most traces of biotite were present (always <5% relative to chlorite). A further eight samples were obtained from the University of Alberta mineralogy laboratory, and are of unknown locations. These rock fragments ranged from 0.5 to 4 cm in size, and their protolith could not be identified, as they consisted almost exclusively of chlorite (>95 modal % chlorite, as 0.1-2 mm crystals). Sample Chl-16 was a single thin (<0.5 mm) chlorite crystal 1 x 1 cm in size (i.e., a sheet) of unknown origin and obtained from the McGill University mineralogy laboratory. Of the remaining three samples, one was a light green, so-called *seraphinite* chlorite (from Russia), consisting exclusively of feather-shaped chlorite grains 0.5-5mm in size, one was sample CCa-2 obtained from the Clay Minerals Society Source Clays Repository (>91% modal % chlorite, Vogt et al., 2002), and one was a chamosite (M-10578) from the University of Alberta Museum collection, from Saalfeld, Germany. Compositional data for the chlorites is provided in Table 2-2.

Table 2-2. Source and composition of chlorite (apfu for 14 O) determined from EMPA.

Sample	**Chl %**	**Type/Source**	**Mg#**	**Si**	**Al^{IV}**	**Al^{VI}**	**Mg**	**Fe**	**Ti**	**Mn**	**Ca**	**Na**	**K**
Cca-2	>90	C.M.S (Flagstaff Hill)	97.4	2.84	1.16	1.38	4.38	0.12	<0.01	<0.01	<0.01	<0.01	<0.01
Chl-1	>95	Rock (Unk.)	89.5	3.02	0.98	0.98	4.47	0.53	<0.01	0.01	<0.01	<0.01	<0.01
Chl-2	>95	Rock (Unk.)	18.0	2.60	1.40	1.47	0.80	3.67	0.01	0.01	<0.01	<0.01	<0.01
Chl-5	>95	Rock (Unk.)	74.3	2.68	1.32	1.42	3.35	1.16	<0.01	<0.01	<0.01	<0.01	<0.01
Chl-7	>95	Rock (Unk.)	66.5	2.62	1.38	1.44	2.99	1.50	<0.01	0.02	<0.01	<0.01	<0.01
Chl-9	>95	Rock (Unk.)	65.6	2.62	1.38	1.46	2.93	1.54	<0.01	0.02	<0.01	<0.01	<0.01
Chl-10	>95	Rock (Unk.)	60.7	2.63	1.37	1.58	2.54	1.65	<0.01	0.12	<0.01	<0.01	<0.01
Chl-11	>95	Rock (Unk.)	92.2	2.90	1.10	1.09	4.52	0.38	0.01	<0.01	<0.01	<0.01	<0.01
Chl-16	100	Crystal (Unk.)	95.3	3.29	0.71	0.63	5.14	0.25	<0.01	<0.01	<0.01	<0.01	<0.01
Seraphinite	100	Unknown (Russia)	95.6	3.32	0.68	0.80	4.91	0.23	<0.01	<0.01	<0.01	<0.01	<0.01
Basalt_L	≈ 30	Metabasalt (Val d'Or)	47.6	2.73	1.27	1.21	2.27	2.50	<0.01	0.04	0.01	0.01	<0.01
M10573	≈ 50	Saalfeld (Germany)	10.9	2.51	1.49	1.52	0.47	3.84	0.07	<0.01	<0.01	<0.01	<0.01
M-1391-1790	≈ 30	Metased. (Malartic)	75.0	2.89	1.11	1.11	3.63	1.21	<0.01	0.01	0.03	<0.01	0.01
M-1391-1950	≈ 30	Metased. (Malartic)	76.8	3.00	1.00	1.07	3.75	1.13	<0.01	0.01	0.01	<0.01	0.01
M-1771-0269	≈ 30	Metased. (Malartic)	66.7	2.90	1.10	1.04	3.27	1.63	<0.01	0.02	0.06	<0.01	<0.01
M-1771-0270	≈ 30	Metased. (Malartic)	66.7	2.90	1.10	1.05	3.28	1.64	<0.01	0.02	0.03	<0.01	<0.01
M-1771-0948	≈ 30	Metased. (Malartic)	55.8	2.88	1.12	1.14	2.64	2.09	0.01	0.02	<0.01	0.01	0.06
M-1771-1115	≈ 30	Metased. (Malartic)	55.5	2.93	1.07	1.13	2.66	2.13	0.01	0.02	<0.01	<0.01	0.03
Pn1450	≈ 30	Metased. (Malartic)	41.7	2.68	1.32	1.36	1.89	2.65	0.01	0.03	0.03	<0.01	0.01
Pn1975	≈ 30	Metased. (Malartic)	43.8	2.71	1.29	1.36	1.99	2.56	0.01	0.03	0.02	<0.01	<0.01
Pn1990	≈ 30	Metased. (Malartic)	70.7	2.79	1.21	1.31	3.25	1.35	0.01	0.02	<0.01	<0.01	0.02
Representative sample			Total	SiO2	Al2O3		MgO	FeO	TiO2	MnO	CaO	Na2O	K2O
Chl-7			84.84	25.15	22.93		19.22	17.25	0.06	0.22	0.01	0.00	0.00

Assumes all Fe as Fe^{2+}. Mg# is calculated as Mg/(Mg+Fe). Al^{IV} and Al^{VI} are calculated assuming full occupancy of the T-sites. Raw data are available in Appendix 1.

2.3.2 Collection of EMPA data

Electron microprobe data were acquired on a JEOL 8900R instrument equipped with five wavelength dispersive spectrometers (WDS). Instrument conditions were a 20 nA beam current, a 15 kV acceleration voltage, and a 5 µm probe diameter. Data were acquired at a 30 second counting time on both peak and background, and were reduced using a CITZAF correction procedure (Armstrong, 1995). Detection limits are <0.02 wt% for all elements and relative analytical error is <1% for major elements. For the crystals (mica sheets), grain mounts were prepared using thin sheets (≈10 x 5 x <0.2 mm) cut from the larger crystal sheets. For the rock samples, sub-samples used for EMPA included thin section sized pieces, down to 5 x 5 mm fragments. In each case, the mean of 10 to 30 individual EMPA data points acquired over the entirety of the sample is reported.

2.3.3 Collection of infrared reflectance spectra

Infrared reflectance spectra between ≈1000-2500 nm were acquired using a Specim SisuROCK™ hyperspectral scanner. The instrument contains a 256 spectral x 320 spatial pixels mercury-cadmium-telluride (MCT) array, yielding data at a 6.3 nm sampling rate and 10 nm spectral bandwidth. Here, data was acquired at close range using an OLES56 lens, giving a spatial resolution of 0.2 x 0.2 mm/pixel. For each acquisition, dark current and a 99% reflectance Spectralon™ white panel (made of polytetrafluoroethylene) were measured. First, dark current data were subtracted from all data, which were then normalized to (divided by) the spectrum of the white panel. All data were further normalized to the spectrum of an Infragold® panel. Each scan included a wavelength calibration standard to correct for any drift in wavelength position between scans, and a correction factor of at most 0.5 nm was added or subtracted to the data.

Broken surfaces on rock fragments produced quality reflectance spectra, and sample preparation (cutting to obtain a flat surface) did not significantly affect reflectance spectra; no sample preparation was therefore required for rock samples. For the large mica crystals (here placed over a dark background), specular reflectance was problematic. All samples were therefore lightly scratched with a tungsten point to produce a thin layer of fine-grained material, which mitigated this issue, and produced quality spectral data.

Given the high spatial resolution of the data (0.2 x 0.2 mm/pixel), representative infrared spectra were obtained by averaging spectra over larger areas. For rock samples (or thin section offcuts), the average was computed for an area up to 50 x 50 pixels (1 x 1 cm) in size. For smaller samples, and for many crystals, areas as small as 9 x 9 pixels were selected from the scratched portion of the sample.

2.3.4 Analysis of reflectance spectra

An objective of this study is to determine the displacement of absorption features as a function of mineral chemistry, which can vary by 20-30 nm. Given the ≈6 nm sampling interval of the instrument, the acquired spectra need to be interpolated in order to yield precise absorption feature positions. To achieve this, the original spectrum was first linearly interpolated to 0.1 nm (an arbitrarily high sampling rate), and smoothed by convolution with a Gaussian function (Clark et al., 1993; van den Boomgaard & van der Weij, 2001). Because the FWHM of the Gaussian function ($2\sqrt{2ln2}\,\sigma$) is set at 10 nm, which is larger than the original sampling of the data, the resulting convolved spectrum is a smoothed version of the raw spectrum.

After interpolation and smoothing, absorption positions are retrieved from reflectance minima on continuum removed spectrum (here calculated using straight line segments, Clark and Roush, 1984). In cases where absorptions are weak, or when multiple absorptions are superimposed, derivative analysis is performed to identify local maxima on the second derivative of the convolved spectrum. For asymmetric absorptions these two methods (continuum removal or derivative analysis) of estimating absorption position yield slightly different results, with the derivative data being offset towards the side with the strongest slope. Therefore, two datasets and two regression lines are reported for each absorption, if possible.

2.3.5 Wavelength calibration of reflectance spectra

Spectral data for a clear Mylar standard (placed on a white panel) referenced to that of the National Institute of Standards and Technology (NIST) was acquired to ensure spectral precision of the instrument, and to illustrate the benefits of the spectral interpolation methodology (Fig. 2-1, top). The estimated absorption positions for this spectrum are within 0.3 nm of the reference values, and are therefore considered precise. Mylar is a stretched form of polyethylene terephtalate (PET), a commonly available plastic which bears the resin identification code (recycling symbol) #1. A PET film was also measured, and showed a slightly different spectrum (Fig. 2-1, bottom) than the Mylar sheet, but all tested PET samples showed absorption positions consistently within ±0.5 nm amongst themselves. Commonly available PET can therefore serve as an alternative spectral calibration standard.

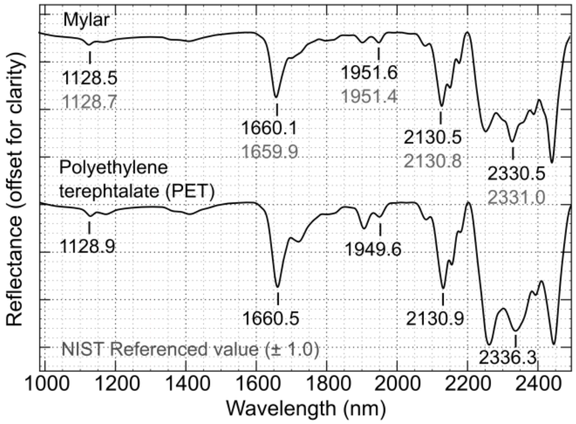

Figure 2-1 *Continuum removed spectra of calibration standards. Top: Mylar standard with measured absorption positions in black (as minima on continuum removed spectra), and NIST referenced values in grey. Bottom: Spectrum of clear PET.*

2.4 Results

2.4.1 Compositional variability of the sample suite

Compositional data for all samples as determined from EMPA were listed in Tables 2-1 and 2-2. The biotite series varies by simple Mg-Fe substitution from phlogopite (Mg# 100) to annite (Mg# 0) end-members at 0.0 Al^{VI}, and by Tschermak substitution to siderophyllite and eastonite end-members at Al^{VI}1.0 (from annite and phlogopite, respectively). Analyzed biotites vary from Mg# 99 to 28, and from Al^{VI} 0.0 to 0.31. Chlorite is defined as clinochlore if Mg-rich and chamosite if Fe-rich, ideally with 1.0 Al^{VI}, although Al content can vary significantly. Here, samples range from Mg# 97-11, with Al^{VI} contents between 0.6 and 1.6.

2.4.2 Spectral results

Biotite – Overview of correlation with sample composition

Biotite has major absorptions around 1390, 2250, 2330, 2390 nm, and a weak absorption around 2120 nm (Fig. 2-2). Because biotite accommodates variation in both Mg# and Al^{VI} contents, the effects of each of these substitutions were analyzed independently. Table 2-3 reports all spectrally derived biotite data. All absorption positions are retrieved from both the continuum removed spectra and from the second derivative of the spectra, except for the 2330 nm absorption which cannot be reliably obtained from derivative data because of its larger width. Continuum removed strength of the 2250 and 2330 nm absorptions are also reported (i.e., 1 – value of the continuum removed minimum reflectance).

Table 2-3. *Position and strength of absorptions observed in biotite.*

Sample	Type	Mg#	Al^{VI}	1390 nm	D"	2250 nm	D"	2330 nm	2390 nm	D"	Str. 2250	Str. 2330	R. 2250/2330
Bt-8	Crystal	28.4	0.26	-	-	2255.8	2256.0	2348.4	-	2404.7	0.024	0.058	0.412
Bt-9	Crystal	60.4	0.00	-	1389.1	-	-	2334.8	2391.4	2390.9	0.000	0.098	0.000
Bt-12	Crystal	59.7	0.00	-	1388.0	-	-	2333.7	2391.3	2390.2	0.000	0.053	0.003
Bt-13	Crystal	28.4	0.25	-	-	2255.6	2254.7	2350.5	-	2401.4	0.018	0.037	0.485
Bt-14	Crystal	82.4	0.01	1380.7	1380.7	-	-	2324.1	2381.1	2382.6	0.030	0.175	0.172
Bt-15	Crystal	70.5	0.00	-	1381.9	-	-	2327.8	2386.7	2386.1	0.000	0.088	0.000
Bt-16	Crystal	58.9	0.00	-	1385.0	-	-	2335.4	2390.4	2392.7	0.000	0.273	0.000
Phl-1	Crystal	99.0	0.02	1378.2	1377.6	2248.1	2245.2	2319.0	2377.3	2379.8	0.051	0.247	0.207
Phl-2	Crystal	93.7	0.04	1375.8	1380.2	2248.2	2245.8	2321.0	2379.7	2381.2	0.028	0.244	0.116
Phl-3	Crystal	93.7	0.11	1378.2	1377.8	2247.0	2245.8	2323.3	2379.9	2380.9	0.060	0.170	0.354
Phl-5	Crystal	92.5	0.11	1378.4	1377.6	2246.7	2245.3	2323.1	2379.4	2380.6	0.077	0.194	0.396
Phl-6	Crystal	93.4	0.03	1378.2	1378.8	2248.7	2246.1	2320.8	2379.0	2381.1	0.049	0.259	0.189
Phl-7	Crystal	86.9	0.17	-	1379.6	2248.7	2246.5	2325.0	2380.8	2382.3	0.096	0.268	0.357
Phl-8	Crystal	94.2	0.09	1378.6	1377.6	2247.5	2245.5	2323.1	2379.4	2380.7	0.162	0.445	0.363
P0111	Metased.	72.8	0.25	1382.2	1383.9	2249.7	2248.1	2330.4	2383.3	2384.9	0.073	0.156	0.467
P0122	Metased.	88.1	0.26	1381.2	1377.6	2246.4	2243.5	2323.3	2378.1	2381.8	0.159	0.272	0.586
P0906	Metased.	81.6	0.24	1382.1	1379.6	2247.5	2245.4	2326.1	2380.7	2382.4	0.106	0.220	0.481
P0907	Metased.	75.4	0.22	1383.6	1381.3	2248.7	2246.5	2328.4	2381.1	2383.4	0.163	0.295	0.552
K389048	Metased.	62.8	0.29	1391.5	1384.2	2250.6	2249.0	2333.2	2383.6	2388.4	0.090	0.150	0.598
K389056	Metased.	72.7	0.27	1385.0	1386.5	2248.0	2246.9	2330.6	2379.2	2384.5	0.043	0.096	0.444
K389084	Metased.	54.3	0.31	1389.8	1388.7	2251.9	2250.1	2336.4	2388.1	2391.1	0.055	0.078	0.708
K389090	Metased.	56.0	0.28	1387.9	1387.7	2251.6	2249.5	2335.7	2386.5	2389.6	0.077	0.120	0.639
K389202	Metased.	91.7	0.15	1377.1	1377.1	-	-	2319.9	2374.6	2379.6	-	-	-
K389203	Metased.	90.6	0.09	1377.3	1376.8	-	-	2321.7	2378.4	2379.5	-	-	-
K389208	Metased.	57.5	0.28	-	1386.2	2250.7	2249.7	2335.9	2385.5	2388.6	0.054	0.109	0.494

Absorption positions of biotite, obtained as the minimum on the continuum removed reflectance spectrum, or from the maximum of the second derivative of the spectrum (indicated as D"). Where absorptions are not reported, no absorption was detectable. Cells highlighted in grey are low Al^{VI} *samples, and are not included in the regression. Also reported are the strengths of the 2250 and 2230 nm absorptions and their ratio.*

Typical spectra of biotite with variable Mg# (but similar Al^{VI} content) are shown on Figure 2-2a. Sample Bt-13 is a biotite crystal with Mg# 28 (0.25 Al^{VI}), whereas sample P906 is a biotite-rich greywacke with Mg# 82 (0.24 Al^{VI}). A weak but significant positive correlation exists between Mg# and absorption strength for all absorptions (e.g., at 2330 nm R^2=0.5, N=21), where absorptions decrease in strength with decreasing Mg#. This is readily apparent in Figure 2-2a, where all absorptions in the top spectrum (Mg# 28) are weaker than those in the bottom spectrum (Mg# 82). Figure 2-2b shows spectra of biotite with variable Al^{VI} content but similar Mg#. Sample Bt-9 is a biotite crystal (Mg# 60) that is free of Al in its octahedral site (Al^{VI} = 0.00), whereas sample K389048 is a biotite-rich greywacke (Mg# 63) with an octahedral

Al content of 0.29. The Al^{VI}-free biotite has no absorption around 2250 nm, but the 2330 and 2390nm absorptions are present for all biotite compositions.

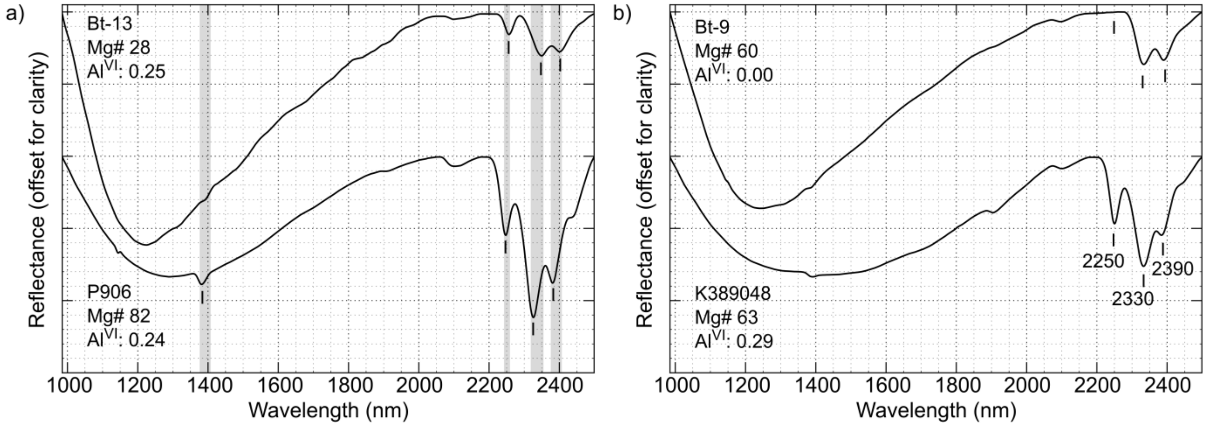

Figure 2-2 *Continuum removed spectra of selected biotites: a) spectra of* Al^{VI}*-bearing biotite with variable Mg#. The possible range of absorption feature is indicated by the grey bars. b) Biotite with variable* Al^{VI} *content, but similar Mg#. Indicated absorptions are the general absorption positions, refer to Table 2-3 for exact data.*

Biotite – Correlation of specific absorptions with sample composition

Correlations between Mg# and absorption positions are reported in Figures 2-3a-d, and correlation of Al^{VI} with absorption strengths is reported in Figure 2-3e, with detail of biotite spectra with variable Al^{VI} content shown in Figure 2-3f. In all cases, absorptions shift to longer wavelengths with decreasing Mg#, from around 1375 to 1410 nm, 2245 to 2261 nm, 2319 to 2360 nm, and 2377 to 2411 nm for the range Mg# 100 to Mg# 0. The 1390 nm absorption is generally weak in biotite, consequently its position could not be retrieved in several samples (primarily in the crystal samples). The 2250 nm absorption is only present if $Al^{VI} > 0$, as reported in Post & Noble (1993). As with other absorptions, its position can be used to estimate Mg#, but there is a systematic bias towards longer wavelengths with decreasing Al^{VI} content as seen on

Figure 2-3b. Because of this, only samples with Al^{VI} >0.2 (black data points) are used to produce the regression line. For those samples, there is a good correlation with Mg# (R^2 of 0.98), with a standard error better than ±3.1 Mg# (corresponding to a change of 0.5 nm). The 2330 nm absorption, present in all samples, can also be used to estimate Mg# to ±3.2 Mg# (Fig. 2-3c). However, because of its large width, its position cannot be reliably estimated by derivative analysis. The 2390 nm absorption (Fig. 2-3d), on the other hand, yields better results when its position is retrieved from the second derivative of the spectrum, likely because this absorption is close to the end of the measured spectral range (2500 nm), which would affect the continuum removal procedure. Here, the continuum removed regression has an R^2 of 0.76, in contrast to 0.94 for the derivative data.

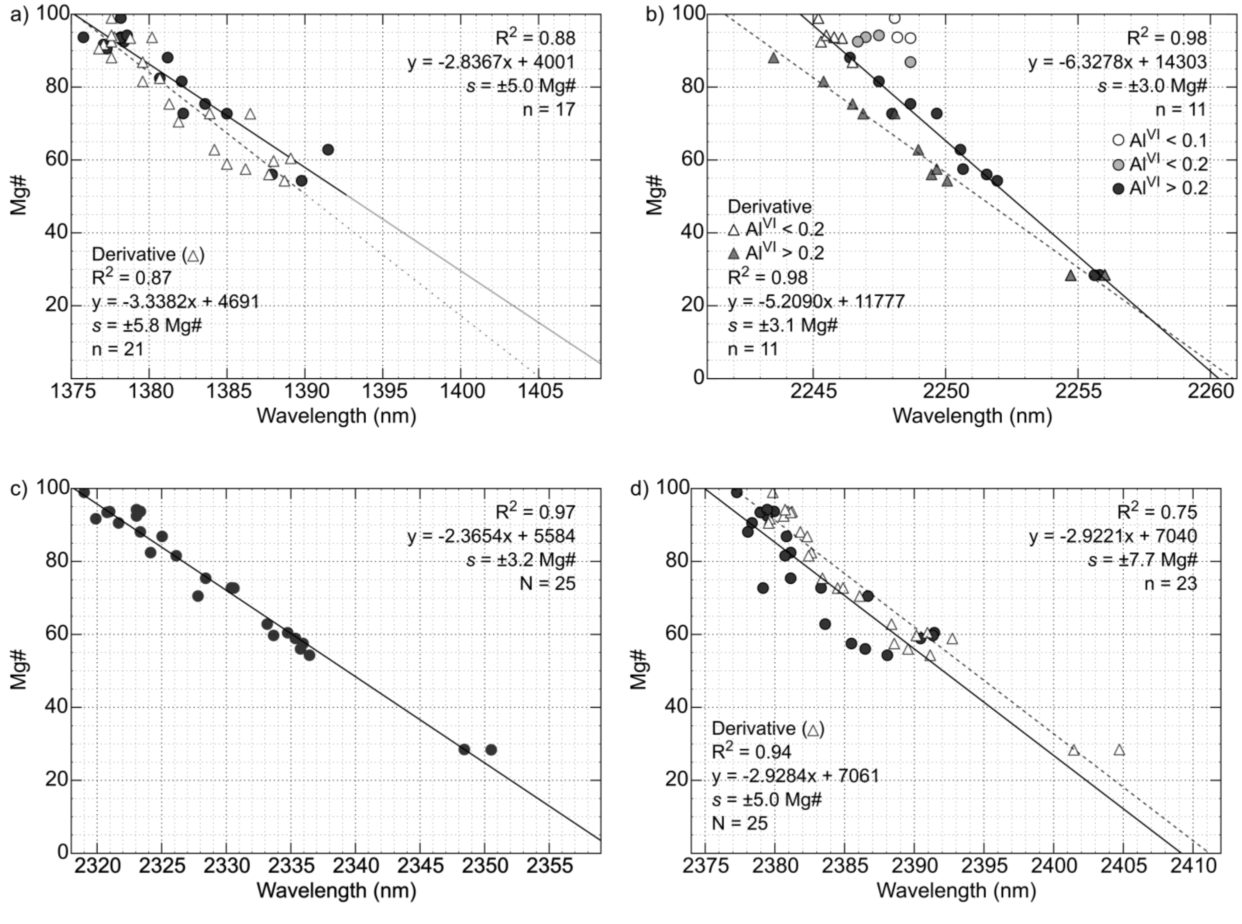

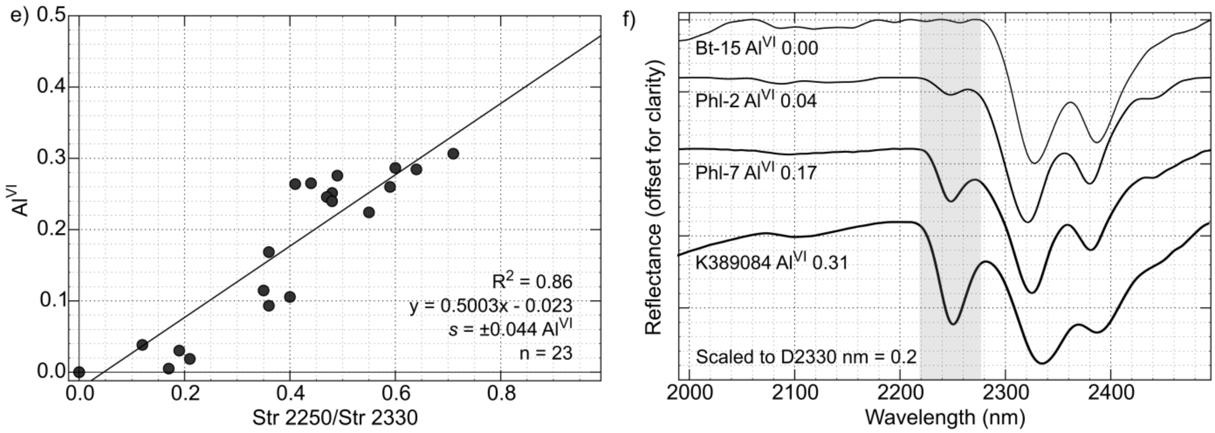

Figure 2-3 *Correlations between biotite composition and spectral data. Absorption position is retrieved as the position of the minima on the continuum removed spectra (circles and full line) or as a maximum of the second derivative spectra (triangles and dashed line). Exact data are listed in Table 3. Correlation for Mg# and the position of the a) 1390 nm absorption, b) 2250 nm absorption, c) 2330 nm absorption, d) 2390 nm absorption. e) Correlation between the* Al^{VI} *content and the ratio of the 2250 and 2330 nm absorption strengths. f) Continuum removed spectra for biotite with variable* Al^{VI} *content.*

The 2250 nm absorption is only present if there is octahedral Al in biotite ($Al^{VI}>0$), and its strength progressively increases with increasing Al^{VI} (Fig. 2-3f). The ratio of the 2250 nm over the 2330 nm absorption strengths can therefore be used to estimate the Al^{VI} content of biotite (independently of Mg#) with a standard error of 0.044 Al^{VI}, as shown in Figure 2-3e.

Chlorite – Overview of correlation with sample composition

Chlorite contains a T-O-T structure similar to that of biotite, and therefore shows major absorptions at similar positions, around 1400, 2250 and 2330 nm. Additional weaker absorptions are also apparent near 1450, 1550, 2000, 2100, 2290, 2350 and 2400 nm, some of which likely stem from the additional hydrated interlayer present in chlorite, and some of which are only apparent given specific chlorite compositions. All data for chlorite absorption positions are reported in Table 2-4.

Table 2-4*. Position of absorptions observed in chlorite.*

Sample	Mg#	Al^{VI}	1400 nm	D"	1450 nm	2000 nm	2100 nm	2250 nm	D"	2290 D"	2330 nm	2400 D"	R. 2330/2250
Cca-2	97.4	1.38	1396.9	1390.4	1439.3	1981.4	2108.2	2248.0	2248.5	2289.6	2324.3	2393.7	1.024
Chl-1	89.5	0.98	1391.2	1389.7	1436.2	1988.8	2110.2	2247.8	2248.3	2290.2	2317.5	2391.8	0.910
Chl-2	18.0	1.47	1411.7	1412.5	-	2009.4	-	2261.5	2262.0	2316.5	2357.8	-	0.987
Chl-5	74.3	1.42	1402.4	1397.9	1445.1	1991.8	2117.0	2252.3	2252.9	2296.1	2336.3	2403.0	0.988
Chl-7	66.5	1.44	1406.7	1407.2	1450.5	1998.2	2122.4	2254.5	2255.1	2303.6	2342.0	-	1.010
Chl-9	65.6	1.46	1406.7	1407.3	1448.8	1997.0	2119.7	2254.1	2254.7	2301.0	2341.2	-	1.017
Chl-10	60.7	1.58	1408.0	1407.9	1444.3	1998.6	2122.0	2255.4	2255.9	2306.8	2344.4	-	1.017
Chl-11	92.2	1.09	1391.0	1389.5	1438.1	1989.1	2105.1	2248.3	2248.8	2292.3	2325.3	2391.1	0.912
Chl-16	95.3	0.63	1391.3	1389.0	-	1981.0	2107.1	2239.3	2239.3	2291.3	2318.6	2392.1	0.858
Seraphinite	95.6	0.80	1392.9	1388.1	-	1979.3	2107.0	2240.5	2241.0	2292.5	2320.9	2392.2	0.862
Basalt_L	47.6	1.21	1405.2	1403.6	1458.1	-	-	2258.3	2258.3	2313.8	2341.0	-	0.960
M10573	10.9	1.52	1413.0	1413.0	-	-	-	2262.4	2262.7	2318.5	2361.6	-	0.993
M-1391-1790	75.0	1.11	1397.6	1393.5	1447.7	1994.9	2116.0	2252.1	2252.1	2295.9	2335.3	2394.5	0.941
M-1391-1950	76.8	1.07	1396.5	1392.9	1439.7	1992.0	2117.0	2251.7	2251.6	2295.4	2333.4	2396.0	0.943
M-1771-0269	66.7	1.04	1400.1	1395.8	1450.3	1997.3	2117.4	2253.2	2253.2	2300.1	2337.8	2397.5	0.916
M-1771-0270	66.7	1.05	1400.9	1395.3	1451.6	1997.1	2117.9	2254.6	2254.6	2296.4	2333.1	2398.7	0.958
M-1771-0948	55.8	1.14	1404.9	1402.4	1455.4	1998.7	2120.1	2255.9	2255.9	2306.4	2342.9	-	0.973
M-1771-1115	55.5	1.13	1402.3	1399.5	1451.5	1999.8	2119.5	2254.0	2254.0	2306.5	2340.7	-	0.930
Pn1450	41.7	1.36	1407.5	1407.6	1464.1	-	-	2258.0	2258.0	2314.7	2347.9	2409.8	0.988
Pn1975	43.8	1.36	1406.5	1406.5	1453.6	2002.1	2123.2	2257.8	2257.8	2311.0	2345.9	-	0.988
Pn1990	70.7	1.31	1401.5	1397.8	1449.5	1996.2	2117.6	2252.6	2252.6	2305.4	2336.6	2396.4	1.001

Absorption positions for chlorite, obtained as the minimum on the continuum removed reflectance spectrum, or from the maximum of the second derivative of the spectrum (indicated as D"). Cells highlighted in grey are outliers not included in the regressions. Additionally, the ratio of the continuum removed depths of the 2250 and 2330 nm absorptions is included.

As in biotite, chlorite can vary in Mg# and in Al^{VI} content, and the effects on the spectrum of each of these elements were analyzed independently. Figure 2-4a shows typical spectra of chlorite with variable Mg# (but similar Al^{VI} content), with a detailed view of part of the combination band region (2150-2450 nm) shown on Figure 2-4b. Sample Chl-5 has an Mg# of 74 (1.42 Al^{VI}), whereas Chl-2 has an Mg# 18 (1.45 Al^{VI}). With a decrease in Mg#, the position of all absorptions shifts to longer wavelengths, and the strength of all absorptions decreases (Fig. 2-4a). The weak 2300 nm absorption decreases in strength more rapidly than the 2330 nm absorption, changing the overall appearance of the spectrum in this region (Fig. 2-4b).

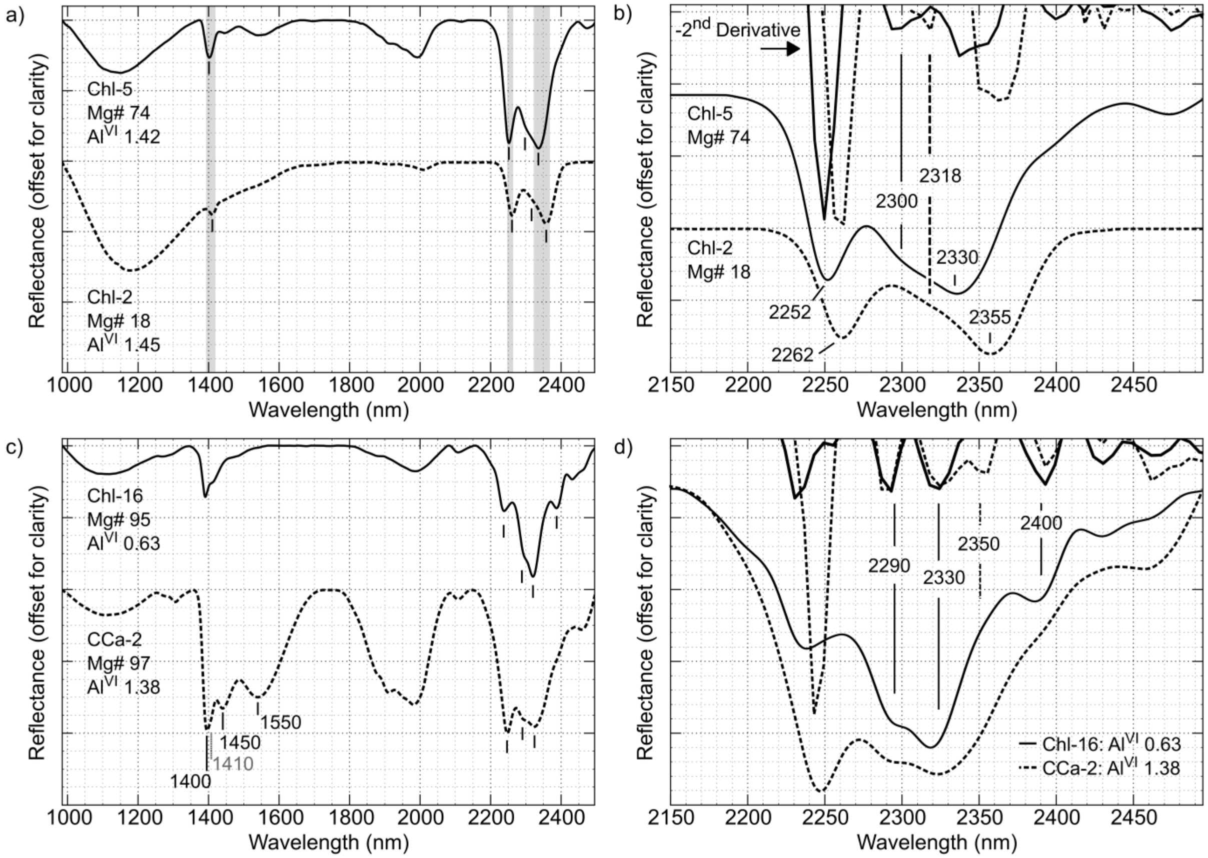

Figure 2-4 *Continuum removed reflectance spectra of chlorites with variable compositions. a) Chlorites with highly variable Mg# but similar Al^{VI} contents. The possible range of absorption positions is indicated by the grey bars. b) Detail of the combination bands region (2150-2500 nm) of the spectra shown in a). The second derivative of the spectra is shown on top, and was computed from the original spectra, with no interpolation. c) Spectra of chlorites with variable Al^{VI} contents but similar Mg#. d) Detail of the spectra shown in c).*

Figure 2-4c shows spectra of chlorite with variable Al^{VI} content but similar Mg#. Sample Chl-16 (top spectrum) is a chlorite crystal with an Al^{VI} content of 0.63 (Mg# 95), and Cca-2 (bottom spectrum) is a chlorite-rich rock with an Al^{VI} content of 1.38 (Mg# 97). A detailed view of the 2150-2450 nm region is shown on Figure 2-4d. The two broad absorptions at 1450 and 1550 nm are prominent only in high-Al^{VI}, high-Mg# samples (Cca-2, Chl-5), and are weak or undetectable in either low-Al^{VI} (Chl-16) or low Mg# (Chl-2) samples. In low-Al^{VI} samples, only weak shoulders occur around 1430 and 1480 nm. As in biotite, the depth of the 2250 nm absorption in chlorite is positively correlated to Al^{VI} content. The absorption near 2330 nm is narrow for the Al^{VI}-poor chlorites (Chl-16), but becomes much broader in the Al^{VI}-rich (Cca-2) samples. This broadening is due to the appearance of an additional, highly overlapping absorption near 2350 nm for Al^{VI}-rich chlorite (>1.0 Al^{VI}), visible in second derivative spectra (Figure 2-4d, top). However, this second absorption cannot be isolated in most other samples due to the limited spectral resolution of the instrument used in this study. Finally, the appearance of the 2350 nm absorption partially masks the weak 2400 nm absorption present in Mg-rich chlorites, which remains nonetheless resolvable in second derivative data of several samples.

Chlorite – Correlation of specific absorptions with sample composition

Correlations between Mg# of chlorite and absorption positions are reported in Figure 2-5. The main 1400 nm absorption of chlorite varies from approximately 1386 to 1419 nm for the range Mg# 100-0 (Fig. 2-5a), a position roughly 10 nm above the corresponding absorption of biotite, for an equivalent Mg#.

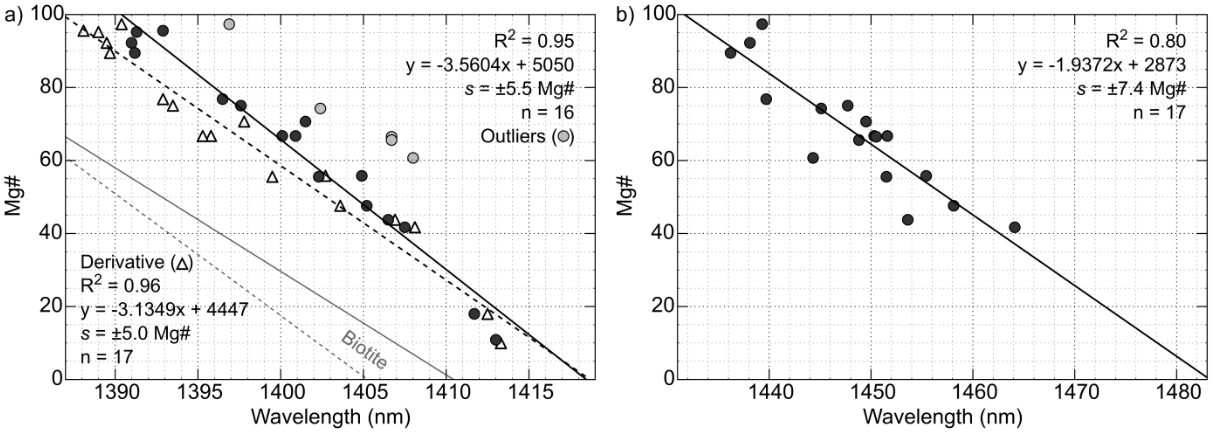

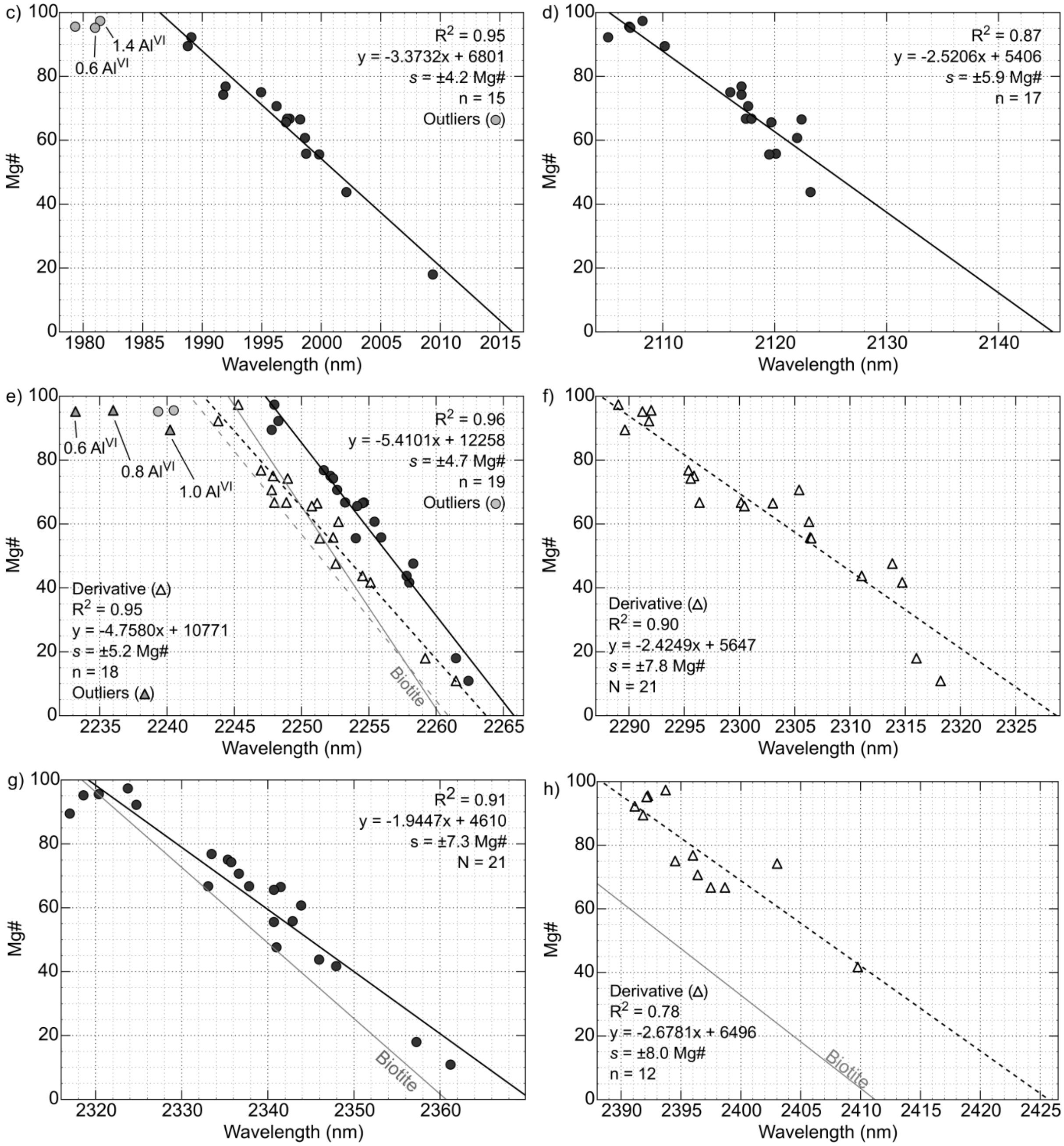

Figure 2-5 *Correlations between Mg# of chlorite and position of a given absorption feature, obtained as a minimum on the continuum removed reflectance spectra (circles and solid regression line), or from the second derivative of the spectrum (triangles and dashed regression line). a) 1400 nm, showing several outliers due to the influence of a second absorption (1410 nm). b) 1450 nm, a weak absorption not detectable in all samples. c) 2000 nm, a weak absorption in many cases, but strong in the three outliers (grey circles Cca-2, Seraphinite, Chl-16). d) 2100 nm, a weak absorption not detectable in all samples. e) 2250 nm. Samples with*

Al^{VI} ≤ 1.0 (grey data points) do not follow the regression. f) 2290 nm. g) 2330 nm. h) 2400 nm. In all cases, light grey lines are regressions derived for biotite.

The 1450 nm absorption is broad (Fig. 2-4) and difficult to detect in many samples. Because of its larger width, its position is only retrieved as a minimum on continuum removed spectra, with convex hull endpoints fixed at 1350 and 1650 nm, and varies from an estimated 1430-1480 nm for Mg# 100-0 (Fig. 2-5b). Because this absorption is also influenced by Al^{VI} content (Fig. 2-4c), the correlation with Mg# is weaker ($R^2 = 0.80$) than that of most other absorptions (Figure 2-5). The broader 1550 nm absorption could not be precisely located in most samples and is therefore not reported.

The 2000 nm absorption varies from approximately 1980 to 2010 nm (Fig. 2-5c) and produces a strong correlation ($R^2 = 0.95$) with Mg#. Three of the purest chlorite samples (modal abundances >90%; Cca-2, Seraphinite, and crystal Chl-16) have this absorption around 1980 nm, 10 nm lower than expected based on the correlations observed for the remainder of the samples. This departure remains unexplained but is not due to Al^{VI} content, as these three outliers include both low and high-Al^{VI} chlorites. A weak absorption occurs between 2105 to an extrapolated 2145 nm (Fig. 2-5d) for all samples, but its position is more difficult to precisely locate ($R^2 = 0.87$).

The major absorption at 2250 nm varies from 2248 to 2266 nm (or 2243-2264 nm for derivative data) for the range of Mg# 100-0, but is valid only when the Al^{VI} content is above 1.0 apfu (black dots, white triangles, Fig. 2-5e). For these data, the regression enables the estimation of the Mg# of chlorite to better than ±5.2 Mg#. A systematic departure to lower wavelengths is observed for samples with Al^{VI} content below 1.0, as seen for the three samples Chl-1 (0.98

Al^{VI}), Seraphinite ($0.80Al^{VI}$), and Chl-16 (0.63 Al^{VI}). For equivalent Mg#, this absorption in chlorite is located 3 to 6 nm above that of biotite.

A weak absorption occurs around 2290 nm for all compositions, but can only be detected in derivative spectra (Fig. 2-5f), as it highly overlaps with the strong 2330 nm absorption. Its position varies from 2288 nm at Mg# 100 to an estimated 2329 nm at Mg# 0, and its strength relative to the main 2330 nm absorption decreases with decreasing Mg# (Fig. 2-4b). At least two overlapping absorptions are observed near 2330 and 2350 nm for Al^{VI}-rich chlorites (Fig. 2-4d), and cannot be confidently deconvolved because of the limited resolution of the instrument. As a consequence, a single absorption position is reported (referred to as the 2330 nm absorption, Figure 2-5g), and includes the influence from both the 2330 and 2350 nm absorptions (Fig. 2-4d). Finally, a weak absorption occurs around 2400 nm (Figure 2-5h) and for an equivalent Mg#, is located roughly 15 nm above the corresponding absorption in biotite. However, in Al^{VI}-rich chlorites, its presence is masked by the 2350 nm absorption.

As for biotite, the Al^{VI} content of chlorite can be estimated from the ratio of the depths of the 2250 and 2330 nm absorptions (Fig. 2-6a). Figure 2-6b illustrates the effect of variable Al^{VI} content on chlorite spectra, highlighting the changes in depths between the 2250 and 2330 nm absorptions, and the apparent broadening of the 2330-2350 nm absorption.

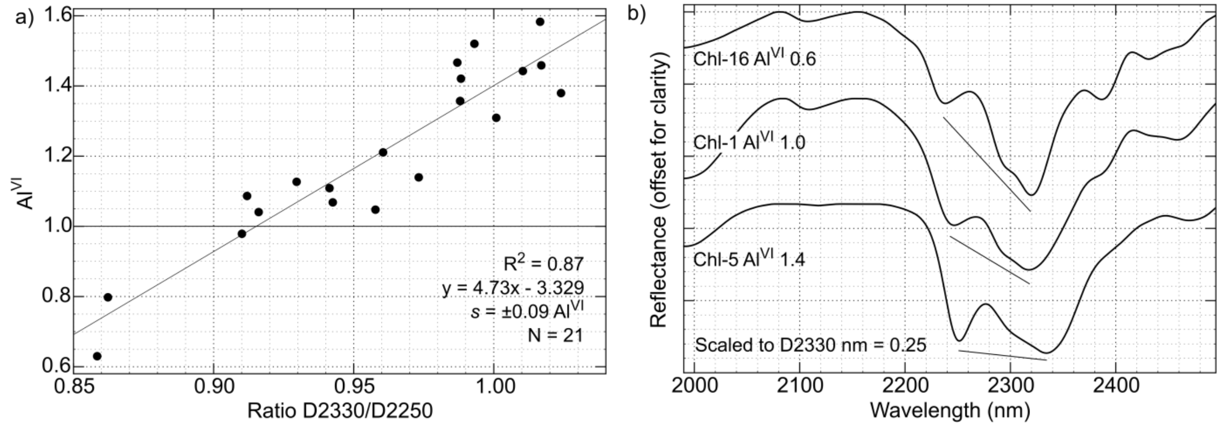

Figure 2-6 *Variability of the spectral response of chlorite with Al^{VI} content. a) Correlation between Al^{VI} content and ratio of the depths of the 2330 over the 2250 nm absorptions. b) Detail of continuum removed spectra for the 2000-2500 nm region for chlorites with increasing Al^{VI} content. Solid lines under the spectra provide a visual cue to the change in absorption strengths.*

2.5 Discussion

Several correlations between spectral features and the mineral chemistry of biotite and chlorite have been presented. However, some of these spectral metrics can be prone to interference from other minerals (e.g., in mineral mixtures in drill core, outcrop, or airborne imagery), and some are valid only within a given range of mineral compositions. It is critical to recognize when these problematics might occur, as they can generate erroneous compositional estimations.

2.5.1 Identification of mineral mixtures

Biotite and chlorite often occur as intimate mineral mixtures, and because they have absorptions at common positions, they are prone to spectral interference. As corresponding absorptions between the two minerals can differ by 1-15 nm for an equivalent Mg#, incorrectly identifying the mineral can lead to errors in the estimation of composition of ≈10 Mg# (Fig. 2-

6e), and possibly up to 40 Mg# (Fig. 2-6a) depending on the absorptions used for the estimation. As any number of other minerals can produce interference (amphibole, epidote, talc), here, only the general case of mixtures of biotite and chlorite with at least intermediate Al^{VI} contents is considered, which should be applicable to most geological environments (other than in Al-poor ultramafic rocks).

Chlorite, because it contains an additional hydrated interlayer (brucite-like or gibbsite-like sheet), shows more absorption features than biotite. In biotite-chlorite mixtures (Fig. 2-7), its presence can therefore be detected from the occurrence of any of its unique absorptions at 1450, 1550, 2000 or 2290 nm. However, most of these secondary absorptions are weak, and generally only the 2000 nm absorption is detectable (Fig. 2-7, middle and bottom spectra). Although an absorption also occurs around 2400 nm for Al^{VI}-poor chlorites, it is much weaker than the equivalent 2390 nm absorption of biotite; the latter can therefore be used to identify biotite in mixtures (Fig. 2-7, top and middle spectra).

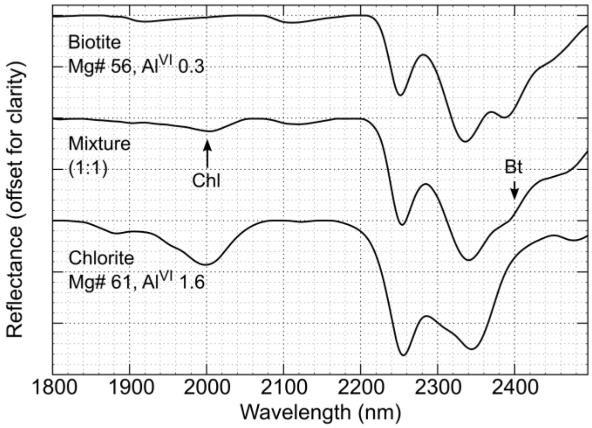

Figure 2-7 *Comparison between continuum removed spectra of biotite, chlorite, and of a greywacke sample containing an approximately 1:1 mixture of both minerals, as determined by optical microscopy.*

In mixtures, the strong absorptions common to both minerals (1400, 2250, 2330 nm) display a position between that of pure biotite and chlorite for a given Mg#. Based on the regression presented in Figure 2-5, this results in an underestimation of Mg# for biotite and an overestimation for chlorite. In such cases, the Mg# of chlorite could be estimated from the 2000 nm absorption, and that of biotite from the 2390 nm absorption, although errors are likely to be larger than those reported for pure samples in Figures 2-3 and 2-5.

2.5.2 Systematic offsets of the 2250 nm Al(Mg,Fe)-OH absorption and potential pitfall in its use

The 2250 nm absorption is a spectral feature broadly used by the remote sensing community for the estimation of Mg# for both biotite and chlorite. However, as this absorption is related to Al(Mg,Fe)-OH, it only provides a valid estimate of Mg# for Al^{VI}-rich samples. To insure it is used appropriately, the Al^{VI} content of either mineral can be determined based on the relative strengths of the 2250 and 2330 nm absorptions, as shown from the regressions in Figures 2-3e and 2-6a, for biotite and chlorite, respectively.

In biotites with $Al^{VI}<0.2$, the 2250 nm absorption is shifted to longer wavelengths, leading to an underestimation of Mg# (Figure 2-3b). In such cases, the Mg# can be accurately estimated from any of the other absorptions (1390, 2330 or 2390 nm), which are related to (Mg,Fe)-OH and are therefore not affected by the Al^{VI} content. For chlorites with Al^{VI} below ≈1.0 apfu, the position of the 2250 nm absorption is systematically offset to lower wavelengths, yielding erroneously high Mg# estimates (e.g., Mg# 146 for Chl-16 at Al^{VI} 0.6, seen in Figure 2-5e). In such cases, the 1400, 2000, 2290 or 2330 nm absorptions can be used to estimate Mg#, as they are not affected by Al^{VI}.

In all cases, issues with compositional estimations can be identified by comparing estimates derived from several absorptions for a given mineral. If estimated compositions do not converge for all absorptions, one or more feature may be affected by interference and should be left out of the estimation process.

2.6 Conclusions

Quantitative relationships between SWIR reflectance spectra of biotite and chlorite and their mineral chemistry have been reported, for both Al^{VI} content and Mg#, and issues in the use of several spectral metrics have been discussed. Reflectance data were acquired using a commercially available hyperspectral instrument, with a 6.3 nm sampling rate and 10 nm bandwidth, which is comparable to current or upcoming satellite sensors (e.g., EnMAP, <8 nm sampling rate above 2200 nm, <12 nm bandwidth, Guanter et al., 2015). Although the instrument was used in a laboratory setting in this study, most of the absorptions described here fall within an atmospheric window (2000-2400 nm) that is exploited for remote sensing. The results derived from this study are therefore directly applicable to the use of hyperspectral data acquired from remote sensing platforms, whether obtained as panoramic observations (e.g. mine wall imaging), airborne or satellite data.

Existing economic geology studies make use of precise mineral composition data (e.g. Mg#), in terms that are familiar to the broader geological community. In some cases, a difference in biotite composition as small as 15 Mg# can represent the difference between unaltered background and mineralized samples (e.g., Selby & Nesbitt, 2000). Mineralogy derived from hyperspectral data is often reported in qualitative terms (e.g., Mg/Fe-rich chlorite), or quantitatively as the displacement of a given absorption position (in nanometres). However both qualifiers are not readily of value to geologists outside of the remote sensing community, who are more familiar with mineral compositional metrics (e.g. Mg#). Additionally, as there exists legacy mineralogical data for most mineral deposits, it is important to have the ability to link such data to information derived from hyperspectral data. The quantitative relationships presented in this study should therefore facilitate a two-way exchange of data between both communities, enhancing the use of legacy mineralogical data by the remote sensing community, and allowing the integration of hyperspectral data into the broader geological research community.

References

Armstrong, J. T. 1995. Citzaf-a package of correction programs for the quantitative Electron Microbeam X-Ray-Analysis of thick polished materials, thin-films, and particles. Microbeam Analysis, 4(3), 177-200.

Bailey, S. W. 1986. Re-evaluation of ordering and local charge-balance in Ia chlorite. The Canadian Mineralogist, 24(4), 649-654.

Beran, A. 2002.Infrared spectroscopy of micas. Reviews in Mineralogy and Geochemistry, 46(1), 351-369.

Biel, C., Subías, I., Acevedo, R. D., Yusta, I., & Velasco, F. 2012. Mineralogical, IR-spectral and geochemical monitoring of hydrothermal alteration in a deformed and metamorphosed Jurassic VMS deposit at Arroyo Rojo, Tierra del Fuego, Argentina. Journal of South American Earth Sciences, 35, 62-73.

Bishop, J. L., Lane, M. D., Dyar, M. D., & Brown, A. J. 2008. Reflectance and emission spectroscopy study of four groups of phyllosilicates: smectites, kaolinite-serpentines, chlorites and micas. Clay minerals, 43(1), 35-54.

Besson, G., & Drits, V. A. 1997. Refined relationships between chemical composition of dioctahedral fine-grained micaceous minerals and their infrared spectra within the OH stretching region. Part II: The main factors affecting OH vibrations and quantitative analysis. Clays and Clay Minerals, 45(2), 170-183.

Clark, R. N., King, T. V., Klejwa, M., Swayze, G. A., & Vergo, N. 1990.High spectral resolution reflectance spectroscopy of minerals. Journal of Geophysical Research: Solid Earth, 95(B8), 12653-12680.

Clark, R.N., Swayze, G.A., Gallagher, A., King, T.V.V and Calvin, W. M. 1993. The U. S. Geological Survey, Digital Spectral Library: Version 1: 0.2 to 3.0 m, U.S. Geological Survey, Open File Report 93-592.

Clark, R. N., & Roush, T. L. 1984. Reflectance spectroscopy: Quantitative analysis techniques for remote sensing applications. Journal of Geophysical Research: Solid Earth, 89(B7), 6329-6340.

Dalm, M., Buxton, M. W. N., & van Ruitenbeek, F. J. A. 2017. Discriminating ore and waste in a porphyry copper deposit using short-wavelength infrared (SWIR) hyperspectral imagery. Minerals Engineering, 105, 10-18.

Deer, W. A., Howie, R. A., & Zussman, J. (Eds.). 2009. Rock Forming Minerals: Layered Silicates Excluding Micas and Clay Minerals, Volume 3B. Geological Society of London.

Fleet, M. E., Deer, W. A., Howie, R. A., & Zussman, J. (Eds.). 2003. Rock-Forming Minerals: Micas, Volume 3A. Geological Society of London.

Farmer, V. C. 1968.Infrared spectroscopy in clay mineral studies. Clay minerals, 7(4), 373-387.

Guanter, L., Kaufmann, H., Segl, K., Foerster, S., Rogass, C., Chabrillat, S., Kuester, T., Hollstein, A., Rossner, G., Chlebek, C. and Straif, C., 2015. The EnMAP spaceborne imaging spectroscopy mission for earth observation. *Remote Sensing*, *7*(7), pp.8830-8857.

Harraden, C. L., McNulty, B. A., Gregory, M. J., & Lang, J. R. 2013. Shortwave infrared spectral analysis of hydrothermal alteration associated with the Pebble porphyry Copper-Gold-Molybdenum Deposit, Iliamna, Alaska. Economic Geology, 108(3), pp. 483-494.

Hunt, G. R. 1977. Spectral signatures of particulate minerals in the visible and near infrared. Geophysics, 42(3), 501-513.

Jones, S., Herrmann, W. and Gemmell, J.B., 2005. Short wavelength infrared spectral characteristics of the HW horizon: Implications for exploration in the Myra Falls volcanic-hosted massive sulfide camp, Vancouver Island, British Columbia, Canada. Economic Geology, 100(2), pp. 273-294.

King, T. V., & Clark, R. N. 1989. Spectral characteristics of chlorites and Mg-serpentines using high-resolution reflectance spectroscopy. Journal of Geophysical Research: Solid Earth, 94(B10), 13997-14008.

Laakso, K., Rivard, B., Peter, J.M., White, H.P., Maloley, M., Harris, J. and Rogge, D., 2015. Application of airborne, laboratory, and field hyperspectral methods to mineral exploration in the Canadian Arctic: recognition and characterization of volcanogenic massive sulfide-associated hydrothermal alteration in the Izok Lake deposit area, Nunavut, Canada. Economic Geology, 110(4), pp. 925-941.

MacLean, W. H., & Kranidiotis, P. 1987. Immobile elements as monitors of mass transfer in hydrothermal alteration; Phelps Dodge massive sulfide deposit, Matagami, Quebec. Economic Geology, 82(4), 951-962.

McLeod, R. L., Gabell, A. R., Green, A. A., & Gardavski, V. 1987. Chlorite infrared spectral data as proximity indicators of volcanogenic massive sulphide mineralization. In Pacific Rim Congress 87, Gold Coast, 1987, Proceedings (pp. 321-324).

Martínez-Alonso, S., Rustad, J.R. and Goetz, A.F., 2002. Ab initio quantum mechanical modeling of infrared vibrational frequencies of the OH group in dioctahedral phyllosilicates. Part II: Main physical factors governing the OH vibrations. American Mineralogist, 87(8-9), pp. 1224-1234.

Post, J. L., & Noble, P. N. 1993.The near-infrared combination band frequencies of dioctahedral smectites, micas, and illites. Clays and clay minerals, 41, 639-639.

Post, J. L., & Crawford, S. M. 2014.Uses of near-infared spectra for the identification of clay minerals. Applied Clay Science, 95, 383-387.

Redhammer, G. J., Beran, A., Schneider, J., Amthauer, G. & Lottermoser, W. 2000. Spectroscopic and structural properties of synthetic micas on the annite-siderophyllite binary: Synthesis, crystal structure refinement, Mössbauer, and infrared spectroscopy. American Mineralogist, 85(3-4), pp. 449-465.

Selby, D., & Nesbitt, B. E. 2000. Chemical composition of biotite from the Casino porphyry Cu–Au–Mo mineralization, Yukon, Canada: evaluation of magmatic and hydrothermal fluid chemistry. Chemical Geology, 171(1), 77-93.

Sillitoe, R. H. 2010. Porphyry copper systems. Economic geology, 105(1), 3-41.

Sun, Y., Seccombe, P. K., & Yang, K. 2001. Application of short-wave infrared spectroscopy to define alteration zones associated with the Elura zinc–lead–silver deposit, NSW, Australia. Journal of Geochemical Exploration, 73(1), 11-26.

van den Boomgaard, R., & van der Weij, R. 2001. Gaussian convolutions numerical approximations based on interpolation. In Scale-Space and Morphology in Computer Vision: Third International Conference, Scale-Space 2001 Vancouver, Canada, July 7–8, 2001 Proceedings 3 (pp. 205-214). Springer Berlin Heidelberg.

van der Meer, F., Kopačková, V., Koucká, L., van der Werff, H. M., van Ruitenbeek, F. J., & Bakker, W. H. 2018. Wavelength feature mapping as a proxy to mineral chemistry for investigating geologic systems: An example from the Rodalquilar epithermal system. International journal of applied earth observation and geoinformation, 64, 237-248.

Vedder, W. 1964 Correlations between infrared spectrum and chemical composition of mica. American Mineralogist, 49, 736–768.

Vogt, C., Lauterjung, J., & Fischer, R. X. 2002. Investigation of the Clay Fraction (< 2µm) of the Clay Minerals Society Reference Clays. Clays and Clay Minerals, 50(3), 388-400.

Wilkinson, J.J., Chang, Z., Cooke, D.R., Baker, M.J., Wilkinson, C.C., Inglis, S., Chen, H. and Gemmell, J.B., 2015. The chlorite proximitor: A new tool for detecting porphyry ore deposits. Journal of Geochemical Exploration, 152, pp.10-26.

Chapter 3 - Using hyperspectral imaging to vector towards mineralization at the Canadian Malartic gold deposit, Québec, Canada

3.1 Introduction

The hydrothermal fluids that are responsible for the formation of several types of mineral deposits can produce extensive hydrothermal alteration haloes in the surrounding host rocks. These alteration haloes typically consist of fine-grained assemblages of hydrated minerals, commonly including biotite, chlorite, and white mica. In many cases, telescoped mineralogical zones are present around these hydrothermal centers, which can serve as vectors to mineralization if correctly identified. Within each mineralogical zone, progressive changes in mineral chemistry can serve to further refine vectors to mineralization (e.g., Sillitoe, 2010; Wilkinson et al., 2015). Obtaining mineral chemistry, however, is typically a time-consuming process, requiring the careful preparation and examination of samples, usually followed by electron microprobe analysis (EMPA). In many cases, the fine-grained nature of the alteration minerals can hinder analysis, as suitably large grains (e.g. >5 µm) need to be located, if available at all. Unlike conventional analytical techniques, shortwave infrared (SWIR) reflectance spectroscopy is not negatively impacted by the fine-grained nature of alteration minerals (Hunt and Salisbury, 1970), and is therefore an ideal tool for the rapid identification and characterization of alteration zones in hydrothermal mineral deposits.

In the SWIR reflectance spectra of hydrated minerals, cation-OH bonds produce characteristic absorption features, which can be used to identify mineralogy (Hunt, 1977; Clark et al., 1990), and in many cases the position of these characteristic absorption features can also be used to estimate mineral chemistry. Typically, the Al_2-OH absorption of white mica near 2200 nm is used to estimate its Al^{VI} content (Post and Noble, 1993; Duke, 1994; Swayze et al., 2014), with the absorption position varying from 2190 nm for Al-rich (muscovitic), to 2215 nm for Al-poor (phengitic) white micas. Similarly, the Al(Mg,Fe)-OH absorption of biotite near 2250 nm (Besson and Drits, 1997; Martinez-Alonso et al., 2002; Bishop et al., 2008) can be used to estimate its Mg# (molar Mg/[Mg+Fe]), with the position varying from 2241 nm for Mg# 100 to 2260 nm for Mg# 0 (Lypaczewski and Rivard, 2018).

Because reflectance data can be acquired from rock surfaces in a few seconds, and require no sample preparation, spectral datasets can be far more extensive than datasets obtained using conventional analytical techniques. Spectroscopic studies can therefore rapidly cover large geographical areas with a high sampling density. For example, Duke and Lewis (2010) mapped metamorphic changes in white mica chemistry from 1036 SWIR point measurements, acquired in an area of several hundred square kilometers. In an exploration setting, Laakso et al. (2016) acquired over a thousand SWIR point measurements at regular intervals on drill core, as well as on outcrops, and reported that Al-rich white mica and Mg-rich chlorite were associated with alteration. In a laboratory setting, line-scanners (e.g., HyLogger-3, Schodlok et al., 2016) can provide continuous spectral measurements from drill core, and intervals of several thousand or tens of thousands of meters can be rapidly investigated (e.g., Arne et al., 2016; Mauger et al., 2016; Wells et al., 2016).

While point or line measurements are useful to delineate large-scale mineralogical patterns, the lack of spatial and textural context of such data yields limited information on small-scale mineralogical variability, for example between fine sedimentary layers, or between veins, vein selvages, and host-rocks. Recently, several studies in various geological settings have reported investigations of drill core using imaging spectrometers, which provide spectral data at high spatial resolution (≈1 mm/pixel). The resulting spectral imagery thus allows the examination of mineralogical changes within their textural context, which can reveal information that cannot be obtained from point or line-scan measurements. For example, Speta et al. (2016) acquired high-resolution hyperspectral imagery for 136 m of oil-saturated drill core, and were able to map small-scale sedimentary and biogenic features that were not visible to the naked eye. In a mineral exploration setting, Mathieu et al. (2017) investigated 16 core samples from the Cigar Lake unconformity-related uranium deposit, and were able to detect changes in alteration mineralogy, as well as textural features such as foliation and veining. Other studies presenting imaging data include investigations of porphyry-Cu deposits (Dalm et al., 2017; Graham et al., 2018), sapphire-bearing marbles (Turner et al., 2017), and an investigation of the use of epidote mineral chemistry as a tool for exploration in an Archean gold deposit (Roache et al., 2011).

In this study, imaging spectroscopy is used to investigate the variability of biotite and white mica mineral chemistry at the Canadian Malartic gold deposit, an Archean gold deposit in the Abitibi region of Québec, Canada. The deposit predominantly is hosted in the Pontiac metasedimentary rocks, near the regional Cadillac-Larder Lake deformation zone (CLLDZ) (Figure 3-1), which has recently been investigated in several studies. The most recent genetic models have been proposed by Helt et al. (2014) and De Souza et al. (2015, 2016), and the structural setting has been revised in Perrouty et al. (2017). Metamorphism in the Pontiac metasedimentary rocks, and geochemical and mineralogical alteration markers around the Canadian Malartic deposit were described in Gaillard et al. (2018) and Perrouty et al. (2018). Physical properties of the metasedimentary rocks were examined in Bérubé et al. (2018), and regional-scale metamorphism has been investigated by Piette-Lauzière et al. (2019). It was reported that the composition of all minerals in the Pontiac metasedimentary rocks is affected by a regional metamorphic gradient, but biotite and white mica compositions are also strongly affected by hydrothermal alteration related to the deposit, therefore can serve as vectors to mineralization (Gaillard et al., 2018).

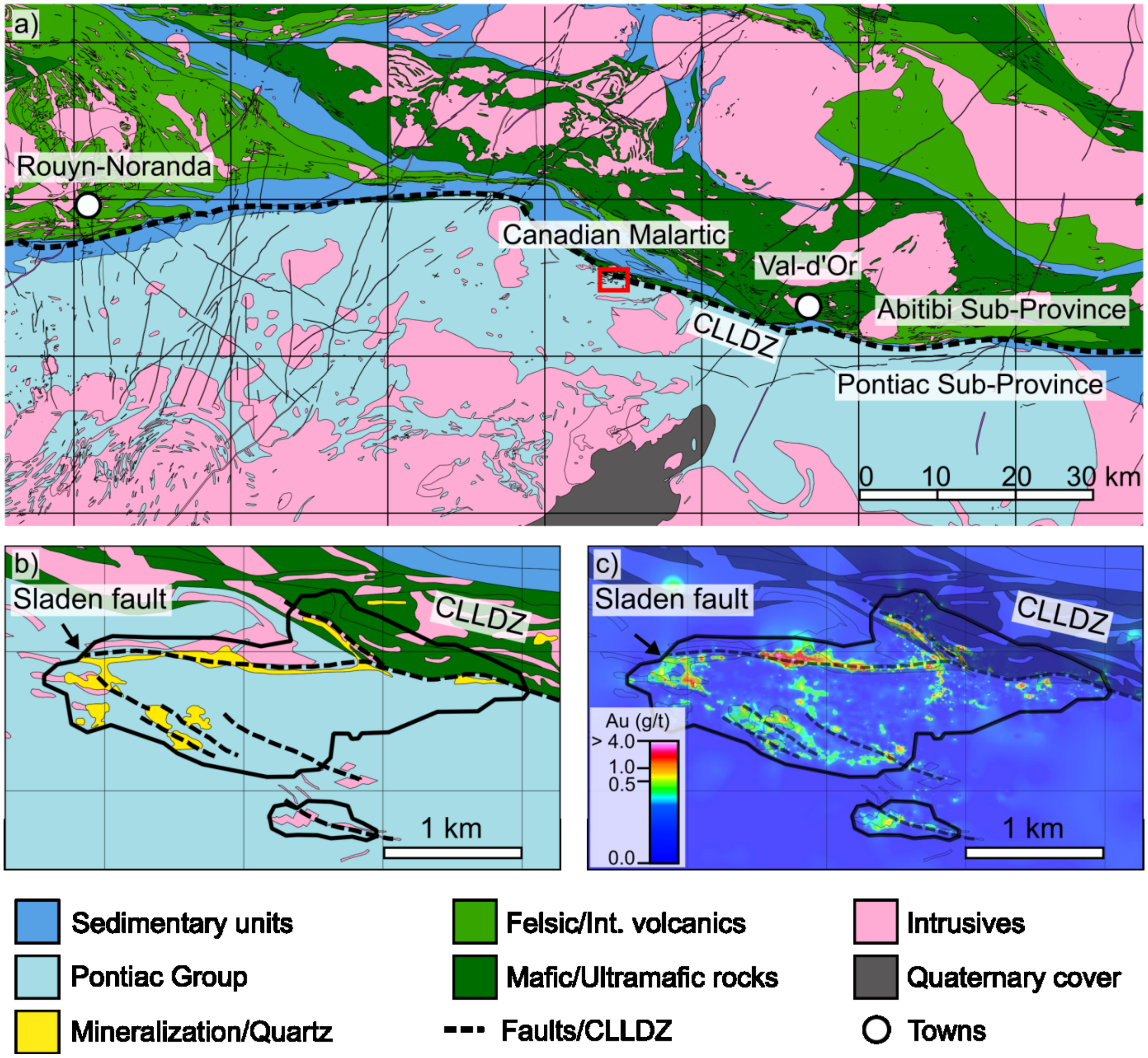

Figure 3-1 *Geological maps of the Abitibi and Pontiac Subprovinces and of the deposit area. a) Regional geological map highlighting the location of the Canadian Malartic deposit, at the contact between the Abitibi and Pontiac Subprovinces. b) Geological map showing the location of the open pit, primarily within the Pontiac metasedimentary rocks directly south of the CLLDZ. c) Distribution of gold grades within the deposit (modified from Gaillard et al., 2018; interpolated from Canadian Malartic Corporation gold assay data). Geological maps modified after Ministère des Ressources Naturelles du Québec, SIGEOM Database, 2016, http://sigeom.mines.gouv.qc.ca/*

In all these studies, however, observations are made using punctual samples, from thin sections (2 cm by 4 cm) selected from larger hand samples (15 to 30 cm), capturing only a fraction of the mineralogical variability present within a given sample. These thin sections provide little information on, for example, the variation of mineral chemistry between alternating sedimentary beds, or on the extent of alteration selvages around veins and veinlets. In turn, the parent hand samples are selected in the field or in drill core with the assumption of continuity between sampling points, but may capture only a fraction of the mineralogical variability present within a deposit, particularly if the sampling is performed at large intervals. The main goal of this study is therefore to visualize the mineralogical variability of biotite and white mica at a variety of scales using imaging spectroscopy. At the scale of a sample, mineralogical variability is investigated using high-resolution hyperspectral imagery, which provides detailed information on small-scale changes related to protolith composition, for example between alternating sedimentary beds, or to hydrothermal alteration, such as between vein, vein selvage and wall-rocks. At the scale of the deposit, similar data acquired on entire drill cores provide details on the continuity and scale of mineralogical changes related to hydrothermal alteration surrounding mineralized intervals. Insights gained from these high-resolution hyperspectral data are in turn used to optimize regional-scale measurement strategies using point spectrometers. Here, a large collection of SWIR point data acquired from outcrops in the Pontiac metasedimentary rocks is used to identify mineralogical changes related to regional metamorphic gradients, and is then used to delineate regional-scale hydrothermal alteration patterns. Because the regional Cadillac-Larder Lake Deformation zone has a strike length exceeding 200 km (Robert, 1989), a large part of which is in direct contact to the Pontiac metasedimentary rocks (themselves covering over

2500 km^2), the results presented in this study can guide exploration within this, or in similar geological environments.

3.2 Background

3.2.1 Regional geology

The Archean-age Canadian Malartic gold deposit is located in the gold-endowed Abitibi Greenstone belt of the southern Superior Province, in Québec, Canada. The deposit is situated within and immediately south of the east-west trending regional Cadillac-Larder Lake Deformation zone (CLLDZ), a zone of steeply dipping faults defining the boundary between the volcano-sedimentary assemblage of the Abitibi Subprovince to the north, and the dominantly sedimentary Pontiac Subprovince to the south (Robert 1989; Helt et al., 2014; Figure 3-1). In the vicinity of the deposit, north of the CLLDZ, the Abitibi Subprovince consists of the Cadillac Group greywackes to mudstones and Timiskaming-type conglomerates (2678–2670 Ma, Corfu et al., 1991; Ayer et al., 2005). Near the deposit, the Piché Group mafic to ultramafic volcanic rocks are limited to, and locally define the CLLDZ (Helt et al., 2014). South, across the deformation zone, the Pontiac Group metasedimentary rocks consist of a turbiditic sequence of mudstones to greywackes (2685-2682 Ma, Davis 2002). The latter two units are crosscut by numerous quartz monzodiorite to granodioritic plutons and dykes (2678-2676 Ma, De Souza et al., 2015; 2016). Regional metamorphism, increasing in intensity southwards, is estimated to have peaked between 2677 and 2643 Ma (Powell et al., 1995), and more recently dated to 2657.5 ± 4.4 Ma (Piette-Lauzière et al., 2019). This also broadly corresponds to a major phase of north-south compression that generated penetrative east-west schistosity (Wilkinson et al., 1999). The Cadillac and Piché Groups north of the deposit are at mid-greenschist facies (chlorite zone), whereas the Pontiac Group sediments within the open pit of the Canadian Malartic mine are at upper-greenschist facies (biotite zone). The amphibolite facies occurs roughly 1.5 km south of the deposit, and is typically marked by the appearance of garnet; the staurolite appearing roughly 1 km further south (Gaillard et al., 2018; Piette-Lauzière et al., 2019).

3.2.2 Deposit geology

Canadian Malartic is a large tonnage, low-grade deposit (204 Mt, 1.08 g/t Au, Gaillard et al., 2018) exploited as an open pit mine roughly 3 km by 1 km in size, situated partly within the Piché Group metavolcanic rocks (the CLLDZ), but primarily within the Pontiac Group metasedimentary rocks at the upper-greenschist facies (Figure 3-1b). Unaltered metasedimentary rocks consist of quartz, plagioclase, white mica, biotite and/or chlorite, forming interlayered greenish-grey mudstones to brownish-grey greywackes, with beds ranging from a few millimeters to several meters in thickness. White mica is present predominantly in the fine-grained (mudstone) beds, and its mineral chemistry varies with metamorphic grade, with Al-rich (muscovitic) white mica occurring at higher grades. In the upper greenschist facies rocks of the northernmost Pontiac Group (near the deposit), metamorphic white mica is a phengitic-muscovite at around 1.7 Al^{VI} apfu (based on a stoichiometry of 11 O). At higher metamorphic grades, white mica becomes progressively Al^{VI}-enriched, reaching 1.9 Al^{VI} apfu in the amphibolite facies roughly 1.5 km south of the deposit. Biotite (± chl), on the other hand, is present in all sedimentary layers, and it's Mg# does not change with metamorphic grade, remaining at around Mg# 55-60 in all unaltered Pontiac metasedimentary rocks. Felsic intrusions or dykes, ranging from quartz monzodiorite to granodiorite crosscut the Pontiac and Piché Group rocks (Trudel and Sauvé, 1992; Helt et al., 2014), and consist of plagioclase and minor orthoclase phenocrysts (<6 mm) in a groundmass of quartz, plagioclase, biotite and chlorite (Gaillard et al., 2018).

Mineralization at Canadian Malartic consists of disseminated free gold grains (<20 µm), occurring within stockworks of quartz-biotite-microcline-carbonate ± pyrite veinlets (*v2* veinlets, Helt et al., 2014; de Souza et al., 2015, 2016; Gaillard et al., 2018), or in the surrounding pervasively altered host rocks. The distribution of the mineralization is structurally controlled by deformation zones or contacts to competent units (dykes, plutons), generally forming a central high-grade ore zone (>1 g/t) surrounded by a pervasive semi-continuous low-grade ore shell (0.3-1.0 g/t). The main mineralized structure within the open pit, the Sladen Fault, is an E-W trending subvertical shear zone that marks the contact between the Pontiac metasedimentary rocks and porphyritic intrusions in the western portion of the open pit, or to the Piché group volcanics in the eastern section of the pit (Sansfaçon et al., 1987; de Souza et al., 2016; Perrouty et al., 2017; Figure 3-1c). Although it may not always be entirely preserved, the typical hydrothermal alteration sequence in the Pontiac metasedimentary rocks progresses from a proximal beige-brown potassic alteration zone (microcline-albite-phlogopite ± quartz-carbonate-pyrite), and grades into a distal blueish-grey potassic-sericitic zone (abundant phengitic white mica and Mg-rich biotite, and also microcline, albite, quartz, calcite, pyrite). A central brecciated and/or mylonitized zone (interpreted to delineate the main fluid pathways) may be present, and can locally be highly silicified (quartz-flooded). All zones can be variably affected by retrograde chloritization (Helt et al., 2014; Gaillard et al., 2018). In the central brecciated zone, biotite may be absent, and where present it is Mg-rich (Mg# >90). Biotite compositions decreases to lower Mg# in the potassic alteration zone, and reaches background compositions of Mg# 55-60 within or shortly outside of the potassic-sericitic zone. White mica is commonly absent in the brecciated zone, and can be present in the potassic zone as phengite (Al^{VI} <1.6 apfu), which gradually progresses to higher-Al background white mica compositions (Al^{VI} >1.7 apfu) in the potassic-sericitic zone (Gaillard et al., 2018). The variability of mineral chemistry is explained by changes in the physico-chemical parameters (ΣaS, fO2, aK+ and/or pH) of the hydrothermal fluids that were progressively buffered by interactions with host rocks (as detailed in Gaillard et al., 2018). In the core of the alteration zone, in close vicinity to the main fluid pathways, the sequestration of Fe by pyrite caused high-Mg# biotite to form, and the buffering of the mildly alkaline hydrothermal fluid to near neutral conditions caused progressive changes in white mica compositions (Heiligmann et al., 2008; Gaillard et al., 2018).

3.3 Methods

3.3.1 Spectral measurements and related sample suites

To capture the small-scale mineralogical changes related to hydrothermal alteration, and to distinguish them from large-scale changes related to metamorphism, three types of spectral datasets were acquired, each covering a progressively larger geographical area, but with progressively less textural details.

The first spectral dataset was obtained for a small geographical area within the deposit, and consists of imagery acquired from over 2000 meters of drill core selected from 9 drill holes. These drill holes are located within and in the immediate vicinity (1 to 2 km) of the open pit, and were selected because they cross major mineralized zones. This dataset is used to provide detailed mineralogical sections of the deposit, encompassing the main fluid pathways and extending to the weakly altered fringes of the alteration halo.

To provide mineralogical information on larger geographical scales, over 500 field and drill core samples (approximately 30 cm by 5 cm in size) were collected from a 20 km by 10 km area surrounding the deposit. Collectively, these samples will better define the extent of the hydrothermal alteration halo around the deposit. Samples collected in the field were cut to include a surface perpendicular to sedimentary bedding, and in some cases included veins or veinlets. The high-resolution spectral imagery of these samples provide insights into the small-scale mineralogical changes in Pontiac metasedimentary rocks, for example highlighting differences between consecutive sedimentary layers in unaltered samples, or changes around veins and veinlets in hydrothermally altered rocks. From this sample suite, homogeneous pieces (excluding obvious veins and veinlets) were selected for geochemical analysis, with Au content determined by ICP-MS after digestion in aqua regia (ALS, British Columbia, Canada). A total of 241 polished thin sections were also prepared from these samples for petrographic and electron microprobe analysis, and spectral imagery was acquired on the corresponding thin section offcuts.

Lastly, over 1500 measurements were collected with a point spectrometer directly on outcrops (primarily in the metasedimentary rocks), encompassing an area of 50 km by 15 km surrounding the deposit. These data offer no textural context (no imaging), but offer a rapid assessment of regional scale variability in mineralogy. Given that surface bedrock no longer exists within the open pit, point data were also acquired from the tops of 326 archived drill holes (within the first 30 m of drill core). In the vicinity of the open-pit, several hundred data points were taken at short intervals on outcrops (every 5 to 20 m) to better define small-scale changes in the proximal alteration halo. These high-density data points are also needed to deconvolve the effects of metamorphism from those of hydrothermal alteration on mineral chemistry within and near the open pit. Sampling was also prioritized along the CLLDZ (up to 12 km northwest of the open pit), with outcrops measured every 50 to 250 meters. Finally, point data were acquired at a sampling interval of 200 to 500 meters along three regional transects (each 10 to 15 km long) situated 20 to 30 km away from the deposit. These transects are roughly perpendicular to the metamorphic isograds, and outline the effects of regional metamorphism on mineral chemistry. The primary goal of these point data was to define the background mineral composition of the Pontiac metasedimentary rocks, and thus veins, veinlets and other visible heterogeneities were avoided. On larger outcrops, the finer grained beds (mudstone, siltstone) were preferred where possible because they were generally white mica bearing, whereas coarser grained units (greywackes) were typically white mica free. A limited number of data were also taken in felsic to intermediate dykes and intrusive units. In all cases, because of an extensive (but thin) lichen cover, outcrops were broken with a hammer to expose a fresh rock surface for data collection.

3.3.2 Collection of EMPA data

Regressions between mineral chemistry and the position of absorption features in the SWIR have been provided in several studies, including McLeod et al (1987) for chlorite, Lypaczewski and Rivard (2018) for biotite and chlorite, and Swayze et al. (2014) for white mica. To insure these calibrations are accurate for the samples investigated here, new regressions were established from a subset of 67 of the 241 available thin sections of Canadian Malartic samples. This subset represents thin section offcuts that were found to be mostly homogeneous based on hyperspectral imagery, and which had negligible interference from chlorite. Electron microprobe analysis (EMPA) data was acquired using wavelength dispersive spectroscopy (WDS) on a JEOL JXA-8900L instrument at McGill University, with instrumental conditions set at a 20 nA beam current, a 15 kV acceleration voltage, and a 5µm probe diameter. EMPA data were acquired across the entirety of the thin section for approximately 10 randomly selected crystals per sample. A total of 40 samples were analyzed for white mica and 67 samples for biotite.

3.3.3 Infrared Spectroscopy

3.3.3.1 Collection of IR spectra

A point spectrometer and two imaging spectrometers were used to acquire the infrared reflectance datasets. Point measurements were acquired directly on outcrops using a portable ASD FieldSpec 3, which operates in the VNIR-SWIR (350-2500 nm). Data is output at a sampling interval of 1 nm, with a spectral resolution better than 10 nm across the entire spectral range (ASD Inc., 2010). The instrument was equipped with a contact probe with an internal illumination source, which provides stable illumination to an area 20 mm in diameter. The integration time for each measurement was set at 35 ms, and 30 measurements were averaged for each data point, resulting in a total acquisition time of approximately 1 s per data point. Reflectance data were obtained by subtracting the dark current and then normalizing the radiance measurement of the target to that of a Spectralon™ white panel (99% reflectance). To minimize drift in reflectance (absolute intensity), the white reference was measured roughly every hour. Spectral drift (i.e., changes in reported absorption positions) was assessed using the spectrum of a clear polystyrene sample measured daily during the month long field season. The main absorptions of polystyrene (≈ 1214, 1729, 2311 nm) were observed to be within 0.2 nm for all measurements, thus indicating the absence of a detectable drift in the measurements.

Spectral imagery in the SWIR (1000-2500 nm) was obtained in the laboratory using a Specim SisuROCK™ hyperspectral scanner (a line-scan imager) at the University of Alberta. The scanner contains a 256 spectral by 320 spatial pixels mercury-cadmium-telluride (MCT) detector array that acquires data at a 6.3 nm sampling interval and a 10 nm spectral bandwidth. The instrument was equipped with either an OLES56 (high-resolution) or an OLES15 (low-resolution) lens, which yielded a spatial resolution between 0.2-0.4 mm/pixel and 1-2 mm/pixel, respectively. Dark current and a 99% reflectance Spectralon™ white panel were measured at the beginning of each data acquisition sequence, and radiance data of the geological target were converted to reflectance by subtracting dark current, and then by normalizing to the radiance data of the white panel. Drill cores in 1.5 m long wooden core boxes (three rows per box) were scanned at 1mm/pixel using the low-resolution lens. Field samples and selected core intervals were scanned using the high-resolution lens (0.4 mm/pixel), and where available, corresponding thin section offcuts were scanned at 0.2 mm/pixel. In all cases, because of signal-to-noise (SNR) considerations, data were acquired at 4x resolution along the scan direction (i.e., pixels were acquired at 1.0 mm by 0.25 mm), and 4 pixels were averaged to obtain the final data with square 1 mm by 1 mm pixels).

Spectral imagery was also acquired in the longwave infrared (LWIR, 8000-12000 nm) using a Specim LWIR-HS hyperspectral scanner. This instrument is equipped with an uncooled micro-bolometer array that acquires data in 30 bands, yielding an average sampling interval of 150 nm, at a 400 nm spectral resolution. A warm-up time of 45 to 60 minutes was allowed before the start of each scanning session for the light source (heat lamps) to reach operating temperatures. Dark current and an anodized aluminium panel (white reference) were measured at the beginning of each acquisition sequence, and were used to obtain reflectance data. This instrument was not equipped with interchangeable lenses, and all data were therefore acquired at a resolution of 1 mm/pixel.

3.3.3.2 Spectral data analysis

In reflectance spectra of minerals, the presence of characteristic absorptions can be used to identify mineralogy (Hunt, 1977; Clark et al., 1990). In addition, for certain minerals, the position of some absorptions can vary by 10 nm to 40 nm based on mineral chemistry (Post and Noble, 1993; Duke 1994; Lypaczewski and Rivard, 2018). The analysis of spectral data therefore requires the detection of the presence of absorption features, and the determination of the exact position of these absorptions. Given the relatively coarse 6.3 nm sampling interval of the imaging spectrometer, spectra need to be interpolated in order to derive precise (and ultimately accurate) absorption positions. Here, data analysis is performed using the method described in Lypaczewski and Rivard (2018), implemented using in-house Python 3 software (van Rossum, 1995) utilizing SciPy (Jones et al., 2001) and NumPy (Oliphant, 2006) packages. For hyperspectral imagery, spectra are analyzed on a per-pixel basis (i.e., a single spectrum). Spectra are first linearly interpolated to an arbitrarily high sampling rate (using `scipy.interpolate.interp1d`, Jones et al., 2001), and are then smoothed by convolution with a Gaussian function (function `numpy.convolve,` Oliphant, 2006). Absorption feature strength and exact position are then retrieved from the maxima of the second derivative of the convolved spectra (i.e., derivative analysis, function `scipy.misc.derivative,` Jones et al., 2001). For hyperspectral imagery, this information is then displayed using a color-coded scale binned to 1 nm intervals (presented alongside imagery), where color represents absorption position, and the lightness of the color represents the relative strength of the second derivative.

The point data obtained from the ASD FieldSpec 3 instrument (at a 1 nm sampling interval) are interpolated to 0.1 nm before convolution, but because of computation time considerations, spectra from hyperspectral imagery from the Specim SisuROCK (6.3 nm sampling interval) are only interpolated to 1 nm before convolution. To further refine the absorption position on a sample level (e.g., for an image of 120 x 230 pixels of a thin section offcut), the average absorption position of all pixels is reported, calculated as the absorption position for each pixel, weighed by the absorption strength of the given pixel. In Lypaczewski and Rivard (2018), where data consisted of averaged spectra which presented low noise levels, convolution was performed with a Gaussian function with a full width half maximum (FWHM) of 10 nm. Here, because the absorption position is determined for the spectrum of every image pixel, which inherently have a relatively low SNR, a Gaussian function with a FWHM of 20 to 30 nm is required to adequately perform smoothing and reduce noise.

3.3.3.3 Instrument calibration

As indicated in Chang and Yang (2012), retrieved absorption positions can vary by a few nanometers between different instruments. A thorough instrumental calibration is therefore required in order to derive accurate absorption positions from multiple sources. To determine the degree (if any) of inter-instrumental variability, and to assess the effectiveness of the spectral interpolation methodology described in the previous section, reflectance data were acquired on a suite of 54 thin section offcuts containing white mica using both the Specim SisuROCK and the ASD FieldSpec 3 Max instruments. For each sample, the positions of the 2200 nm absorption obtained from both instruments are presented in Figure 3-2.

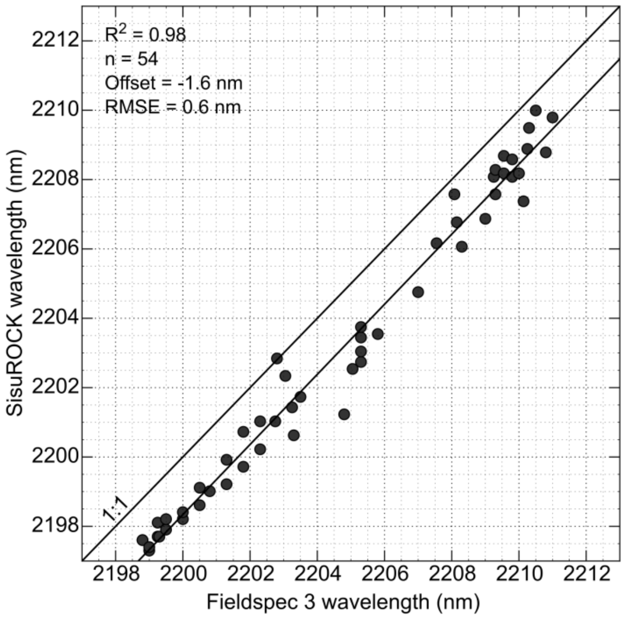

Figure 3-2 *Comparison between the positions of the 2200 nm absorption for 54 thin section offcuts, derived from the Specim SisuROCK and ASD Fieldspec 3 instruments.*

The lack of clustering of data around the original SisuROCK sampling points (every 6.3 nm), and the good correlation to more finely sampled (1 nm) FieldSpec 3 data indicate that the spectral interpolation methodology performs adequately. Furthermore, as fully described in section 3.5 of Lypaczewski and Rivard (2018), the effectiveness of the interpolation was also assessed by acquiring data on a National Institute of Standards and Technology (NIST) referenced Mylar standard. It was reported that, after interpolation of the original 6.3 nm sampling rate, derived absorption positions near 1128, 1660, 1951, 2130, and 2330 nm were all within 0.5 nm of the NIST referenced values. This calibration also served to confirm that the values reported by the imaging spectrometer are accurate to at least ±1 nm, corresponding to the NIST referenced error margin. Taking into account that the SisuROCK data are accurate, Figure 3-2 shows that the Fieldspec 3 data are systematically offset by 1.6 nm to longer wavelengths, relative to the SisuROCK data. Consequently, all Fieldspec 3 data in this study are corrected by subtracting a constant 1.6 nm value to the derived absorption positions. Finally, the reproducibility of the measurements was assessed by acquiring data on one of the thin section offcuts over multiple measurements spanning multiple days, ensuring that the room temperature remained constant. Over a total of 40 measurements, the derived absorption position spanned a total range of 0.7 nm, with a standard deviation of < 0.2 nm.

3.3.3.4 Mineral identification

In the SWIR, dominant absorptions are observed around 1410, 2200, 2350 and 2430 nm for white mica (Clark, 1990; Besson and Drits, 1997; Martinez-Alonzo et al., 2002), around 1390, 2250, 2330 and 2380 nm for biotite (Clark, 1990; Bishop et al., 2008; Lypaczewski and Rivard, 2018), and around 1395, 2000, 2250, and 2330 nm for chlorite (McLeod et al., 1987, Clark 1990, Bishop et al., 2008, Lypaczewski and Rivard, 2018). All absorptions shift in position by 10 to 40 nm with mineral chemistry, and some also vary in strength (the spectral response of biotite and chlorite is discussed at length in Lypaczewski and Rivard, 2018).

The Pontiac metasedimentary rocks investigated here include spectrally active white mica, biotite, chlorite, and in some cases, minor amounts of carbonates. The presence of white mica can therefore be identified by the Al_2-OH absorption near 2200 nm, as no other minerals with an absorption near this position are present (e.g., smectite, kaolinite). Similarly, biotite and/or chlorite can be identified by the presence of an Al(Mg,Fe)-OH absorption near 2250 nm, as the samples in this study do not contain other minerals with an absorption near 2250 nm (e.g., epidote, tourmaline). However, biotite and chlorite have similar reflectance spectra, with mutually interfering absorptions. A rule-based method was proposed in Lypaczewski and Rivard (2018) to determine if a given spectrum is biotite or chlorite-rich. This methodology is applied here, where the presence of the 2250 nm absorption is first used to detect pixels containing either biotite or chlorite, and spectra that also have an absorption at 2380 nm are classified as biotite, whereas those that also have a broad absorption at 2000 nm are classified as chlorite.

The accuracy of this rule-based method is qualitatively assessed in Figure 3-3, which compares results of the classification of SWIR imagery of a thin-section offcut to the mineralogy detected from mineral liberation analysis (MLA) in the corresponding polished thin-section. A good agreement is seen in the distribution of biotite and chlorite as determined by MLA data and classified SWIR imagery, where the central portion of the sample (background) is biotite-rich, and veinlet selvages are chlorite-rich.

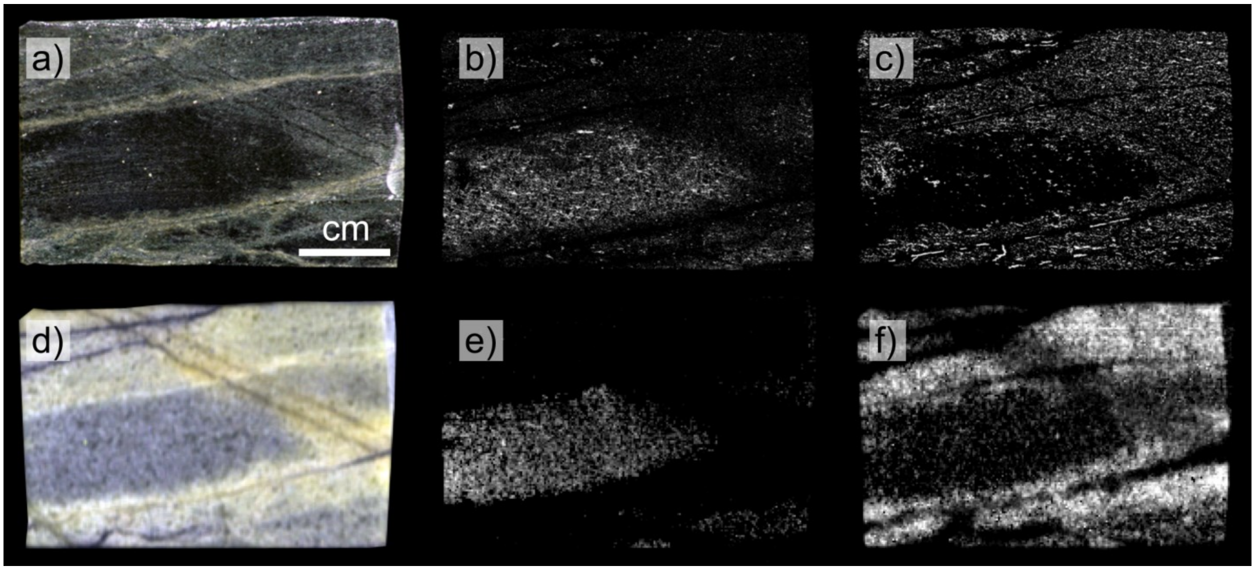

Figure 3-3 *Comparison of the detection of biotite and chlorite by mineral liberation analysis (MLA, top) and hyperspectral imaging (bottom). a) Photograph of the thin section offcut, b) MLA showing biotite, c) MLA showing chlorite, d) SWIR false color image at 0.2 mm/pixel, e) Hyperspectral image showing biotite, and f) showing chlorite.*

In the LWIR, quartz is identified by the presence of a strong reflectance peak near 9200 nm. As no other minerals present a peak at this position, the peak strength is used to directly estimate the relative abundance of quartz in imagery.

3.3.3.5 Estimation of mineral chemistry from absorption positions

The mineral chemistry of white mica is generally estimated from the position of the main Al_2-OH absorption at 2200 nm, and the Mg# of biotite can be estimated from the Al(Mg,Fe)-OH absorption, near 2250 nm, provided it is Al-bearing (Post and Noble, 1993; Lypaczewski and Rivard, 2018). Correlations between Al^{VI} content and the 2200 nm absorption position of white mica were presented in Post and Noble (1993), and have been applied to mapping hydrothermal systems with data obtained either from imaging spectrometers (e.g., Laukamp et al., 2011, van Ruitenbeek et al., 2012; Graham et al., 2018) or from point spectrometers (e.g., Harraden et al., 2013; Wells et al., 2016; Wang et al., 2017). Similarly, changes in chlorite or biotite composition derived from the 2250 nm absorption, have also been used to map hydrothermal systems, for example in McLeod et al. (1987), Jones et al. (2005), and Laakso et al. (2016).

Regression equations between the 2200 nm absorption and Al^{VI} content of white mica were more recently provided in Swayze et al. (2014), and equations to estimate the Mg# in biotite were provided in Lypaczewski and Rivard (2018). However, both studies made use of pure or nearly pure samples (laboratory standards or single crystals), whereas the majority of the samples in the current study consist of mineral mixtures. The resulting spectra can therefore present partially overlapping absorptions, which can potentially influence the estimation of their exact position. Additionally, because of the lower SNR of single pixel data, spectral smoothing is performed using a relatively wide Gaussian, which might further increase the overlap between closely spaced absorptions, for example in samples with mixtures of phengitic white mica

(≈ 2215 nm) and Mg-rich biotite (≈ 2245 nm). To assess whether mineral mixtures affect the estimation of the absorption position near 2200 nm, a regression line between the estimated white mica band position and the corresponding Al^{VI} content (from EMPA) was established using 40 white mica-rich samples from Canadian Malartic (Figure 3-4b) that also have significant amounts of biotite, chlorite and/or carbonates. The regression obtained from such mineral mixtures was found to closely match the regression provided in Swayze et al. (2014) for white mica standards (Figure 3-4b), indicating that mineral mixtures do not negatively affect the estimation of the white mica chemistry.

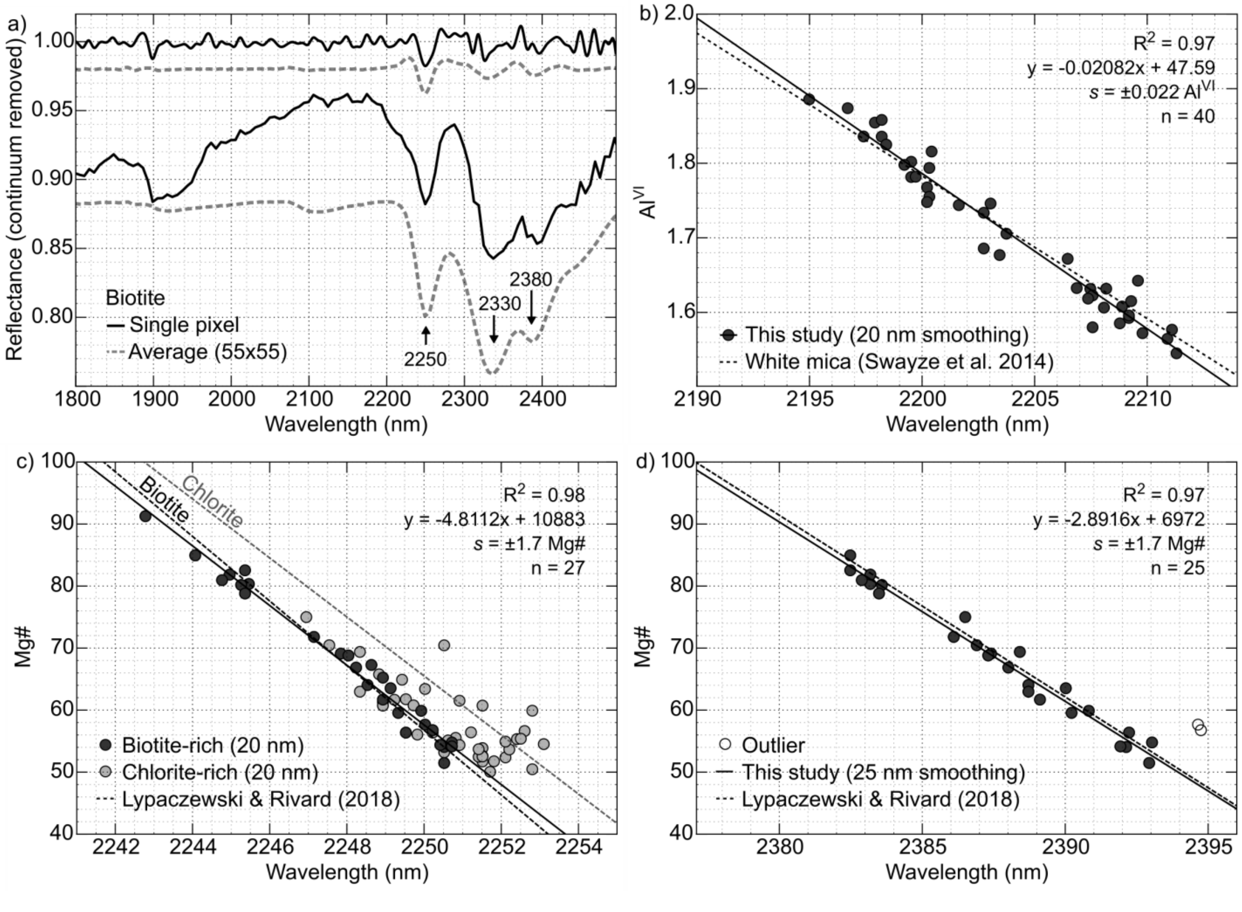

Figure 3-4 *Typical biotite spectrum, and correlations between mineral composition (from EMPA) and absorption position. a) Averaged (dashed line) and single pixel (solid line) biotite spectra, highlighting the lower-SNR of single pixel data. The negative of the second derivative*

for both spectra is plotted at the top, b) Correlation between the Al^{VI} content of white mica and the position of the 2200 nm Al_2-OH absorption, c) Correlation between the Mg# of biotite and the position of the 2250 nm absorption, d) Correlation between the Mg# of biotite and the position of the 2380 nm absorption.

Biotite and chlorite have entirely overlapping absorptions near 1400, 2250 and 2330 nm, but for an equivalent Mg#, chlorite has its absorptions shifted to slightly longer wavelengths relative to those of biotite (Lypaczewski and Rivard, 2018). In mineral mixtures, errors in the estimation of mineral chemistry of biotite may therefore occur if the effect of chlorite is not accounted for. To determine if the effect of interfering chlorite can be spectrally detected and mitigated, EMPA data was acquired for biotite in 67 samples containing variable amounts of chlorite. The samples were classified as being either biotite or chlorite-rich using the rule-based method applied to each pixel. A total of 40 samples with more than 33% of the pixels labeled as chlorite, or with less than 10% of pixels labeled as biotite were labeled as chlorite-rich, and were excluded from the biotite sample population. A regression line was then established between the position of the absorption at 2250 nm and the Mg# of biotite of biotite-rich samples (Figure 3-4c, black data points). This regression was found to closely follows the one established for pure biotite samples (Lypaczewski and Rivard, 2018), indicating that the interference from chlorite can effectively be spectrally detected and mitigated using the rule-based method. The samples labeled as chlorite-rich generally show longer absorption positions, as expected. Alternatively, biotite Mg# can be estimated (with no interference of chlorite) from the position of the 2380 nm absorption, as shown in Figure 3-4d, although this absorption is generally weaker and is more prone to noise than the one at 2250 nm.

3.4 Results

3.4.1 Variability of mineralogy and mineral chemistry at Canadian Malartic

A main objective of this study is to investigate changes in mineralogy related to protolith (in unaltered samples), and those related to hydrothermal alteration, for example between vein, vein halo and host-rock mineralogy. Figure 3-5 provides photographs and interpreted spectral imagery of typical unaltered, and weakly through highly hydrothermally altered samples. A representative sample of unaltered Pontiac metasedimentary rock (Figure 3-5a, K389402, <0.01 g/t Au) was collected approximately 3 km southwest of the deposit. As this is a channel sample taken from an exposed outcrop surface, a ≈1cm deep weathered rind is visible, particularly on the quartz vein (Figure 3-5a, right-end of the sample). The processed hyperspectral imagery shows that most of the sample is white mica-bearing (purple colors represent an absorption at ≈ 2196 nm, corresponding to 1.9 Al^{VI} apfu), and, importantly, that no changes in composition are present between the weathered surface (top) and fresh rock. Thus, any measurement taken on the weathered surface using a point spectrometer would compare to those obtained from unweathered drill core samples. In most of the samples in this study, including the one shown in Figure 3-5a, the layers free of white mica (corresponding mainly to greywackes) are generally biotite-rich (here the green color represents an absorption at ≈2250 nm, or Mg# 58), whereas the layers containing white mica (mudstones) are generally chlorite-rich (Figure 3-5a, the biotite image becomes darker in the left portion).

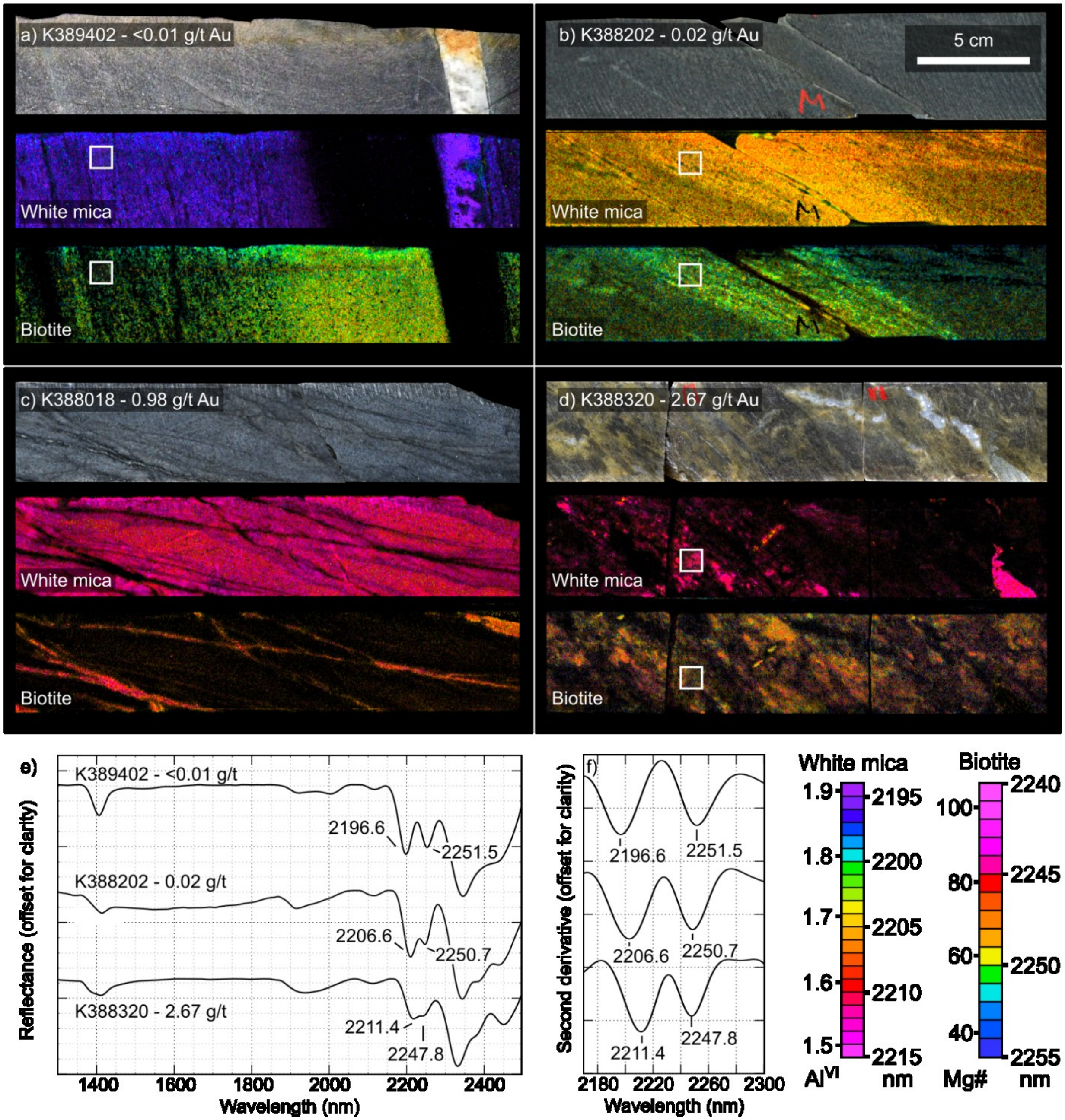

Figure 3-5 *Photograph and spectral imagery of four representative Pontiac Group metasedimentary rock samples collected near and within the deposit. The panel for each sample displays a photograph at the top, imagery conveying the absorption wavelength position of white mica (middle) and biotite (bottom), respectively. The color legends are shown in the lower right. Panel a) K388402 (<0.01 g/t Au) is a typical unaltered, distal sample showing metamorphic white mica (2197 nm) occurring only in specific beds. Panel b) K388202 (0.02 g/t Au) is altered, containing disseminated pyrite, but is unmineralized. Alteration is not strongly visible, but white mica is phengitic (2206 nm). Panel c) K388018 (0.98 g/t Au) is mineralized and strongly altered, showing greyish-blue sericitization (highly phengitic, 2211 nm). Panel d) K388320 (2.67 g/t Au)*

is mineralized and shows the most intense (beige-brown) proximal alteration assemblage. Panel e) displays average spectra (15 by 15 pixels, continuum removed), from the locations marked by white boxes in panels a, b and d. Panel f) displays a portion of the spectra as the negative of the second derivative, highlighting the change in absorption positions, and the separability of the partially overlapping absorptions. Additional sample imagery is available in Appendix 2A.

A weakly altered but unmineralized sample (K388202, 0.02 g/t Au) is shown in Figure 3-5b. This portion of core was collected a few meters from a highly mineralized zone (>1 g/t Au), and contains minor amounts of sulphides, but alteration is otherwise difficult to identify visually. The estimated white mica composition is phengitic (2206 nm, 1.66 Al^{VI} apfu), indicating moderate levels of hydrothermal alteration. The composition of biotite remains unchanged from background values present in the prior sample (2250 nm or Mg# 58), highlighting that white mica alteration extends further away from hydrothermal fluid pathways than biotite alteration. A strongly altered and mineralized sample (K388018 - 0.98 g/t Au) is shown in Figure 3-5c and displays a greyish-blue color typical of pervasive potassic-sericitic alteration (distal alteration, Gaillard et al., 2018). This alteration type commonly results in an enrichment in highly phengitic white mica (2211 nm, 1.6 Al^{VI} apfu), and generally occurs within and immediately adjacent to strongly mineralized intervals. Part of the stockwork of auriferous quartz-biotite-microcline-carbonate ± pyrite (*v2*) mineralized veinlets is visible in this sample, detectable in the biotite imagery as highly Mg-rich biotite veinlets (2247 nm, Mg# 80). In this sample, the biotite alteration is restricted to the veinlets, but the phengitic alteration halo is pervasive, with host rocks showing phengite on scales of up to several meters away from veinlet-rich zones. Finally, an example of the most intense alteration type is shown in Figure 3-5d (proximal alteration, Gaillard et al., 2018). This brownish-beige alteration (potassic alteration) occurs exclusively in central portions of mineralized intervals (at most a few tens of meters wide). In these zones, white mica may be entirely absent, or when present, may occur sporadically or in patches (in the less altered samples white mica is pervasive and had a more homogeneous distribution). In the potassic alteration zones, Mg-rich biotite is usually, but not always present, with compositions between Mg# 70 to Mg# 90. In the most extreme cases, sections within this brown-beige altered core can be silica flooded, resulting in the absence of detectable biotite (or white mica).

Typical spectra taken from these samples (Figure 3-5e) reiterate that with increasing alteration, white mica becomes more phengitic, with the position of the 2200 nm absorption moving to longer wavelengths. Concurrently, biotite becomes increasingly Mg-rich, and the position of the 2250 nm absorption moves to shorter wavelengths. In continuum removed spectra of highly altered samples, both absorptions therefore partially overlap, and may not be fully distinguishable. However, both absorptions remain fully separable in second derivative spectra, as seen in Figure 3-5f.

3.4.2 Correlation between mineral chemistry and Au content

The results presented above indicate that the composition of white mica and biotite reflects the degree of hydrothermal alteration. It may therefore be possible to determine if a sample is mineralized based on the absorption positions of these minerals. This section examines the correlation between hyperspectral data of all available offcuts (216 metasedimentary and 25 intrusive samples), and the Au content of their parent sample. In this case, homogeneous sections of drill core or field samples were selected for geochemical analysis, with obvious veins and veinlets excluded, and thin sections were cut in a portion of the (homogeneous) sample. The spectral imagery showed that 142 of the 216 metasedimentary samples had white mica (66% of samples) and 182 had biotite and/or chlorite (84% of samples). For the later, biotite and chlorite predominance was determined using the rule-based method, where 82 samples were determined to be biotite-rich. Of the 216 metasedimentary samples, 34 (16%) had biotite/chlorite abundances too low for proper identification (i.e., the samples are predominantly white mica). Of the 25 intrusive rocks, 21 samples (84%) showed white mica, 15 samples had biotite (63%) and 8 had chlorite (32%).

Correlations between whole-rock Au concentration and absorptions positions are presented in Figure 3-6. A scatter plot of the Au content and the position of the 2200 nm absorption of white mica is presented in Figure 3-6a, and includes data for the metasedimentary (circles) and intrusive rocks (diamonds). For all samples, the Au content increases with the absorption position (towards phengitic white mica). Importantly, all samples with >0.3 g/t Au (the current cut-off grade) have absorptions above 2205 nm (<1.68 Al^{VI} apfu), and all samples with >1 g/t have absorptions above 2207 nm (<1.64 Al^{VI} apfu). Figure 3-6b shows the same plot using absorptions for biotite and chlorite and reveals that the Au content increases with a decrease in the absorptions position (increase in Mg#). All samples above 0.3 g/t Au have absorptions below 2250 nm for biotite (Mg# >65), or 2252 nm for chlorite (Mg# >65), and all samples with >1 g/t Au have absorptions below 2249.5 nm for both biotite (Mg# >70) and chlorite (Mg# >67).

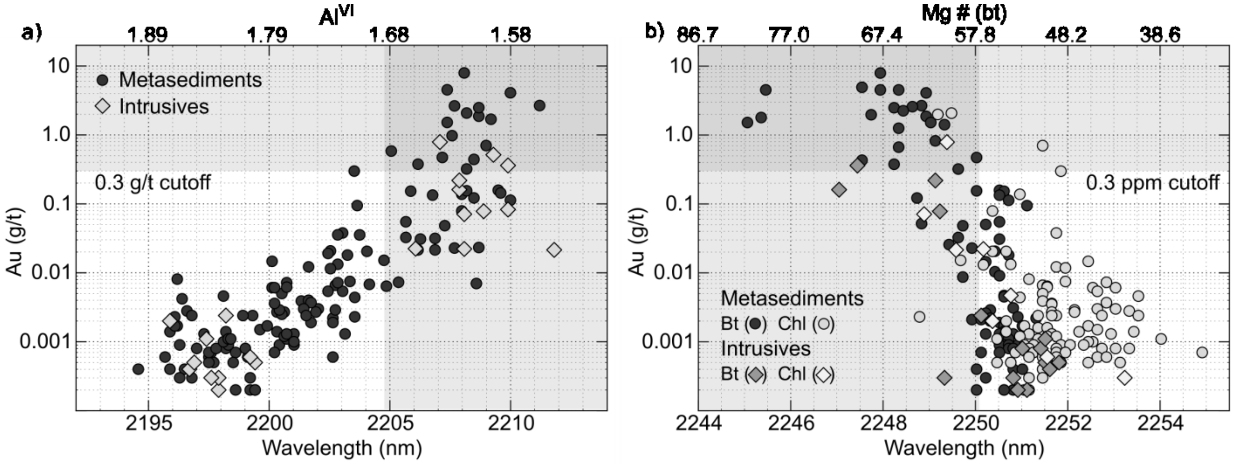

Figure 3-6 *Scatter plot of whole-rock Au concentration and the position of absorption features for a) white mica and b) biotite in Pontiac Group metasedimentary and intrusive rocks.*

As pervasive hydrothermal alteration can locally extend further than strong Au-enrichment (see Figure 3-5b), an exact estimation of Au content is not possible for individual samples (i.e., because of the nugget effect). For example, samples with an absorption feature at 2208 nm for (phengitic) white mica can have Au concentrations ranging from 0.1 to 4.0 g/t. However, because this composition is indicative of strong hydrothermal alteration, all samples at 2208 nm are from within a few meters of significant Au contents. This is illustrated in the next section from the analysis of continuous drill core intervals, where alteration haloes extend from a few meters to tens of meters around mineralized intervals.

3.4.3 Imagery of continuous drill core

Hyperspectral data in both SWIR and LWIR were acquired on drill core intervals at 1 mm/pixel to visualize the extent of the alteration haloes around mineralized zones. Eleven drill holes were analyzed, totaling approximately 2000 m of drill core. Figure 3-7 shows the 100-275 m interval of drill hole CM07-1391, which starts in weakly altered to unaltered Pontiac metasedimentary rocks, traverses the Sladen fault (the main mineralized zone), and terminates in the unaltered quartz monzodiorite footwall (last 3 m of core). Here, the presented downhole ore grades were derived from entire drill core intervals (in up to 1.5 m intervals) that were cut in half and analyzed in bulk (including veins). Processed imagery displays the presence and composition of biotite, ranging from 2251 nm (Mg# 54) to 2247 nm (Mg# 72) and chlorite, ranging from 2253 nm (Mg# 52) to 2247 nm (Mg# 75), for least to most altered intervals, respectively. In other drill holes (presented in Appendix 2B), biotite compositions can reach Mg# 90 in highly altered intervals. White mica shows a wider spread (in nanometers), ranging from 2199 nm (1.80 Al^{VI} apfu) in the least altered zone (top, blue colors) to 2211 nm (1.56 Al^{VI} apfu) in the most altered portion of core (center, red colors). Highly mineralized intervals always show highly phengitic white mica (orange-red, >2205 nm) and Mg-rich biotite (orange, <2249 nm). Rocks surrounding strongly mineralized intervals (>1 g/t Au) display a weak to moderate increase in phengitic component over a few meters to a few tens of meters, which also corresponds to areas of anomalous Au contents (above the background of <0.01 g/t Au, but not considered as mineralized).

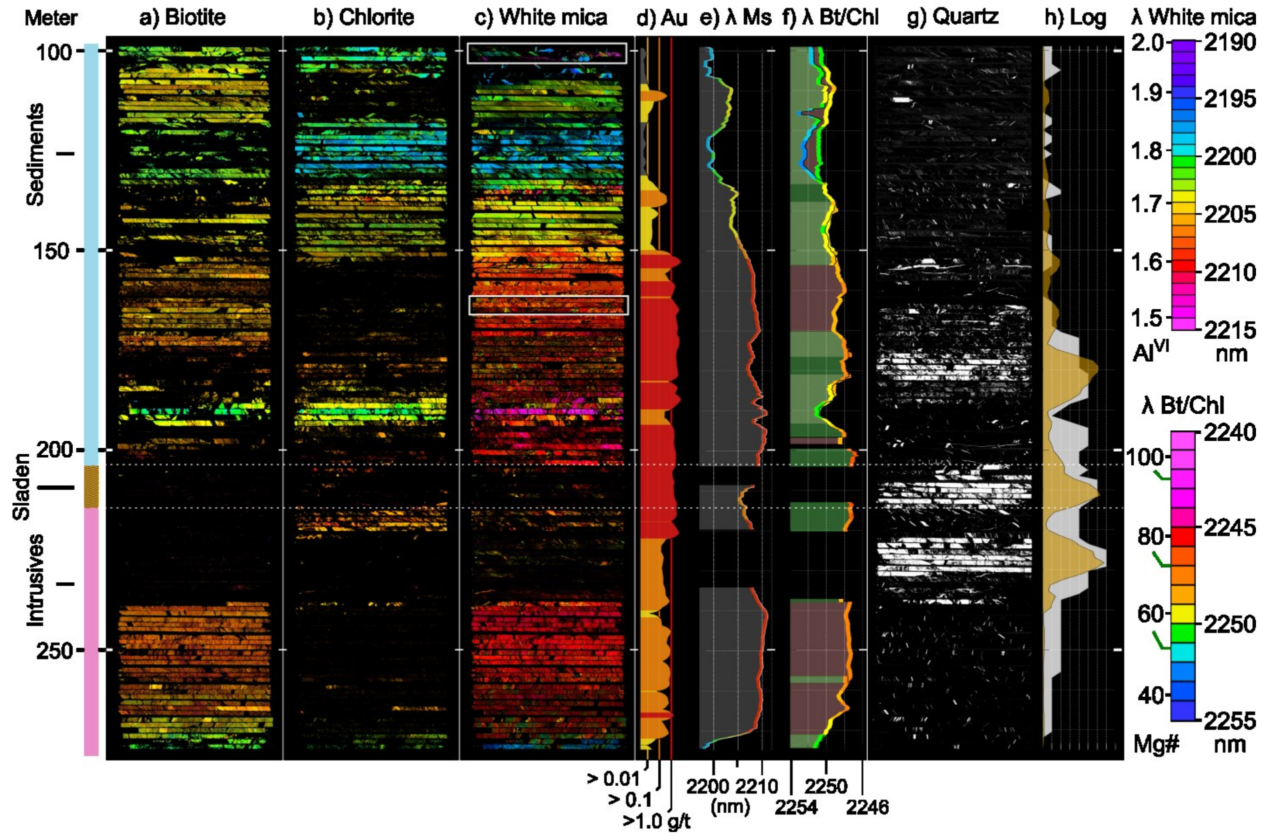

Figure 3-7 *Processed hyperspectral imagery for 175 m of core (from depth interval of 100 to 275 m of drill hole CM07-1391, corresponding to core boxes 25 to 66, lithology indicated at the far left side, same color scheme as in Figure 3-1), with gold grades and logs of silica alteration from the mining company. From left to right, columns a), b) and c) show the positions of the absorptions for biotite, chlorite, and white mica (the two highlighted core boxes in the white mica image are presented in Figure 3-8). For each mineral the color scales relating to absorption positions are on the right. d) Depth profile of the gold grade (in g/t) at a sampling interval of 1.5 m with strongly mineralized zones (>1 g/t Au) highlighted in red, >0.1 g/t in orange, and >0.01 g/t in yellow. Plots e) and f) are depth profiles of the 2200 nm white mica absorption position and the 2250 nm absorption for biotite and chlorite, respectively. g) Processed spectral imagery showing the relative abundance of quartz (from the strength of the 9200 nm peak in reflectance). h) Depth profile of the silicification intensity as determined by the mine geologist (1.5 m interval) in grey and from spectral imagery in yellow. Depth profiles of spectral data (e, f, h) are retrieved from the spectral imagery at a sampling interval of 25 cm (average of 250 lines at 1 mm/pixel with 50 pixels per line), and smoothed using a 3m wide moving average. A graphical summary of lithology, as determined from drill core logs, is plotted on the far left.*

Longwave infrared (LWIR) spectral data are used to estimate silicification intensity. Figure 3-7g shows the relative abundance of quartz, which is estimated from the strength of the ≈9200 nm quartz reflectance peak. The associated downhole profile generally shows a good agreement between the degree of silicification as logged by the mine geologist (grey plot), and the relative strength of the 9200 nm peak (yellow plot). However, because of the relatively low spectral sampling rate of the LWIR-HS instrument (30 bands), further mineralogical characteristics could not be derived for these silicified zones, and no correlation to ore grades is seen in the current dataset.

3.4.4 Textural relationships from hyperspectral imaging

The Canadian Malartic deposit is characterized by disseminated mineralization and pervasive hydrothermal alteration which occurs within and surrounding a network of small *v2* veinlets (de Souza et al., 2015, 2016; Gaillard et al., 2018), and lacks an association with large visible quartz veins. The pervasive nature of the hydrothermal alteration can readily be detected from spectral imagery, where changes in the textural characteristics of white mica occur in association with changes in its composition. Textural characteristics (and petrographic context) observed in spectral imagery can therefore be useful in the identification of alteration. As an example, Figure 3-8 shows imagery from two core boxes of drill hole CM07-1391 (location outlined in Figure 3-7c) including a representative unmineralized and unaltered portion of the Pontiac metasedimentary rocks, and an altered and highly mineralized section of core. The first core box presents an unmineralized section of core, consisting of metasedimentary rocks with metamorphic white mica (2200 nm) that occurs along distinct sedimentary layers (mudstones), in sharp contact to layers devoid of white mica (greywackes). Locally, small veinlets with highly phengitic white mica (≈ 2214 nm) and Mg# ≈50 chlorite (not shown) crosscut all sedimentary layers, and are not related to mineralization. The mineralized section of core (Figure 3-8b), on the other hand, shows pervasive phengitic white mica (≈ 2209 nm) associated with a stockwork of small *v2* veinlets, but does not occur along any particular visible vein, and shows no sharp transitions between sedimentary beds. In this core box, biotite and/or chlorite (not shown) are also present and are always above Mg# 70. Numerous quartz veins and veinlets (mm to cm in sizes) are present in both mineralized and unmineralized sections, and typically contain white mica of muscovitic composition (blue colors, ≈ 2198 nm, 1.82 Al^{VI} apfu), as seen in Figure 3-5a, Figures 3-8a and b (labelled Qz-Ms). In some cases, quartz veins can also be free of white mica (Figure 3-8b, labelled Qz). The presence of veins and veinlets unrelated to mineralization has implications for the sampling strategies best suited for mineral exploration, particularly for bulk-analysis methods that do not provide a clear petrographic context to the data (i.e., point data). At the Canadian Malartic deposit, all visible veins and veinlets were therefore avoided during collection of infrared point data on outcrops.

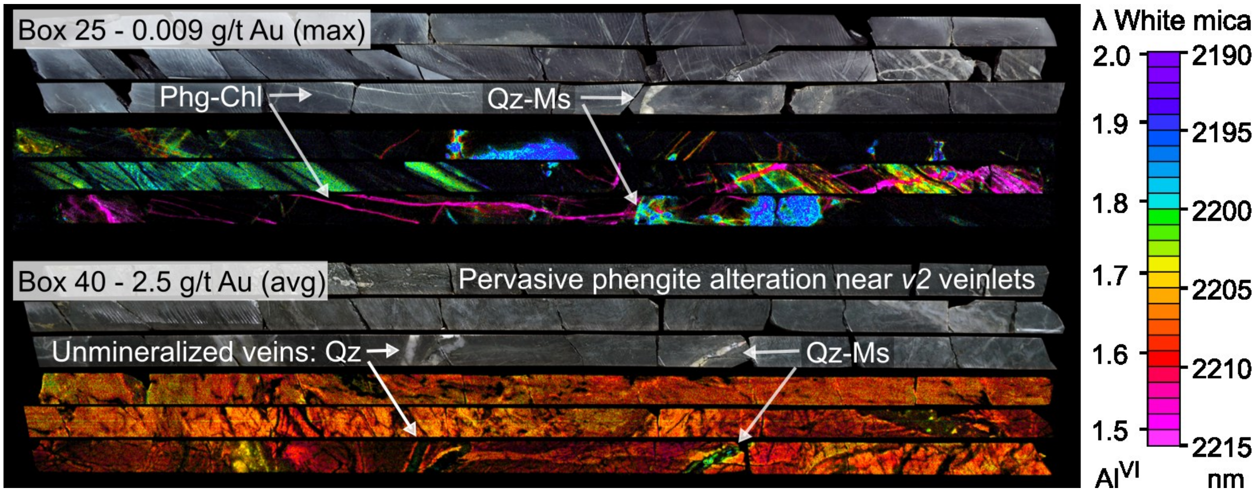

Figure 3-8 *Detail of two core boxes highlighted in Figure 3-7, showing textural and compositional changes in white mica. For each box, a photo of three rows of core (top) is juxtaposed to spectral imagery conveying the position of the white mica absorption (bottom). Top portion: Box 25 (highlighted in Figure 3-7c, top) showing interbedded layers of mudstone (white mica-bearing) and greywacke (white mica-free). The maximum gold grade over this 1.5 m*

interval is 0.009 g/t Au. Lower portion: Box 40 (highlighted in Figure 3-7c, middle) showing typical pervasive phengitic white mica alteration associated to mineralization, with an average gold content of 2.5 g/t Au.

3.4.5 Regional patterns in white mica composition

Gaillard et al. (2018) noted that systematic changes in hydrothermal white mica chemistry could be used as a vector towards mineralization at Canadian Malartic. On regional scales, however, white mica composition is also affected by metamorphism, where higher metamorphic grades stabilize white mica that is progressively more Al-rich (Miyashiro and Shido, 1985; Duke and Lewis, 2010). The regional metamorphic grade in the Pontiac metasedimentary rocks increases southward, with isograds roughly parallel to the CLLDZ. Gaillard et al. (2018) reported white mica compositions (obtained by EMPA) for 47 samples, collected along a single, 4 km long N-S section that included the entirety of the deposit. The metamorphic white mica progressively varies from ≈1.9 Al^{VI} apfu (corresponding to 2195 nm) in the staurolite zone (several km south of the pit) to ≈1.8 Al^{VI} apfu (2200 nm) in the biotite zone (near the pit). On the other hand, hydrothermal white mica was reported to vary from 1.64 to 1.60 Al^{VI} apfu (2207 to 2209 nm).

This study expands on these findings by mapping the full extent of the alteration footprint. For this purpose, over 1500 SWIR data points were acquired in a 50 km by 15 km region surrounding the deposit. Because the regional metamorphic grade decreases towards the open pit, metamorphic white mica becomes more phengitic towards the deposit and may partially masks the effect of (phengitic) hydrothermal alteration. To determine the lowest-grade metamorphic white mica compositions (the most phengitic) near the deposit, data points were acquired in this study with a high sampling density (every outcrop) near the open pit, and are complemented by over 100 data points from tops of historical drill cores within the open pit. Because two distinct processes (metamorphism and hydrothermal alteration) affect white mica composition, regional point data are analyzed in two ways in order to highlight changes related to either process.

The first analysis of these data is shown in Figure 3-9a and was aimed at highlighting regional changes in white mica composition likely related to metamorphic grade. For this purpose, data points are plotted with those showing the shortest wavelength (the least phengitic compositions) on top. That is, if two closely spaced data points overlap, only the least phengitic is shown, and represents the least altered (metamorphic) white mica compositions in that area. Figure 3-9a shows that white mica at the lowest metamorphic grades, in the Timiskaming-type conglomerates north of the CLLDZ, has absorption wavelengths between 2204-2208 nm (yellow-red, ≈1.74-1.64 Al^{VI} apfu). In the northernmost Pontiac metasedimentary rocks, immediately south of the CLLDZ (and within the open pit), the most phengitic micas of metamorphic origin has wavelengths shorter than 2203 nm (yellow-green, ≈1.72 Al^{VI} apfu). Southwards, and with increasing metamorphic grade, white mica is progressively more muscovitic (Al-rich), and has absorption positions that progressively decrease to 2195 nm (purple, ≈1.88 Al^{VI} apfu), which matches the compositions reported by Gaillard et al. (2018). Three regional transects (each 10-15 km long) roughly perpendicular to the metamorphic isograds were sampled 20-30 km away from the deposits, and show similar changes in white mica mineral chemistry, confirming the regional nature of the compositional changes attributed to the regional increase in metamorphic grade.

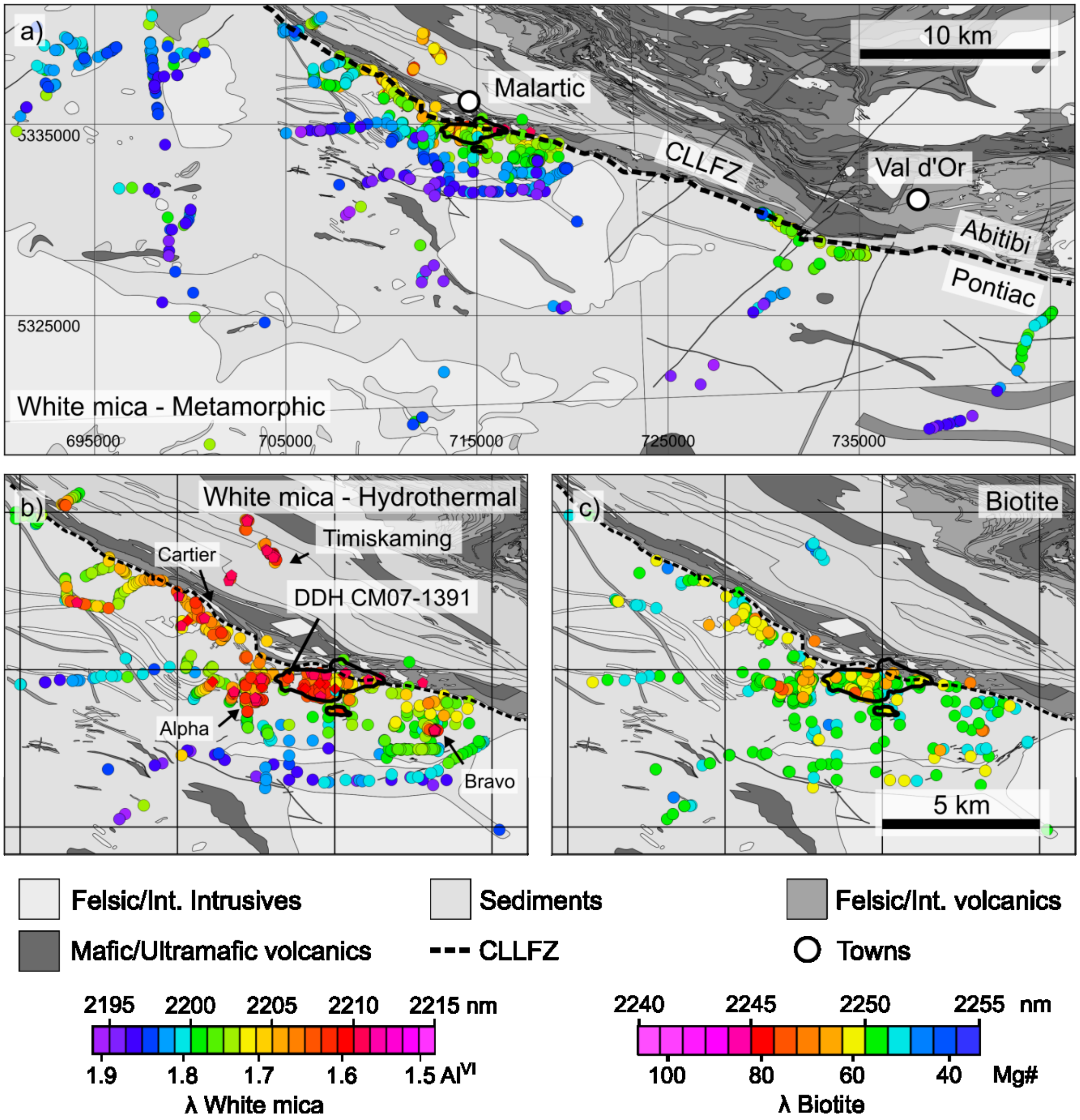

Figure 3-9 *Regional geological map showing spectrally estimated mineral chemistry around Canadian Malartic. Note that at the map scale shown, multiple data points may overlap. a) Regional white mica composition map highlighting changes attributed to increasing metamorphic grade. Data points are plotted with the shortest wavelength shown on top to highlight effect of metamorphism (i.e., for overlapping data points, only the least altered point, with lowest wavelengths are visible). b) Same dataset as in a), but the data points are plotted with the highest wavelength on top in order to highlight the effect of hydrothermal alteration. Note that low wavelength (blue-green) data points represent metamorphic white mica, while hydrothermal white mica is at or above 2205 nm, as established in Figure 3-6a. c) Biotite*

composition map, with data points with the lowest wavelengths plotted on top, to highlight the effects of hydrothermal alteration.

The second analysis of the data is shown in Figure 3-9b, and was aimed at highlighting the hydrothermal alteration halo around Canadian Malartic. For this purpose, the data points at the highest wavelengths (most phengitic micas) are plotted on top. Within and in the vicinity of the open pit, highly altered white mica have wavelengths between 2206 and 2212 nm (orange-red, 1.66-1.55 Al^{VI} apfu), and white mica with elevated phengitic components (down to 2206 nm, orange) can be detected up to 6 km west of the deposit, adjacent to the CLLDZ, past the *Cartier* zone. Weakly altered white micas showing absorptions down to 2203 nm (yellow, 1.72 Al^{VI} apfu), can be detected up to 9 km west of the deposit, but partly overlap with metamorphic compositions. Importantly, all known gold occurrences in the district (*Alpha*, *Bravo* and *Cartier* zones) display the same alteration pattern as Canadian Malartic, having at least a few data points at highly phengitic compositions (>2210 nm). The total size of the detectable alteration footprint, encompassing all known occurrences, approximately spans 12 km along the CLLDZ, and 3 km across strike.

Compositional changes in biotite Mg# associated with hydrothermal alteration occur on a more limited spatial scale than for white mica, and do not define a significant footprint on regional scales. Figure 3-9c shows a regional map of biotite composition, plotted with the lowest wavelengths (highest Mg#) on top, to highlight hydrothermal alteration. Here, only some of the data points within and near the open pit show distinctly Mg-rich biotite, below 2250 nm (yellow, Mg# >65). Background biotite compositions are stable near Mg# 55-60 (≈ 2251 nm) throughout the entirety of the Pontiac metasedimentary rocks, with no systematic changes seen with increasing metamorphic grade to the south. In the lower grade Timiskaming-type conglomerates, however, biotite is Mg-poor, with absorption wavelengths of 2252-2253 nm (Mg# 48-44).

3.5 Discussion

3.5.1 Estimating mineral chemistry in Canadian Malartic samples

Characterizing mineral chemistry is a critical component of economic geology studies, as geochemical parameters can provide information on ore-forming processes, and alteration footprints may be identified. At Canadian Malartic, the Mg# of biotite and the Al^{VI} content of white mica vary with hydrothermal alteration intensity, and were previously identified as potential vectors to mineralization (Gaillard et al., 2018). However, because conventional methods of obtaining mineral chemistry are sample-based, generally expensive and time consuming (e.g. EMPA), datasets are typically limited in size (e.g. a few hundred samples at best). These data therefore only serve to define broad trends in alteration patterns, and provide limited information on the true scale of mineralogical variability within and surrounding a given deposit. In a commercial exploration setting, even if vectors in mineral chemistry are known for a given deposit, few companies make use of EMPA data due to the time and expense required.

This study showed that SWIR data can be used to accurately obtain mineral chemistry (Figure 3-4), and data can be acquired in a matter of seconds. Because no significant changes were seen between spectra of weathered surfaces and equivalent fresh rock (Figure 3-5a), SWIR data can be acquired directly on outcrop surfaces (after removing the lichen cover) or on fresh rocks (e.g., drill core). In all cases, Al^{VI} content of white mica can be estimated from the 2200 nm absorption to ±0.022 Al^{VI} apfu (Figure 3-4b), and importantly, this absorption is not affected by mineral assemblages present in Pontiac metasedimentary rocks. For biotite, the 2250 nm absorption can be used to estimate Mg# to ±1.7 Mg# in biotite-rich samples (Figure 3-4c). In practice, however, because of interference from chlorite, and because the rule-based method described in section 3.3.4 only identifies a given pixel as being biotite-rich or chlorite-rich, some ambiguity remains for intermediate mixtures. In a worst-case scenario, where a chlorite spectrum would be erroneously identified as biotite, the position of the 2250 nm absorption could be shifted by 2 nm to longer wavelengths, towards the chlorite line (Figure 3-4c), and would cause an underestimation of biotite composition by 10 Mg#. In such cases, the use of the 2380 nm absorption could yield better estimates, as it is not prone to interference from chlorite (Lypaczewski and Rivard 2018). Other absorptions present for either white mica or biotite, on the other hand, cannot be used to quantitatively estimate mineral chemistry. The 1400 nm absorption displays an overlap for white mica, biotite and chlorite, and the 2330 nm absorption further overlaps with that of carbonates.

3.5.2 Mineralogical variability in unaltered samples

Few analytical methods allow the investigation of mineral chemistry on scales much larger than a thin section, and in most cases, data can only be obtained in point form (e.g. EMPA). These punctual datasets provide limited information on the small-scale variability present within a sample, leaving uncertainties on the extent of mineralogical variability related to protolith composition, metamorphism, or hydrothermal alteration. The Pontiac Group metasedimentary rocks investigated here consists of interlayered mudstones and greywackes, with beds ranging in size from a few millimeters to several meters. It was noted that metamorphic mineralogy varies with protolith composition, with metamorphic white mica occurring preferentially in the Al-rich mudstones, whereas biotite (± chl) occurs in all metasedimentary rocks (Gaillard et al., 2018; Piette-Lauzière et al., *2019*). Hyperspectral imagery of several hundred samples, revealed that, on average, 60 to 70% of the unaltered Pontiac metasedimentary rocks are white mica-bearing (≈ mudstones), with the remainder being white mica-free (≈ greywackes), usually with sharp transitions between both rock types (e.g. Figure 3-5a). Most white mica-bearing beds had chlorite, whereas most white mica-free beds were preferentially biotite-rich, but mixtures of biotite and chlorite commonly occur. It was also revealed that, while the protolith composition affects mineralogy, no changes in mineral chemistry are observed between alternating rock types on sample-scales (up to a few meters). All layers within a given sample showed absorption positions within ± 1 nm throughout (part of this variability is likely attributable to noise in single pixel spectra). In unaltered metasedimentary rocks, changes in white mica mineral chemistry are caused by changes in metamorphic grade, which occur in the Pontiac metasedimentary rocks on regional scales. Here, metamorphic white mica compositions in the Pontiac metasedimentary rocks gradually vary from 1.9 Al^{VI} apfu (2195 nm) in the highest grades (amphibolite facies), several kilometers south of the deposit, to approximately 1.75 Al^{VI} apfu (2203 nm) in the northernmost and lowest grade Pontiac metasedimentary rocks (upper greenschist facies) which occur near and within the open pit. Changes in white mica composition attributable to metamorphism are therefore at most 1 nm (0.02 Al^{VI} apfu) per 200 m (Figure 3-9a), in a direction perpendicular to metamorphic isograds. On a sample scale, variability in white mica composition larger than ± 1 nm is therefore likely to be related to hydrothermal alteration. Further north, across the CLLDZ, the Timiskaming-type metasedimentary rocks sit at a lower, mid-greenschist facies metamorphic grade. Based on a few data points, metamorphic white mica is slightly more phengitic than in the Pontiac Group, and can reach 1.6 Al^{VI} (2208 nm).

In the Pontiac metasedimentary rocks, biotite composition (Mg#) does not vary on a sample scale (i.e., from protolith composition), but, unlike in white mica, it is unaffected by metamorphic grade, and remains stable at around Mg# 55-60 (Figure 3-9c). Because the Mg# of biotite is consistent on regional scales, any significant variability in absorption position on a sample scale is likely to be related to hydrothermal alteration, although in some cases, minor, gradual changes in biotite absorption positions (up to 2 nm) observed within or between beds may be caused by the presence of small amounts of interfering chlorite, as discussed in the previous section. The Timiskaming-type metasedimentary rocks similarly show consistent biotite compositions, but generally at a lower Mg# of 50.

3.5.3 Hydrothermal alteration zonations at Canadian Malartic

The hydrothermal alteration at Canadian Malartic progresses from a proximal potassic alteration zone, characterized by a beige-brown color and spectrally active phlogopite or Mg-rich biotite (Mg# 90-70), and grades into a distal potassic-sericitic alteration zone presenting a pale blueish-grey color and spectrally active Mg-rich biotite (Mg# >60) and phengitic white mica. A mylonitized or brecciated zone (corresponding to the Sladen fault) may be present at the core of the potassic alteration zone, and can locally be highly silicified, resulting in the presence of few spectrally active minerals. These zones commonly show considerable overlap, and can occur concurrently on sample scales (within tens of centimeters) around mineralized *v2* veinlets (see Gaillard et al., 2018, Figures 6 and 7). However, not all alteration zones are necessarily present within a given drill core interval, with sericitization generally being better developed in Al-rich mudstone protoliths (Gaillard et al., 2018). Additionally, all zones have the potential to be affected by retrograde chloritization, further complicating their identification (Helt et al., 2014; de Souza et al., 2015, 2016; Gaillard et al., 2018). Based on the hyperspectral imagery presented here, these alteration zones can be better described by gradual change in white mica and biotite chemistry, estimated from the 2200 and 2250 nm absorptions, respectively.

In the example drill hole shown here (CM07-1391, Figure 3-7), a central brecciated zone (the Sladen fault) is silica flooded and shows few to no spectrally active minerals in the SWIR, but quartz, the predominant mineral, can be detected in the LWIR. Other drill holes (e.g., CM08-1578, Figure 11 in Gaillard et al., 2018) show a central brecciated zone predominantly consisting of microcline-albite and SWIR-active phlogopite (Mg# > 90), with relatively little quartz (detected in LWIR). The phlogopite is generally Al-poor ($Al^{VI} < 0.2$ apfu), which is reflected in a weak or non-existent 2250 nm Al(Mg,Fe)-OH absorption. In such cases, the 2380 nm $(Mg,Fe)_3$-OH absorption is better suited at estimating biotite composition, as this absorption is not affected by Al^{VI} content (see Lypaczewski and Rivard 2018 for the effects of Al^{VI} on biotite spectra). In these most intensely altered intervals, white mica is generally absent. Outwards, in the typical proximal alteration zone (i.e., beige-brown potassic alteration zone, Figure 3-5d), the Al^{VI} content of biotite increases to above 0.2 Al^{VI} apfu, and Mg# can reliably be estimated from the 2250 nm absorption. Within this alteration zone, the Mg# of biotite decreases from Mg# 90 (2243 nm) near or within the brecciated zone to Mg# 65 (2248 nm) in the outer fringes of the proximal alteration zone, generally within tens of meters. White mica may appear in the proximal alteration zone when biotite composition reaches Mg# 75 (2246 nm), initially as highly phengitic white mica (1.5 Al^{VI} apfu, 2212 nm). Further outwards on scales of tens to hundreds meters, as alteration intensity decreases, white mica progressively loses its phengitic component, reaching 1.62 Al^{VI} apfu (2208 nm) in the distal alteration zone (the blueish-grey potassic-sericitic zone, Figure 3-5c). Concurrently, biotite reaches Mg# 60 (≈2250 nm) and becomes indistinguishable from background metamorphic compositions. With increasing distance outwards, white mica composition progressively reaches metamorphic background values (≈ 2203 nm near the open pit).

As presented in Figure 3-6, mineralization intensity (g/t Au) is broadly correlated to alteration intensity, with high-grade ore (> 1 g/t Au) occurring exclusively in samples with white mica > 2208 nm (< 1.6 Al^{VI}) and biotite < 2249 nm (> Mg# 65), and the low-grade ore-shell (> 0.3 g/t Au) occurring only in samples with white mica > 2205 nm (< 1.68 Al^{VI}) and biotite < 2250 nm (Mg# > 60). These correlations have potential application for the mining industry, both in an exploration setting, as vectors to mineralization, and in a production environment, as simple metrics for ore-sorting.

3.5.4 Implications for the mining industry

The bulk of the mineralization at Canadian Malartic occurs within or in the immediate vicinity of structurally-controlled fluid pathways (*v2* veinlet stockworks), but hydrothermal fluids percolated through and altered the host rocks on scales of meters to tens of meters away from these pathways (Figure 3-7). As shown in Figure 3-9b, however, altered zones are detectable on a regional scale around Canadian Malartic, up to several kilometers outside the current open pit. These distant alteration zones occur along lithological contacts to more competent units, for example along intrusive dykes (e.g., Alpha zone, Figure 3-9b), or along the CLLDZ (e.g., Cartier zone, Figure 3-9b), which acted as fluid pathways. As the phengitic white mica characterizing these alteration zones can easily be detected using SWIR reflectance spectroscopy, this method can be used as a rapid exploration tool in the Abitibi Subprovince. Focusing exploration along lithological contacts, particularly along the prospective CLLDZ, which has a strike length of over 200 kilometers, may allow mineralized areas to be detected at greater distances than using conventional exploration methods. This study was mainly focused on the Pontiac metasedimentary rocks, but data were also collected in a small number of felsic to intermediate dykes or plutons (i.e., the competent units). These units follow the same alteration patterns as in the metasedimentary rocks (Figure 3-6), therefore white mica compositions from either the sedimentary or the intrusive units can be similarly utilized as a potential vector to mineralization.

However, several caveats need to be considered if SWIR results are to be interpreted correctly. For example, in the Abitibi Subprovince, white mica compositions can be affected by both the metamorphic grade and by hydrothermal alteration. At high metamorphic grades, such as in the amphibolite facies found in the southern Pontiac metasedimentary rocks, metamorphic white mica is Al-rich and is distinct from Al-poor (phengitic) hydrothermal white mica. At low metamorphic grades, however, such as in the mid-greenschist facies in the Timiskaming-type sediments (Figure 3-9b), metamorphic white mica is Al-poor. In samples that have an uncertain protolith (e.g., boulders), this white mica composition may erroneously be interpreted to be of hydrothermal origin. In such cases, biotite chemistry may serve as a way to discriminate between hydrothermal and metamorphic phengite. In the Timiskaming-type sediments, metamorphic phengite is associated to Mg# 50 biotite (> 2252 nm), whereas the hydrothermal phengite at Canadian Malartic is associated to Mg# > 65 biotite (< 2248 nm). Another potential issue is the occurrence of numerous late veinlets presenting highly phengitic white mica unrelated to mineralization (Figure 3-8a, 2215 nm, 1.5 Al^{VI}). If spectral imagery is available, these veinlets can relatively easily be distinguished by their textural context. Alternatively, in point data, they can be detected by the composition of the associated chlorite, which is always low-Mg# (absorption at ≈ 2253 nm, Mg# 50), inconsistent with hydrothermal alteration. In other deposits, opposite alteration patterns may also occur. For example, Wang et al. (2017) reported that, in the

Eastern Goldfields of Western Australia, the Archean Sunrise Dam gold deposit presented low wavelength (Al-rich) white mica in mineralized intervals, whereas the Kanowna Belle gold deposit, in the same region, presented ore zones with high wavelength (Al-poor) phengitic white mica, similarly as to what is seen at Canadian Malartic.

With these limitations in mind, and if the deposit geology is well understood, it would be possible to use hyperspectral imaging in a production environment. A hyperspectral camera installed directly atop a conveyor belt transporting bulk-ore, for example, could be an effective ore sorting method. At Canadian Malartic, any rock sample that would present Al-rich white mica (e.g., > 1.68 Al^{VI}, < 2205 nm, Figure 3-6a) would be unaltered, and therefore cannot be mineralized. Any such fragments could safely be discarded as waste. On the other hand, a sample that would present phengitic white mica (> 2205 nm) and/or Mg-rich biotite (< 2250 nm) could be hydrothermally altered, and could potentially (but not necessarily) be mineralized. Samples with these compositions could have Au contents ranging from ≈ 0.01 to > 1.0 g/t Au, but it would not be possible to determine the exact Au content with this metric. Other spectrally derived metrics may have applications at later stages of ore processing. For example, LWIR data can be used to accurately estimate the intensity of silicification (quartz), which has direct repercussion on milling operations. Alternatively, these same datasets can be acquired at earlier stages of the exploration process, for example during the initial core logging and geological modelling stages. This would allow to more efficiently determine lithology, and to more accurately delineate potential ore zones, potentially reducing assaying costs.

3.6 Conclusions

Reflectance spectroscopy is shown to be an effective method to characterize mineralogy and mineral chemistry, including in samples containing complex mineral mixtures. The Mg# of biotite can be estimated from the 2250 nm absorption to ± 1.7 Mg# for relatively chlorite-free samples, and the Al^{VI} content of white mica can be estimated from the 2200 nm absorption to ± 0.022 Al^{VI} in all samples, as no spectrally interfering minerals are present. At the Canadian Malartic gold deposit, mineral chemistry varies with hydrothermal alteration intensity, with increasingly Al-poor (phengitic) white mica and increasingly Mg-rich biotite occurring towards mineralized centers. As ore grades are broadly correlated to alteration intensity, and therefore to mineral chemistry, barren and ore-bearing samples can be distinguished on the basis of their spectral response. In drill core, changes in biotite mineral chemistry (Mg#) are restricted to, and can be used to delineate mineralized intervals, whereas changes in white mica chemistry (Al^{VI} content) extend meters to tens of meters beyond mineralized intervals, and can serve as vectors to mineralization. Regionally, white mica alteration can be detected in a 12 km by 3 km halo surrounding the deposit, extending to large distances preferentially along lithological contacts to more competent units. As acquiring SWIR data requires no samples preparation and can be done directly on outcrops, SWIR spectroscopy has the potential to be used as a rapid regional exploration tool in the Abitibi, or in similar greenstone belt environments.

References

Arne, D., House, E., Pontual, S. and Huntington, J., 2016. Hyperspectral interpretation of selected drill cores from orogenic gold deposits in central Victoria, Australia. Australian Journal of Earth Sciences, 63(8), pp.1003-1025.

ASD Inc. (2010) FieldSpec® 3 User Manual, Boulder, CO, USA. ASD Inc.

Ayer, J.A., et al., 2005. Overview of results from the greenstone architecture project: discover Abitibi initiative. Ontario Geol. Surv. Open File Rep. 6154, 146.

Bérubé, C.L., Olivo, G.R., Chouteau, M., Perrouty, S., Shamsipour, P., Enkin, R.J., Morris, W.A., Feltrin, L. and Thiémonge, R., 2018. Predicting rock type and detecting hydrothermal alteration using machine learning and petrophysical properties of the Canadian Malartic ore and host rocks, Pontiac Subprovince, Québec, Canada. Ore Geology Reviews, 96, pp.130-145.

Besson, G., and Drits, V. A. 1997. Refined relationships between chemical composition of dioctahedral fine-grained micaceous minerals and their infrared spectra within the OH stretching region. Part II: The main factors affecting OH vibrations and quantitative analysis. Clays and Clay Minerals, 45(2), 170-183.

Bishop, J.L., Lane, M.D., Dyar, M.D. and Brown, A.J., 2008. Reflectance and emission spectroscopy study of four groups of phyllosilicates: smectites, kaolinite-serpentines, chlorites and micas. Clay minerals, 43(1), pp.35-54.

Chang, Z. and Yang, Z., 2012. Evaluation of inter-instrument variations among short wavelength infrared (SWIR) devices. Economic Geology, 107(7), pp.1479-1488.

Clark, R.N., King, T.V., Klejwa, M., Swayze, G.A. and Vergo, N., 1990. High spectral resolution reflectance spectroscopy of minerals. Journal of Geophysical Research: Solid Earth, 95(B8), pp.12653-12680.

Corfu, F., Jackson, S.L., Sutcliffe, R.H., 1991. U-Pb ages and tectonic significance of late Archean alkalic magmatism and nonmarine sedimentation: timiskaming Group, southern Abitibi belt, Ontario. Can. J. Earth Sci. 28 (4), 489–503.

Dalm, M., Buxton, M.W.N. and van Ruitenbeek, F.J.A., 2017. Discriminating ore and waste in a porphyry copper deposit using short-wavelength infrared (SWIR) hyperspectral imagery. Minerals engineering, 105, pp.10-18.

Davis, D.W., 2002. U–Pb geochronology of Archean metasedimentary rocks in the Pontiac and Abitibi subprovinces, Quebec, constraints on timing, provenance and regional tectonics. Precambrian Research, 115(1-4), pp.97-117.

De Souza, S., Dubé, B., McNicoll, V.J., Dupuis, C., Mercier-Langevin, P., Creaser, R.A., Kjarsgaard, I.M., 2015. Geology, hydrothermal alteration, and genesis of the worldclass Canadian Malartic stockwork-disseminated Archean gold deposit, Abitibi, Quebec. In: Dube, B., Mercier-Langevin, P. (Eds.), Targeted Geoscience Initiative 4: Contributions to the Understanding of Precambrian Lode Gold Deposits and Implications for Exploration. Geological Survey of Canada, pp. 113–126 Open File 7852.

De Souza, S., Dubé, B., McNicoll, V.J., Dupuis, C., Mercier-Langevin, P., Creaser, R.A., Kjarsgaard, I.M., 2016. Geology and hydrothermal alteration of the world-class Canadian Malartic gold deposit: genesis of an Archean stockwork-disseminated gold deposit in the Abitibi Greenstone Belt, Québec. Reviews in Economic Geology, 19, 29 p.

Duke, E.F., 1994. Near infrared spectra of muscovite, Tschermak substitution, and metamorphic reaction progress: Implications for remote sensing. Geology, 22(7), pp.621-624.

Duke, E.F. and Lewis, R.S., 2010. Near infrared spectra of white mica in the Belt Supergroup and implications for metamorphism. American Mineralogist, 95(7), pp.908-920.

Gaillard, N., Williams-Jones, A.E., Clark, J.R., Lypaczewski, P., Salvi, S., Perrouty, S., Piette-Lauzière, N., Guilmette, C. and Linnen, R.L., 2018. Mica composition as a vector to gold mineralization: Deciphering hydrothermal and metamorphic effects in the Malartic district, Quebec. Ore Geology Reviews, 95, pp.789-820.

Graham, G.E., Kokaly, R.F., Kelley, K.D., Hoefen, T.M., Johnson, M.R. and Hubbard, B.E., 2018. Application of imaging spectroscopy for mineral exploration in Alaska: A study over porphyry Cu deposits in the Eastern Alaska Range. Economic Geology, 113(2), pp.489-510.

Harraden, C.L., McNulty, B.A., Gregory, M.J., Lang, J.R., 2013. Shortwave infrared spectral analysis of hydrothermal alteration associated with the pebble porphyry Copper-Gold-Molybdenum Deposit Iliamna, Alaska. Econ. Geol. 108 (3), pp. 483–494.

Heiligmann, M., Williams-Jones, A.E. and Clark, J.R., 2008. The role of sulfate-sulfide-oxide-silicate equilibria in the metamorphism of hydrothermal alteration at the Hemlo gold deposit, Ontario. Economic Geology, 103(2), pp.335-351.

Helt, K.M., Williams-Jones, A.E., Clark, J.R., Wing, B.A. and Wares, R.P., 2014. Constraints on the genesis of the Archean oxidized, intrusion-related Canadian Malartic gold deposit, Quebec, Canada. Economic Geology, 109(3), pp.713-735.

Hunt, G.R., Salisbury, J.W., 1970. Visible and near-infrared spectra of minerals and rocks: I Silicate minerals. Modern Geology, 1, pp. 283-300

Hunt, G.R., 1977. Spectral signatures of particulate minerals in the visible and near infrared. Geophysics 42 (3), 501–513.

Jones E, Oliphant E, Peterson P, et al. SciPy: Open Source Scientific Tools for Python, 2001-, http://www.scipy.org/ [Online; accessed 2019-04-04]

Jones, S., Herrmann, W. and Gemmell, J.B., 2005. Short wavelength infrared spectral characteristics of the HW horizon: Implications for exploration in the Myra Falls volcanic-hosted massive sulfide camp, Vancouver Island, British Columbia, Canada. Economic Geology, 100(2), pp.273-294.

Laakso, K., Peter, J.M., Rivard, B. and White, H.P., 2016. Short-wave infrared spectral and geochemical characteristics of hydrothermal alteration at the Archean Izok Lake Zn-Cu-Pb-Ag volcanogenic massive sulfide deposit, Nunavut, Canada: Application in exploration target vectoring. Economic Geology, 111(5), pp.1223-1239.

Laukamp, C., Cudahy, T., Thomas, M., Jones, M., Cleverley, J.S. and Oliver, N.H.S., 2011. Hydrothermal mineral alteration patterns in the Mount Isa Inlier revealed by airborne hyperspectral data. Australian Journal of Earth Sciences, 58(8), pp.917-936.

Lypaczewski, P. and Rivard, B., 2018. Estimating the Mg# and AlVI content of biotite and chlorite from shortwave infrared reflectance spectroscopy: Predictive equations and recommendations for their use. International journal of applied earth observation and geoinformation, 68, pp.116-126.

Martínez-Alonso, S., Rustad, J. R., and Goetz, A. F. 2002. Ab initio quantum mechanical modeling of infrared vibrational frequencies of the OH group in dioctahedral phyllosilicates. Part II: Main physical factors governing the OH vibrations. American Mineralogist, 87(8-9), pp. 1224-1234.

Mathieu, M., Roy, R., Launeau, P., Cathelineau, M. and Quirt, D., 2017. Alteration mapping on drill cores using a HySpex SWIR-320m hyperspectral camera: Application to the exploration of an unconformity-related uranium deposit (Saskatchewan, Canada). Journal of Geochemical Exploration, 172, pp.71-88.

Mauger, A.J., Ehrig, K., Kontonikas-Charos, A., Ciobanu, C.L., Cook, N.J. and Kamenetsky, V.S., 2016. Alteration at the Olympic Dam IOCG–U deposit: insights into distal to proximal feldspar and phyllosilicate chemistry from infrared reflectance spectroscopy. Australian Journal of Earth Sciences, 63(8), pp.959-972.

McLeod, R.L., Gabell, A.R., Green, A.A., Gardavski, V., 1987. Chlorite infrared spectral data as proximity indicators of volcanogenic massive sulphide mineralization. Pac. Rim Congr. 87, 321–324.

Miyashiro, A. and Shido, F., 1985. Tschermak substitution in low-and middle-grade pelitic schists. Journal of Petrology, 26(2), pp.449-487.

Oliphant, T.E., 2006. A guide to NumPy (Vol. 1, p. 85). USA: Trelgol Publishing.

Perrouty, S., Gaillard, N., Piette-Lauzière, N., Mir, R., Bardoux, M., Olivo, G.R., Linnen, R.L., Bérubé, C.L., Lypaczewski, P., Guilmette, C. and Feltrin, L., 2017. Structural setting for Canadian Malartic style of gold mineralization in the Pontiac Subprovince, south of the Cadillac Larder Lake Deformation Zone, Québec, Canada. Ore Geology Reviews, 84, pp.185-201.

Perrouty, S., Linnen, R.L., Lesher, C.M., Olivo, G.R., Piercey, S.J., Gaillard, N., Clark, J.R. and Enkin, R.J., 2018. Expanding the size of multi-parameter metasomatic footprints in gold exploration: utilization of mafic dykes in the Canadian Malartic district, Québec, Canada. Mineralium Deposita, pp.1-26.

Piette-Lauzière, N., Guilmette, C., Bouvier, A., Perrouty, S., Pilote, P., Gaillard, N., Lypaczewski, P., Linnen, R.L. and Olivo, G.R., 2019. The timing of prograde metamorphism in the Pontiac Subprovince, Superior craton; implications for Archean geodynamics and gold mineralization. Precambrian Research, 320, pp.111-136.

Post, J.L. and Noble, P.N., 1993. The near-infrared combination band frequencies of dioctahedral smectites, micas, and illites. Clays and clay minerals, 41(6), pp. 639-644.

Powell, W.G., Carmichael, D.M. and Hodgson, C.J., 1995. Conditions and timing of metamorphism in the southern Abitibi greenstone belt, Quebec. Canadian Journal of Earth Sciences, 32(6), pp.787-805.

Roache, T.J., Walshe, J.L., Huntington, J.F., Quigley, M.A., Yang, K., Bil, B.W., Blake, K.L. and Hyvärinen, T., 2011. Epidote–clinozoisite as a hyperspectral tool in exploration for Archean gold. Australian Journal of Earth Sciences, 58(7), pp.813-822.

Robert, F., 1989. Internal structure of the Cadillac tectonic zone southeast of Val d'Or, Abitibi greenstone belt, Quebec. Canadian Journal of Earth Sciences, 26(12), pp.2661-2675.

Sansfaçon, R., Grant, M., and Trudel, P., 1987, Géologie de la mine Canadian Malartic -District de Val d'Or, Série des manuscripts bruts - Direction Générale de l'Exploration Géologique et Minérale, MB87-26.

Schodlok, M.C., Whitbourn, L., Huntington, J., Mason, P., Green, A., Berman, M., Coward, D., Connor, P., Wright, W., Jolivet, M. and Martinez, R., 2016. HyLogger-3, a visible to shortwave and thermal infrared reflectance spectrometer system for drill core logging: functional description. Australian Journal of Earth Sciences, 63(8), pp.929-940.

Sillitoe, R.H., 2010. Porphyry copper systems. Economic geology, 105(1), pp.3-41.

Speta, M., Rivard, B., Feng, J., Lipsett, M. and Gingras, M., 2015. Hyperspectral Imaging for the Determination of Bitumen Content in Athabasca Oil Sands Core Samples. AAPG Bulletin, 99(7), pp.1245-1259.

Swayze, G.A., Clark, R.N., Goetz, A.F., Livo, K.E., Breit, G.N., Kruse, F.A., Sutley, S.J., Snee, L.W., Lowers, H.A., Post, J.L. and Stoffregen, R.E., 2014. Mapping advanced argillic alteration at Cuprite, Nevada, using imaging spectroscopy. Economic Geology, 109(5), pp.1179-1221.

Trudel, P., and Sauvé, P., 1992, Synthèse des caractéristiques géologiques des gisements d'or du district de Malartic, Direction Générale de l'Exploration Géologique et Minérale, MM 89-04.

Turner, D., Groat, L.A., Rivard, B. and Belley, P.M., 2017. Reflectance spectroscopy and hyperspectral imaging of sapphire-bearing marble from the Beluga occurrence, Baffin island, Nunavut. The Canadian Mineralogist, 55(4), pp.787-797.

van Rossum, G., Python tutorial, Technical Report CS-R9526, Centrum voor Wiskunde en Informatica (CWI), Amsterdam, May 1995 van Ruitenbeek, F.J., Cudahy, T.J., van der Meer, F.D. and Hale, M., 2012. Characterization of the hydrothermal systems associated with Archean VMS-mineralization at Panorama, Western Australia, using hyperspectral, geochemical and geothermometric data. Ore geology reviews, 45, pp.33-46.

Wang, R., Cudahy, T., Laukamp, C., Walshe, J.L., Bath, A., Mei, Y., Young, C., Roache, T.J., Jenkins, A., Roberts, M. and Barker, A., 2017. White mica as a hyperspectral tool in exploration for the Sunrise Dam and Kanowna Belle Gold deposits, Western Australia. Economic Geology, 112(5), pp.1153-1176.

Wells, M., Laukamp, C. and Hancock, E., 2016. Reflectance spectroscopic characterisation of mineral alteration footprints associated with sediment-hosted gold mineralisation at Mt Olympus (Ashburton Basin, Western Australia). Australian Journal of Earth Sciences, 63(8), pp.987-1002.

Wilkinson, J.J., Chang, Z., Cooke, D.R., Baker, M.J., Wilkinson, C.C., Inglis, S., Chen, H. and Gemmell, J.B., 2015. The chlorite proximitor: A new tool for detecting porphyry ore deposits. Journal of Geochemical Exploration, 152, pp.10-26.

Wilkinson, L., Cruden, A.R., Krogh, T.E., 1999. Timing and kinematics of Timiskaming deformation within the Larder Lake - Cadillac deformation zone, southwest Abitibi greenstone belt, Ontario, Canada. Can. J. Earth Sci. 36 (4), 627–647.

Chapter 4 - Characterization of mineralogy in the Highland Valley porphyry Cu district using hyperspectral imaging, and potential applications

4.1 Introduction

Numerous mineral deposits are formed by hydrothermal fluids that, in addition to potentially concentrating metallic elements, also produce an extensive alteration halo in the surrounding host rocks. In porphyry Cu deposits, mineral zonations occur in generally well understood, approximately concentric patterns (e.g., Seedorff et al., 2005; Sillitoe, 2010). If correctly identified as such, changes in mineralogy may be used to vector towards mineralized centers. In numerous hydrothermal mineral deposits, however, alteration consists of fine-grained assemblages that are often difficult to identify with the unaided eye. Alteration is also often telescoping, and early minerals may be partially or fully overprinted by later, lower temperature assemblages, complicating geological interpretations. In practice, in a mineral exploration context, the mineralogical patterns expected from genetic models may be difficult to recognize. Consistently identifying alteration mineralogy requires highly skilled geological expertise, the cutting of, and the analysis of petrographic thin sections, and often also necessitates the support of more complex instrumentation, such as electron probe micro-analyzers (EPMA) or X-ray diffractometers (XRD). Samples investigated using these methods, however, are limited in physical size to fit the instruments (i.e., thin section or hand samples at best), and may not encompass the entirety of the mineralogical variability present within a given rock. In addition, while providing quality data, these instruments are generally expensive and time consuming to operate. Because of this, datasets are generally limited in volume (i.e., at most a few hundred samples), which only allows defining broad trends in regional alteration patterns.

Unlike time-consuming conventional analytical techniques, shortwave infrared (SWIR) reflectance spectroscopy is a well-suited method to rapidly identify alteration mineralogy, as no sample preparation is required, and data acquisition times are on the order of a few seconds per sample. In hydrated minerals, cation-OH bonds produce characteristic absorption features in the SWIR wavelength range that can be used to identify mineralogy, and in many cases also allow estimating mineral chemistry (Hunt, 1977; Clark et al., 1990). Additionally, reflectance spectroscopy is not negatively affected by the fine-grained nature of alteration minerals (Hunt and Salisbury, 1970). SWIR data has been used in numerous studies to characterize alteration mineralogy in various geological settings, including several porphyry-Cu deposits. Cudahy et al. (2001), for example, acquired airborne hyperspectral imagery at 3 to 10 meters/pixel over a porphyry-skarn-Cu system near Yerington, Nevada, which revealed large-scale mineralogical and mineral chemistry patterns associated with mineralization. More recently, Harraden et al. (2013) acquired a total of 3900 SWIR point measurements from a total of 150 drill holes at the Pebble Cu-Au-Mo porphyry deposit in Alaska. These point data revealed that Cu mineralization occurs with pyrophyllite and low-wavelength white mica. Agus (2011) and the related Dalm et al. (2017) studies presented high-resolution hyperspectral imagery (0.2 mm/pixel) for 43 samples from a porphyry-Cu system, with the aim of discriminating between ore and waste material. It was reported that white mica crystallinity and the relative abundances of chlorite and tourmaline could be used to that effect. Graham et al. (2018) acquired both airborne (6 meters/pixel) and laboratory-based (0.5 mm/pixel) hyperspectral imagery near porphyry-Cu deposits at Orange Hill and Bond Creek, Alaska, and identified changes in chlorite and white mica chemistry near mineralized areas. Changes in chlorite chemistry, as determined from SWIR point data, were also identified as a potential vector to mineralization at the Batu Hijau Cu-Au porphyry in Neal et al. (2018).

The Highland Valley Copper (HVC) district in British Columbia, Canada, is host to four major porphyry Cu-(Mo) systems that formed at deeper levels than typical porphyry-Cu deposits, and show a relatively restricted alteration halo (Lesage et al. 2016; Byrne et al. 2017, D'Angelo et al. 2017). The HVC deposits are investigated here as part of the Natural Sciences and Engineering Research Council of Canada (NSERC) and Canada Mining Innovation Council (CMIC) Footprints project, which aims to identify large-scale alteration signatures around mineralized systems using a variety of analytical techniques. To this effect, several studies investigated numerous aspects of the deposits, and have recently been, or are soon to be published. D'Angelo (2016) and D'Angelo et al. (2017) investigated the petrogenesis and evolution of the Guichon Creek batholith hosting the HVC deposits, Byrne et al. (2017) and Byrne (2019) investigated the distal mineralogical signature of alteration, Byrne et al. (2019) investigated the geophysical signature of mineralization, and Lesage et al. (2019) investigated the 3D structure of the deposit.

The current study builds on the datasets acquired as part of these investigations, utilizing a common sample suite. Here, hyperspectral imagery is acquired on 755 common Footprints samples obtained by, and for the studies of D’Angelo (2016), Byrne (2019), and Lesage et al. (2019), as well as on several hundred meters of additional continuous drill core obtained specifically for this study. Because rocks in the HVC district present significant mineralogical complexity on centimeter-scales (several photographs, including feldspar staining results, are available in Byrne et al. 2017), hyperspectral imagery is acquired at high-resolution (0.2 - 0.5 mm/pixel) in order to discern changes occurring between veins, veinlets and vein selvages. Data is also acquired at 1 mm/pixel on continuous drill core to determine the full extent of alteration surrounding mineralized intervals. The application of spectral metrics developed for these datasets is then investigated on a variety of scales. Regionally, in an exploration setting, these can serve to vector towards mineralization. On smaller scales, in a production environment, spectrally detectable changes in mineralogy could enhance the accuracy of core logging, and could potentially predict if a sample is mineralized. However, as discussed in this paper, a number of caveats need to be considered for an accurate interpretation of hyperspectral data.

4.2 Background

4.2.1 Regional geology

The Highland Valley porphyry copper district, comprising at least four mineralized centers, is located in southern British Columbia, Canada, 50 km southwest of the town of Kamloops. The district is hosted by the approximately 60 km by 25 km, concentrically zoned Guichon Creek batholith (Figure 4-10) in the southern portion of the Quesnel Terrane, within the Intermontane Belt physiographic province (McMillan, 1976; Casselman et al., 1995; Alva-Jimenez, 2011, Byrne et al. 2013, D'Angelo et al. 2017). The I-type, calc-alkaline Guichon Creek batholith was emplaced into the Nicola Group volcano-sedimentary rocks of the Quesnel Terrane by at least two magmatic pulses (Northcote, 1969; McMillan, 1976; D'Angelo et al., 2017) between ≈ 211 Ma and ≈ 207 Ma (petrographic descriptions and zircon uranium-lead dates referenced below are summarized from D'Angelo et al., 2017, unless otherwise indicated).

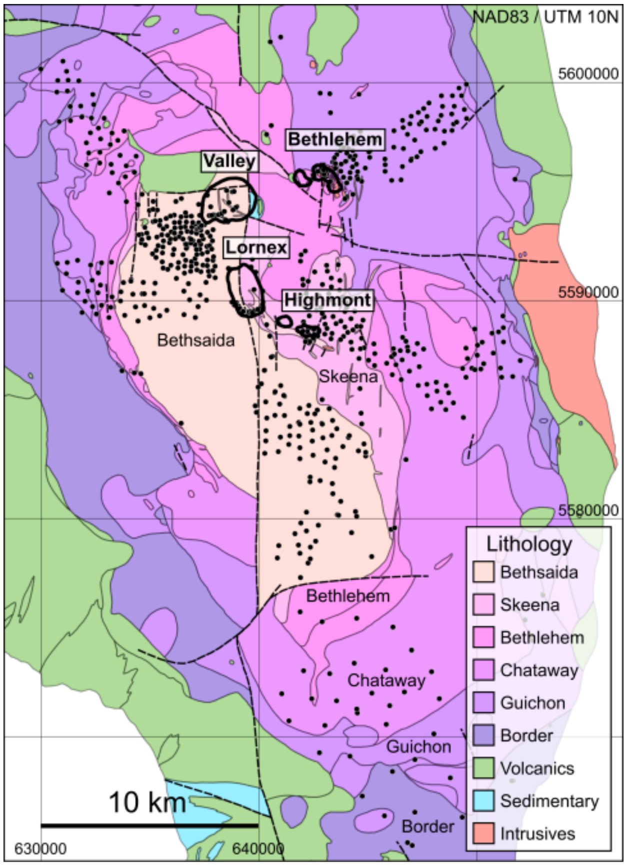

Figure 4-10 *Regional lithological map of the Guichon Creek batholith, with labelled lithofacies. The locations of the major porphyry centers are indicated, and black outlines indicate open pits. The dots represent the locations of 755 rock samples used in this study. Modified after McMillan et al. (2009).*

Continuous magma differentiation resulted in a concentrically zoned batholith comprising five texturally and compositionally distinct facies, ranging from gabbros at the margins to granites near the core, but mostly consisting of granodiorites. From the margins inwards, the equigranular (1) Border and (2) Highland Valley facies (subdivided into the Guichon and the Chataway sub-facies) were emplaced by a first magmatic pulse starting at 211.02 ± 0.17 Ma (Whalen et al. 2017 provide a slightly older date of 215.6 ± 0.5 Ma). A second magmatic pulse was emplaced prior to complete solidification of the Highland Valley facies, as evidenced by gradational contacts (Northcote, 1969; McMillan, 1976). This second pulse started at

209.81 ± 0.27 Ma and formed the porphyritic (3) Bethlehem, and a third pulse was responsible for the (4) Skeena and (5) Bethsaida facies, and associated dikes (D'Angelo et al. 2017; Lee et al., 2017). The youngest Bethsaida facies rocks are dated to 208.55 ± 0.20 Ma. At least six varieties of pre-, syn-, to post-mineralization dikes are recognized throughout the district (Byrne et al. 2013, D'Angelo et al. 2017; Lee et al., 2017). Quartz-feldspar-phyric and quartz-rich porphyry dikes in the Bethsaida facies, interpreted to be syn-to-late-mineralization, are dated to ≈ 206.95 ± 0.22 Ma and represent the last magmatic events to occur in the batholith.

From the generally equigranular rocks formed in the first magmatic pulse, the Border facies rocks are the most heterogeneous, and often contain basaltic xenoliths near the outer margins of the batholith. Border rocks range from gabbros with minor olivine (altered to serpentine, talc and iddingsite) and two pyroxenes (often rimmed by amphiboles) to quartz monzodiorites with amphibole, plagioclase and quartz (D'Angelo et al. 2017). Because of their highly heterogeneous nature (ranging from 44 to 63 wt% SiO_2), the eastern and western sections of the Border facies are excluded from this study, but the less variable southern section (51 to 64 wt% SiO_2, average 58%) is included. The Highland Valley facies comprises the Guichon (≈ 62 wt% SiO_2) and Chataway (≈ 64 wt% SiO_2) sub-facies, consisting of granodiorites to minor quartz monzodiorites. Amphibole and biotite occur in approximately equal proportions and account for up to 25% of the Guichon facies, whereas amphibole is dominant over biotite, which together account for up to 15% the Chataway facies. The second magmatic pulse generated the porphyritic Bethlehem facies granodiorites (≈ 65 wt% SiO_2), with up to 9% mafic minerals, consisting mainly of 2-4 mm sized amphibole phenocrysts and lesser biotite. Felsic phases consist of plagioclase, K-feldspar and fine-grained quartz. The Skeena granodiorites to monzogranites (≈ 67 wt% SiO_2) are intermediate between the Bethlehem and Bethsaida facies

(≈ 69 wt% SiO_2), a porphyritic granodiorite to granite. The Bethsaida contains approximately 50% plagioclase and 30% quartz phenocrysts, and lesser K-feldspar. Mafic phases consist of up to 6% biotite phenocrysts in books up to 5 mm in diameter, and minor amphiboles (Northcote, 1969). Numerous feldspar-(quartz)-(mafic mineral) porphyritic dikes are reported throughout, and are described in detail in Byrne et al., (2013) and D'Angelo et al., (2017).

At least four major porphyry-Cu deposits (Valley, Lornex, Highmont and Bethlehem, Figure 4-10) and over 160 Cu showings are known to occur in the batholith (McMillan et al., 2009; Byrne et al., 2013). The porphyry-Cu centers currently under production or in past-production occur within the more felsic interior and core of the Guichon Creek batholith, and two mineralizing events are recognized (McMillan, 1985; Byrne et al. 2013). The first Cu mineralizing event followed the formation of the Bethlehem facies, and occurred with the emplacement of porphyry dikes and breccias into this facies, forming the Bethlehem deposit. The second and larger Cu-Mo mineralizing event followed the emplacement of the Bethsaida facies and resulted in the formation of the Valley-Lornex and Highmont deposits. The originally contiguous Valley-Lornex deposit was cut by late faulting (the Lornex fault), and the now separate Valley and Lornex deposits are offset by ≈ 3.5 km (Hollister et al., 1976; McMillan, 1976; Byrne et al., 2013). Re-Os ages for molybdenite from the Valley deposit have been reported at 206.7± 1.5 Ma and 205.8 ± 1.5 Ma by Ash et al. (2007), although molybdenite mineralization is interpreted to occur late relative to the main Cu mineralization at Valley (Whalen et al., 2017). Similar Re-Os ages (within error) have been reported by D'Angelo et al. (2017) for the Highmont and Lornex pits (208.3 ± 1.0 Ma, and 208.4 ± 0.9 Ma).

4.2.2 Deposit geology

The Highland Valley district is the largest producing porphyry camp in Canada (Whalen et al. 2017), and has been mined since 1962. Production since 1986 to the end of 2012 is approximately 1,160 million tonnes grading 0.391% copper and 0.009% molybdenum (Graden, 2013). In 2018, Highland Valley Copper produced 100,800 tonnes of copper in concentrate and 8.7 million pounds of molybdenum in concentrate, and has proven and probable reserves of 535 Mt at 0.30 % Cu and 0.007% Mo (Teck Resources Limited, 2019).

The Highland Valley deposits were emplaced by cogenetic plutonic host rocks at relatively deeper levels (4-5 km, D'Angelo 2016, Byrne et al. 2017, D'Angelo et al. 2017) than typical porphyry deposits formed in stocks above parental plutons (generally the upper 4 km of the crust, Sillitoe, 1973; Singer et al. 2008; Sillitoe, 2010). This deeper level of emplacement resulted in a relatively restricted alteration footprint, with alteration selvages limited to a few centimeters around veins or veinlets. Nonetheless, hydrothermal alteration in the Highland Valley district broadly follows the alteration patterns typically recognized in porphyry-Cu deposits, and described in numerous seminal publications (Lowell and Guilbert, 1970; Guilbert and Lowell, 1974; Dilles and Einaudi, 1992; Sillitoe, 2010). The Highland Valley district has been the subject of numerous early (Briskey and Bellamy, 1976; McMillan, 1976; Olade and Fletcher, 1976; Osatenko and Jones, 1976; Olade, 1977) and more recent studies (Alva-Jimenez, 2011; Casselman et al. 1995; Cohen et al. 2011, Byrne et al. 2013; Byrne et al. 2017, D'Angelo et al. 2017, Lesage et al. 2019), where the typical potassic, phyllic, argillic, and propylitic alteration zones have been documented. Mineralization predominantly occurs in veins, fractures, faults, and in the case of the Bethlehem deposit, in breccias. Generally, near the core of the deposits, bornite is the most common sulphide, grading outwards into chalcopyrite and pyrite (Osatenko and Jones, 1976; Alva-Jimenez, 2011; Byrne et al. 2013).

Quartz is most prominent at the Valley and Lornex deposits, where, in the central portion of the deposits, quartz veins with no apparent selvages are Cu barren (Alva-Jimenez, 2011, Byrne et al. 2013). These zones are referred to as a “silicic zone” (McMillan, 1985; Osatenko and Jones, 1976), “silicic re-entrant” (Casselman et al., 1995; Graden, 2013), and more recently as the “barren core” (Byrne et al., 2013). At Valley-Lornex, potassic alteration occurs adjacent to mineralized quartz veins, and is characterized by K-feldspar and by minor secondary biotite (Osatenko and Jones, 1976; Alva-Jimenez, 2011). At Bethlehem, biotite is the principal mineral defining the potassic alteration assemblage near the core of the deposit (biotite is identified mainly in a 400 m wide region near the center or the Jersey open pit, shown on Figure 2.5 of Alva-Jimenez, 2011), but commonly occurs with or is replaced by chlorite (Briskey, 1981; Alva-Jimenez, 2011). Locally, tourmaline cemented breccias occur near the Bethlehem and Highmont deposits. Phyllic alteration, closely associated with mineralization, is most conspicuous at the Valley and Lornex deposits, occurring as coarse grey muscovite selvages around quartz veins, on widths of up to several centimeters. This muscovite-rich alteration is in some cases referenced to as "sericitic" (Osatenko and Jones, 1976) or "early-halo, greisen-like veins" (Byrne et al. 2017). Coarse-grained, greenish phengitic muscovite was also described as forming part of the outer phyllic alteration zone at the Valley (Alva-Jimenez, 2011) and Bethlehem deposits. Pervasive argillic alteration (kaolinite ± montmorillonite) is adjacent to the phyllic zones (Briskey and Bellamy, 1976; Casselman et al., 1995; Byrne et al., 2013), and grades into pervasive propylitic alteration (epidote ± prehnite ± chlorite ± carbonate), which is most apparent in the mafic facies of the batholith, and in the vicinity of the Bethlehem deposit (Casselman et al., 1995; Byrne

2019). From SWIR measurements performed during the course of the NSERC-CMIC "Footprints" project, prehnite has been recognized as an important mineral in the distal propylitic alteration zone in the Guichon Creek batholith (Byrne et al. 2017), and may have previously been identified as "zeolite" in Olade and Fletcher (1976) and Alva-Jimenez (2011). Prehnite occurs either as dark to light mint-green, mm-sized veinlets with extensive disseminated prehnite haloes in more felsic rocks, or as selvages around epidote veins in more mafic rocks. It has been noted that prehnite veinlets (and associated chlorite-white mica alteration) commonly refracture and overprint earlier veins and their alteration haloes, which lead to complex alteration patterns in most samples (Byrne et al., 2017) and complicates their interpretation.

4.3 Methods

4.3.1 Sample suite

In this work, hyperspectral imaging is used to investigate the mineralogical variability across the Guichon Creek batholith and associated Highland Valley deposits. As part of the NSERC-CMIC "Footprints" project, a collection of over 800 common samples were acquired during the works of D'Angelo (2016), Byrne (2019) and Lesage et al. (2019), from which thin sections and whole-rock major and trace element compositions (including Cu grade) are available. A subset of 755 rock slabs from the project sample suite were imaged in order to identify the mineral assemblages related to the distal and proximal alteration at HVC. This imagery also provide insights into small scale (millimeter to centimeter) mineralogical variability often observed between veins, veinlets, and their alteration selvages. Each slab, approximately 10 cm x 10 cm x 1 cm in size, was acquired with a rock saw from outcrops in a 20 km x 40 km region encompassing the deposit, and the slabs span all lithofacies present in the batholith (see Figure 4-10 for sample locations). Near the deposit, samples were acquired at a spacing of approximately 200 m, but sampling density decreased to one per kilometer towards the outer margins of the batholith. Collectively, this sample suite provides insights into regional-scale mineralogical patterns occurring in the Guichon Creek batholith.

A second sample suite, consisting of 400 meters of continuous drill core from the Bethsaida granodiorite, in close proximity to the Valley open pit, was additionally selected for hyperspectral imaging, and intersects both mineralized and unmineralized intervals. This core serves to better define the spatial continuity of hydrothermal alteration on intermediate scales near Cu-mineralized zones (i.e., tens of centimeters to meters), beyond what is observable on a single slab sample. This continuous dataset also correlates mineral assemblages with Cu grade, as assayed by the mining company.

4.3.2 Hyperspectral data acquisition

Hyperspectral imagery was acquired in the SWIR (1000 to 2500 nm) using a Specim SisuROCK hyperspectral scanner (a line-scan imager) at the University of Alberta, Edmonton, Canada. This instrument contains a 256 spectral by 320 spatial pixels mercury-cadmium-telluride (MCT) detector array that acquires data with a 6.3 nm sampling interval, and a 10 nm spectral bandwidth. The instrument was equipped with either an OLES56 (high-resolution) or an OLES15 (low-resolution) lens, which respectively yielded a spatial resolution of 0.2-0.5 mm/pixel or 1 mm/pixel. Dark current and a 99% reflectance Spectralon™ white panel were measured at the beginning of each data acquisition sequence, and radiance data of the geological target were converted to reflectance by subtracting dark current, and then by normalizing to the radiance data of the white panel. Drill cores in 1.2 m long wooden core boxes (four rows per box) were scanned at 1 mm/pixel using the low-resolution lens, and rock slabs were scanned at 0.5 mm/pixel or 0.2mm/pixel using the high-resolution lens. The reported absorption positions (spectral accuracy) of the instrument were calibrated against a National Institute of Standards and Technology (NIST) referenced Mylar standard, as described in Lypaczewski and Rivard (2018). The strongest absorption of the standard is measured at 1660 nm, matching the NIST reference value of 1659.9 nm ±1 nm. Spectral drift (i.e., changes in reported absorption positions over time) was assessed using a reference biotite sample measured with every scanning session, and remained below 1 nm for the entirety of the dataset.

4.3.3 Spectral data analysis

The analysis of spectral data requires the detection of absorption features that are used to uniquely identify mineralogy (Hunt, 1977; Clark et al., 1990). For certain minerals, mineral chemistry or grain size can also be estimated from spectral characteristics, either from the exact position or from the strength of specific absorption features (Clark et al., 1990; Post and Noble, 1993; Lypaczewski and Rivard, 2018). Given the relatively coarse 6.3 nm sampling interval of the imaging spectrometer, spectra need to be interpolated in order to derive precise (and ultimately accurate) absorption positions. Here, spectral data analysis is performed using the method described in Lypaczewski et al. (2019). Spectra are analyzed on a per-pixel basis, and are first linearly interpolated to a sampling rate of 1 nm. Interpolated spectra are then smoothed by convolution with a Gaussian function with a full width half maximum (FWHM) of 25 nm. Absorption feature strength and position are then retrieved by derivative analysis, from the maxima of the second derivative of the convolved spectra. On a sample level (i.e., for an image of a 10 cm by 10 cm slab consisting of 200 x 200 pixels), the average absorption position of all pixels is reported, calculated as the absorption position for each pixel weighed by the absorption strength of the given pixel. To aid in the identification of certain minerals, a spectral slope between two specific wavelengths is also reported, and is calculated on raw data (i.e., non-interpolated, not continuum removed spectra).

4.3.4 Mineral identification

The analysis of spectral data as performed in this study requires a degree of geological and spectroscopic knowledge to correctly identify mineralogy. In a first place, minerals that are likely to occur within the investigated sample suite are identified from ancillary geological knowledge of porphyry copper deposits, as well as from known characteristics of the Highland Valley deposits. Previous studies (summarized in section 4.2.2) have identified the presence of, among others, coarse grained muscovite, kaolinite, tourmaline, chlorite, epidote, smectite and prehnite. Spectral characteristics of these minerals are examined either from existing spectral libraries (e.g., the USGS spectral library, Kokaly et al., 2017) or from samples where the mineral is known to occur, ideally in pure form. Absorptions features unique to these minerals are then identified (if existing), and one or more diagnostic absorptions is selected for each mineral. If no diagnostic absorption exists, a combination of a non-diagnostic absorption and a specific spectral slope in a given spectral region is selected. Hyperspectral data for all samples is then processed by derivative analysis to identify all absorption features occurring in the dataset. Any absorption occurring at positions not identified during the mineral identification step is further investigated, as it could indicate the presence of unidentified minerals. Several additional minerals were identified in this way, including pumpellyite (absorption at 1510 nm) and gypsum (absorption at 1490 nm).

The samples investigated here commonly show the presence of at least 10 spectrally active minerals (i.e., presenting characteristic absorptions features), in addition to spectrally inactive quartz and sulfides (i.e., intrinsically presenting a flat spectral response). For each mineral, a typical spectrum derived from the current sample suite is presented in Figure 4-11, and spectral parameters used for identification are indicated.

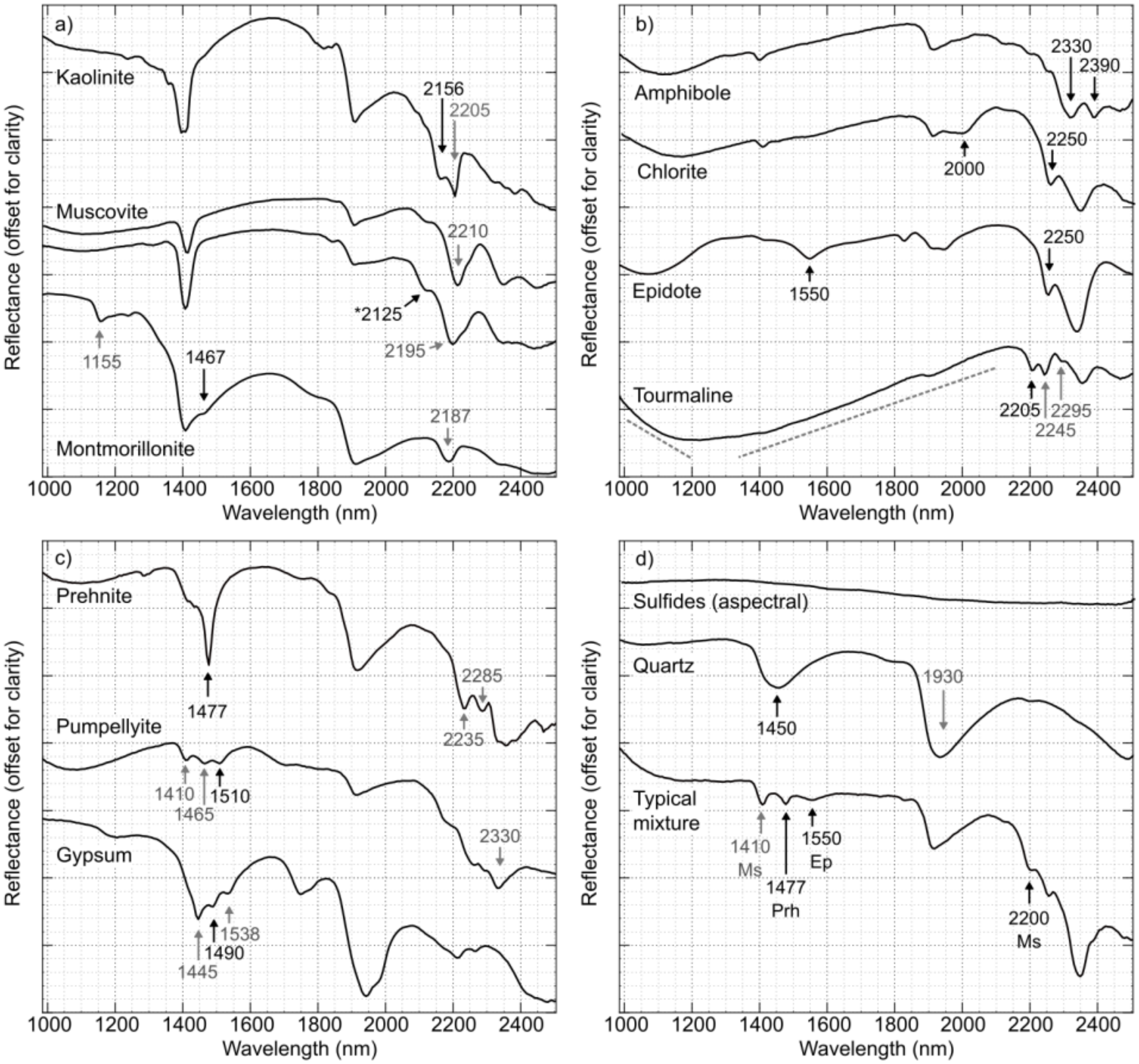

Figure 4-11 *Mineral spectra derived from the sample suite, in all cases obtained from 3x3 pixel averages. Absorptions used for identifications are indicated with black arrows, and additional distinctive absorptions (not used here) are indicated in grey. Dashed lines indicate regions where minerals are identified using the slope of the spectrum (band ratios). Spectra are offset and scaled for clarity, but are not continuum removed. a) Spectra of Al-bearing phyllosilicates. Note that the 2125 nm absorption of white mica is only detectable in coarse-grained samples. b) Spectra of (Fe, Mg)-bearing minerals. c) Spectra of Ca-bearing minerals. d) Spectra of*

aspectral minerals (top), and a typical mineral mixture (bottom) occurring in the sample suite, showing prehnite, epidote and white mica within a single spectrum.

The spectral features used for mineral identification presented in Figure 4-11 are also reported in

Table **4-5**, which in addition provides a list of minerals that could potentially cause spectral interference, and also lists references to recent studies investigating the spectral response of the given mineral, if available. As an example of the mineral identification process, prehnite can be uniquely identified by the presence of a single diagnostic absorption at 1477 nm (Figure 4-11a). Tourmaline on the other hand can only be identified by the combination of a non-diagnostic absorption at 2205 nm (an absorption at this position could also be from kaolinite or white mica) and by a strong negative spectral slope between 1000 and 1200 nm and a strong positive slope between 1400 and 2100 nm (spectral slopes are indicated by dashed lines on Figure 4-11b). The presence of spectrally inactive minerals can also be inferred from spectral characteristics. For example, quartz is identified by the presence of a broad water-related absorption near 1450 nm (from fluid inclusions), while the presence of sulfides is inferred from pixels that show a flat spectral response across the entire SWIR spectral range (i.e., aspectral pixels). Aspectral pixels are identified as those having no detectable absorptions near 1400, 1900, 2200 or 2350 nm, and are then further filtered to exclude pixels with a spectral slope between 1000 nm and 1200 nm, related to Fe electronic absorptions (Hunt and Salisbury, 1970). In all cases, the spectra presented here have a high degree of similarity to those in the listed references, as well as to those available in the USGS spectral library (Kokaly et al. 2017). Several thin sections available from the sample suite also served to confirm the nature of minerals that were spectrally identified but not apparent to the naked eye (i.e., the presence of green epidote or black tourmaline can be readily confirmed with the naked eye, but pale greenish prehnite and pumpellyite is not readily visually identifiable).

In the majority of samples in the current study, mineral mixtures are common, where several minerals can be present within a given pixel (i.e., in a single spectrum). In many cases, such as the mixture spectrum shown in Figure 4-11d, absorption features unique to a given mineral nonetheless allow for an unambiguous identification. In the example spectrum, prehnite and epidote can respectively be identified from diagnostic absorptions at 1477 nm and 1550 nm. The presence of white mica is identified from the absorption near 2200 nm, combined with the lack of absorptions near 1460 nm or 2160 nm (ruling out the presence of montmorillonite or kaolinite, respectively). In other instances, however, white mica cannot be unambiguously identified. Illite (inferred from a deeper 1900 nm absorption) cannot be spectrally discriminated from muscovite in the current dataset, as several other phases show absorptions near this position. Spectral mixtures of either montmorillonite (absorptions at 1460 nm and 2200 nm) or kaolinite (absorptions at 2160 nm and 2205 nm) would also make the detection of fine-grained white mica (single major absorption near 2200 nm) ambiguous at best, as no absorptions unique to white mica would be present. The effects of spectral mixtures between kaolinite and fine-grained white mica are further addressed in the section 4.5.4.

Table 4-5 *Spectrally detectable mineralogy at Highland-Valley*

General group	Mineral	Diagnostic absorptions	Causes interference to:	Reference
Al-bearing	**Montmorillonite** (Mnt) $(Na,Ca)_{0.33}(Al,Mg)_2(Si_4O_{10})(OH)_2\cdot nH_2O$	1467 nm		Post and Noble, 1993; Bishop et al., 2008
	Kaolinite (Kaol) $Al_2Si_2O_5(OH)_4$	2160 nm	Mt, Ms, Tr	Bishop et al. 2008
	Muscovite (Ms) $KAl_2(AlSi_3O_{10})(OH)_2$	2125 nm, 2200 nm (coarse grained only)	Kaol, Mt, Tr	Duke, 1994; Lypaczewski et al. 2019
Ca-bearing	**Gypsum** (Gyp) $CaSO_4\cdot 2H_2O$		Pump	Harrison, 2012
	Prehnite (Prh) $Ca_2Al_2Si_3O_{10}(OH)_2$	1477 nm	Chl (2250 nm)	White et al., 2017
	Pumpellyite (Pmp) $Ca_2(Mg, Fe)Al_2(SiO_4)(Si_2O_7)(OH)_2\cdot(H_2O)$	1510 nm	-	White et al., 2017
(Fe,Mg)-bearing	**Epidote** (Ep) $Ca_2(Al, Fe)_2(SiO_4)_3(OH)$	1540 nm 2250 nm	Chl (2250 nm), Tr	Roache et al., 2011
	Amphibole (Am) $Ca_2(Mg, Fe)_5Si_8O_{22}(OH)_2$	2330 nm 2390 nm	Chl	Laukamp et al. 2012
	Chlorite (Chl) $(Mg, Fe)_5Al(AlSi_3)O_{10}(OH)_8$	2000 nm 2250 nm	Amp, Ep, Tr	McLeod et al. 1987; Lypaczewski and Rivard, 2018
	Tourmaline (Tur) $Na(Mg, Fe)_3Al_6(Si_6O_{18})(BO_3)_3(OH)_3(OH)$	2205 nm 2245 nm Slope 1000 nm/1180 nm	Ms, Kaol, Mt, Chl (2250 nm)	Taran et al., 1993; Bierwirth, 2008.
Spectrally inactive	**Sulfides** (Sulf.) $([Cu], Fe)S_2$	Flat spectrum	-	Kokaly et al., 2017
	Quartz (Qz) SiO_2	Inferred from 1450 nm H_2O absorption	-	Clark, 1981; Entezari et al., 2017

4.3.5 White mica thickness estimation

In addition to allowing the identification of mineralogy, spectral metrics can provide information on physical characteristics of certain minerals. White mica is a relatively weak absorber (i.e., as opposed to darker minerals such as biotite), and is translucent even for relatively large crystal thicknesses (along the c-axis). Reflectance measurements performed with crystal samples of increasing thickness (increasing optical path length) yield spectra that appear to follow the Beer-Lambert law, for samples up to a few millimeters in thickness. That is, absorption features become increasingly pronounced with increasing sample thickness, up to band saturation. With increasing sample thickness, several minor absorptions become increasingly apparent, for example near 1840 nm or 2125 nm. Figure 4-12a presents reflectance measurements from increasingly thick white mica sheets (parted from the same original crystal book) laid flat on a Spectralon white panel. With increasing thickness, the absolute reflectance decreases across the entire spectral range, and the strong absorptions rapidly become saturated (e.g., at 2200 nm). Of interest is that the relative strengths of the weak to strong absorptions increase differentially with sample thickness (i.e., the weak 2125 nm absorption increases in depth while the strong 2200 nm absorption becomes saturated). Thus, as presented in Figure 4-12b, the ratio between the strength of the second derivative of the 2125 nm to the 2200 nm absorptions can be used to estimate white mica thickness, up to 3 mm. Above this thickness, the relationship is not valid as the saturated absorptions become too broad for strengths to be correctly estimated.

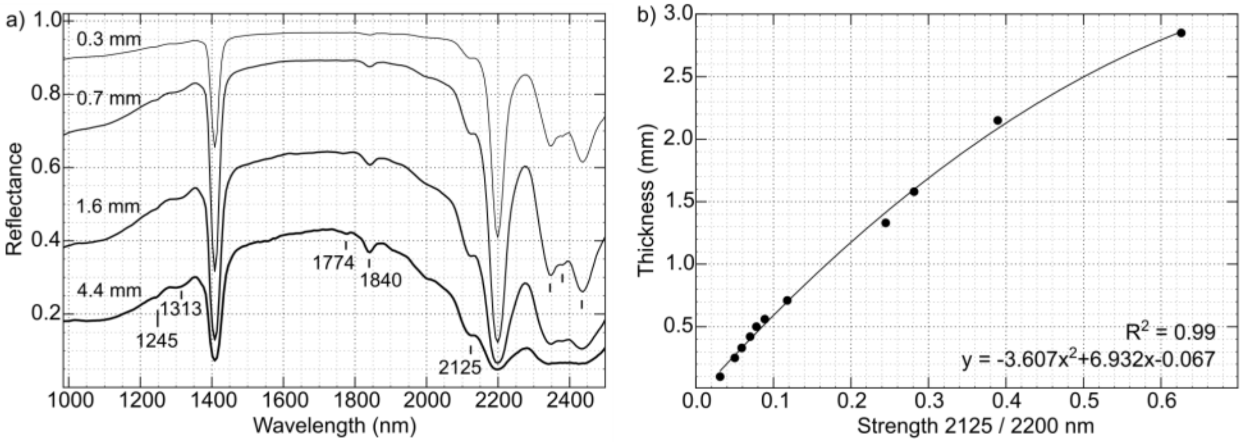

Figure 4-12 *Variation of the spectral response of white mica as a function of thickness. a) Spectra of white mica sheets of variable thickness, measured with precision callipers. Reflectance spectra are shown without any offset, and are not continuum removed. b) Correlation between the relative second derivative strengths of the 2125 nm and 2200 nm absorptions to sample thickness.*

Although the relationship was established using white mica layers parted from a pure crystal and placed on a white panel, the same effect is observed in natural samples, where fine-grained matrix white mica (e.g., from sericitized feldspars) is spectrally distinguishable from coarse-grained white mica phenocrysts based on this ratio. In this study, coarse-grained refers to white mica presenting a thickness above 1 millimeter, or a 2125 nm over 2200 nm ratio of approximately 0.16.

4.3.6 Estimation of relative modal mineral abundances

Hyperspectral data for the 755 slabs from the Guichon Creek batholith were analyzed to extract relative modal abundances of the 12 minerals listed in Table 1, as well as apparent white mica thickness (referred to as grain size). Spectral imagery is analyzed on a per-pixel basis, with each pixel possibly indicating the presence of one or several minerals, based on the criteria presented in Figure 4-11 and

Table **4-5**. For each slab sample, a relative modal abundance for each mineral is calculated as the number of pixels with the given mineral over the total number of pixels in the sample (note that a single pixel can have multiple, one, or no minerals detected). That is, the relative modal abundances reported in this study only represent relative changes in abundance for the investigated mineral within the sample suite, and are not true modal abundances as these do not take into account all phases present in a rock (e.g., feldspars cannot be accounted for). As an example of the modal abundance estimation process, Figure 4-4 shows the relative abundance of prehnite in two samples, respectively at 12% and 54%. For continuous drill core, a relative mineral abundance value is reported for every 20 cm section of core.

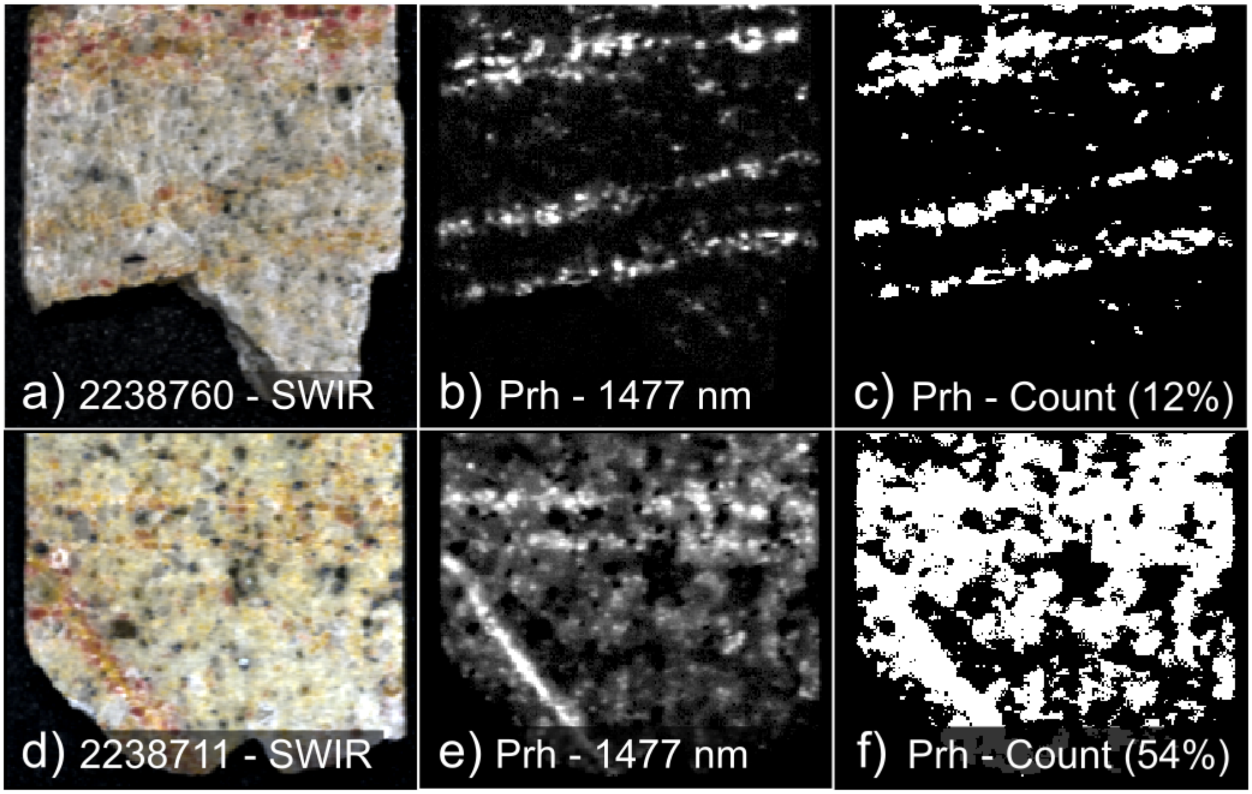

Figure 4-13 *Pixel count example. a) False color SWIR imagery. b) Processed hyperspectral image showing the relative strength of the 1477 nm absorption, indicating the presence of prehnite. c) Pixel count of the image shown in b), indicating 12% of the total pixels contain prehnite. c) False color SWIR imagery. d) Processed hyperspectral image showing the relative*

strength of the 1477 nm absorption. f) Pixel count of the image shown in e), indicating 54% of the total pixels contain prehnite.

4.3.7 Alteration score used for the detection of mineralized samples

In most mineral deposits, mineralogy in altered and mineralized samples is distinct from that of background, unaltered and unmineralized samples. At Highland Valley, mineralization in the form of copper-iron sulfides occur in quartz veins with coarse muscovite selvages, and kaolinite is also common within the deposit. In some areas, tourmaline breccias are reported to be associated with mineralization, and may be overprinted by epidote. Prehnite is common in distal propylitic alteration zones (Byrne et al. 2017).

Here, a simple alteration score is developed based on the presence or absence of minerals that are known to occur with mineralization, and that are spectrally detectable in the SWIR spectral range. This metric can be used to estimate the degree of alteration in a given sample (or drill core interval), and could potentially be used to discriminate mineralized from unmineralized samples (i.e., for ore-sorting). For each sample, a modal abundance is calculated for each of the minerals associated to mineralization, here including sulfides, quartz, coarse-grained muscovite, kaolinite, tourmaline, and epidote. An alteration score is calculated by adding a value of one for each alteration mineral present above a given threshold in a sample, and a score of two is added for tourmaline and sulfides, which occur exclusively in mineralized samples. Generally, a threshold of 5% of the pixels (i.e., modal abundance) is used to determine the presence of a mineral within a sample, or 0.1% for sulfides. That is, a sample with a spectrally estimated modal abundance of over 5% for both kaolinite and tourmaline would obtain an alteration score of three. An example of modal abundance estimation was shown in Figure 4-13. Note that, as each mineral is identified independently, several minerals could potentially be present within a single pixel, such as shown in the mixture spectrum in Figure 4-11d.

4.4 Results

Unlike conventional analytical techniques that provide information on limited scales (i.e., thin sections), hyperspectral imaging provides mineralogical information on a range of scales, from thin sections offcuts (2 cm by 4 cm), hand samples (10 cm by 10 cm), to entire drill cores (meters). In the following section, hyperspectral data is presented for samples at increasingly larger scales, from hand samples to drill cores. High-resolution imagery on small-scales allows the characterization of veins, veinlets and vein selvages. Mineralogical patterns related to alteration can thus be recognized, and spectral metrics to identify mineralized samples can be developed. These metrics can then be applied on large-scales, to delineate mineralized interval in drill cores and facilitate core logging, or to outline potential mineral deposits on regional-scales.

4.4.1 Sample scale variability in the Bethsaida and Skeena facies

The Bethsaida granites to granodiorites are one of the main hosts to mineralization in the Highland Valley district, hosting the Valley and part of the Lornex deposit, both of which formed during the younger mineralizing event in the district. In these deposits, mineralization is intimately linked to quartz veins that present coarse-grained grey muscovite selvages (early-halo veins, Alva-Jimenez, 2011; Byrne et al. 2013). Kaolinite may also be present throughout these systems. A total of 331 slab samples were acquired in the Bethsaida facies and enclosed felsic dykes, and a total of 42 samples from this group are mineralized (defined by grades above approximately 1000 ppm Cu). Figure 4-14 presents hyperspectral imagery of typical samples from the Bethsaida facies, with a mineralized sample from the Valley deposit, and an unmineralized sample from 2 km west of the open pit.

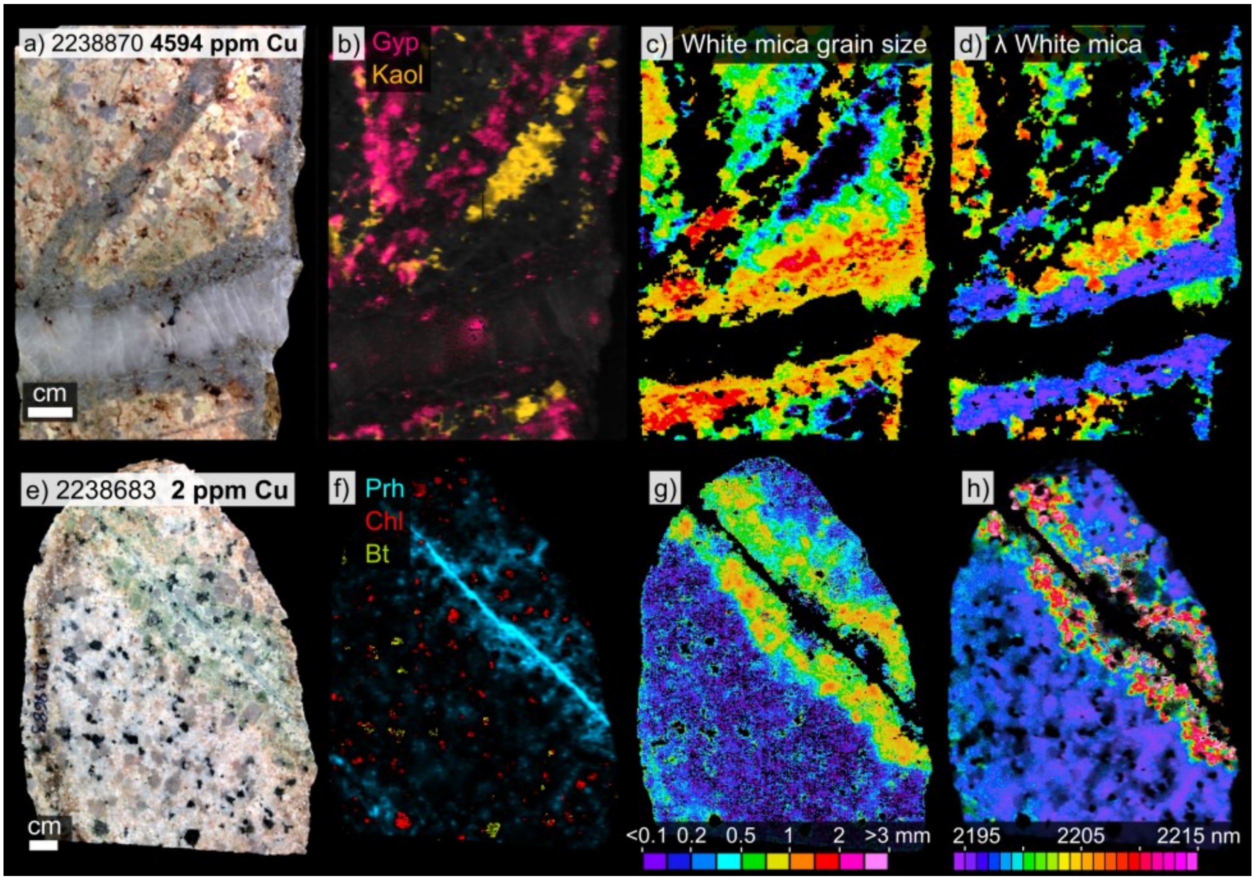

Figure 4-14 *Photographs and processed hyperspectral imagery of samples from the Bethsaida facies. Top: A mineralized sample from within the Valley open pit; a) color photograph; b) distribution of kaolinite (orange) and gypsum (pink); c) spectrally determined white mica grain size (color-scale at bottom) and; d) absorption position of the 2200 nm* Al_2*-OH feature exclusively for white mica pixels above 0.5 mm in thickness (color scale at bottom). Bottom: An unmineralized sample located 2 km west of the Valley open pit; e) color photograph; f) distribution of prehnite; g) spectrally determined white mica grain size, and; h) absorption position of the 2200 nm* Al_2*-OH feature for white mica.*

In the mineralized sample (Figure 4-14, top), spectrally detected mineralogy is consistent with the reported alteration styles in the Bethsaida facies. The quartz vein selvage consists of coarse-grained white mica, and kaolinite is present in the altered groundmass (Figure 4-14b). Gypsum is present throughout as an overprinting mineral (Figure 4-14b), although it may not be present in most samples. The grey muscovite, forming the selvage of mineralized veins described in previous studies, corresponds here to the coarse-grained (generally above 1 mm, Figure 4-14c) muscovitic (high-Al) white mica, with an Al_2-OH absorption feature near 2195 nm (Figure 4-14d). Immediately adjacent to this grey muscovite, coarse-grained green white mica (described in Alva-Jimenez, 2011) is phengitic (Figure 4-14d), with an absorption near 2210 nm, although in other mineralized samples phengitic mica may be absent. Note that Figure 4-14d was filtered to remove interference from kaolinite by only showing pixels with coarse-grained white mica, with a ratio of the 2125 nm to 2200 nm absorptions above 0.1 (corresponding to a thickness above 0.5 mm). Kaolinite does not have any absorption near 2125 nm, resulting in a ratio of zero. Masking pixels with a ratio below 0.1 therefore eliminates both fine-grained white mica and kaolinite.

A typical unmineralized (but altered) sample from the Bethsaida facies is presented in Figure 4-14 (bottom). Spectrally identified mineralogy is consistent with the prehnite-rich propylitic alteration domain described in Byrne et al (2017). Figure 4-14f displays spectral imagery highlighting the presence of a prehnite vein, with a vein selvage consisting of low amounts of prehnite and coarse-grained (Figure 4-14g) phengitic white mica (Figure 4-14h), with an absorption near 2210 nm. In most samples, this coarse-grained white mica is restricted to the immediate vicinity of veins (1 to 5 cm). In many cases, weakly altered to unaltered background mineralogy is detectable away from veins (e.g., on the lower-left portion of the unmineralized sample in Figure 4-14). Here, this consists of fine-grained white mica (muscovite and/or illite) ± montmorillonite, which together always show low absorption wavelengths, at or below 2195 nm. In many cases, least altered rocks contain minor amounts of prehnite throughout (Figure 4-14f, bottom left part), or may alternatively at times be dominated by montmorillonite (Appendix A, sample 2232402), or more rarely by pumpellyite (Appendix A, sample 2247917).

In the Bethsaida facies, epidote veins are at times present within the propylitic alteration zone, but are subordinate to prehnite veins and veinlets.

The Skeena facies is represented by a total of 118 samples, 15 of which contain sulfide mineralization. This facies is the main host rock for the Lornex and part of the Bethlehem deposits, and the entirety of the Highmont deposit. Skeena facies rocks present similar mineralogy to Bethsaida, with a major difference being that epidote veins or veinlets are ubiquitous, often with selvages consisting of prehnite (Appendix A, sample 2015KB249), with or without associated coarse-grained phengitic (long wavelength, near 2210 nm) white mica.

4.4.2 Sample scale variability in the Bethlehem and other facies

The Bethlehem deposit (not currently in production) and the >160 distal showings across the Guichon Creek batholith were not the focus of the NSERC-CMIC "Footprints" project, but several samples were nonetheless collected as part of investigations of the distal alteration footprint, and are briefly described here. The Bethlehem lithofacies rocks are grouped with the other two more mafic facies forming the outer margins of the Guichon Creek batholith (the Highland Valley and Border facies), and include the Bethlehem deposit and numerous peripheral Cu showings. Of the 306 samples from these lithofacies, 11 were mineralized (here defined as >1000 ppm Cu), and, although the majority were from distal showings, all present broadly similar alteration patterns.

Figure 4-15 (top) presents a typical mineralized sample from the Guichon subfacies of the Highland Valley facies, and is located less than 200 m northeast of the Bethlehem open pit. Figure 4-15 (bottom) presents a typical unmineralized (but partially altered) sample from the

Bethlehem facies, located 6 km to the west of the Lornex pit. This sample corresponds to the propylitic alteration zone described by Byrne (2016).

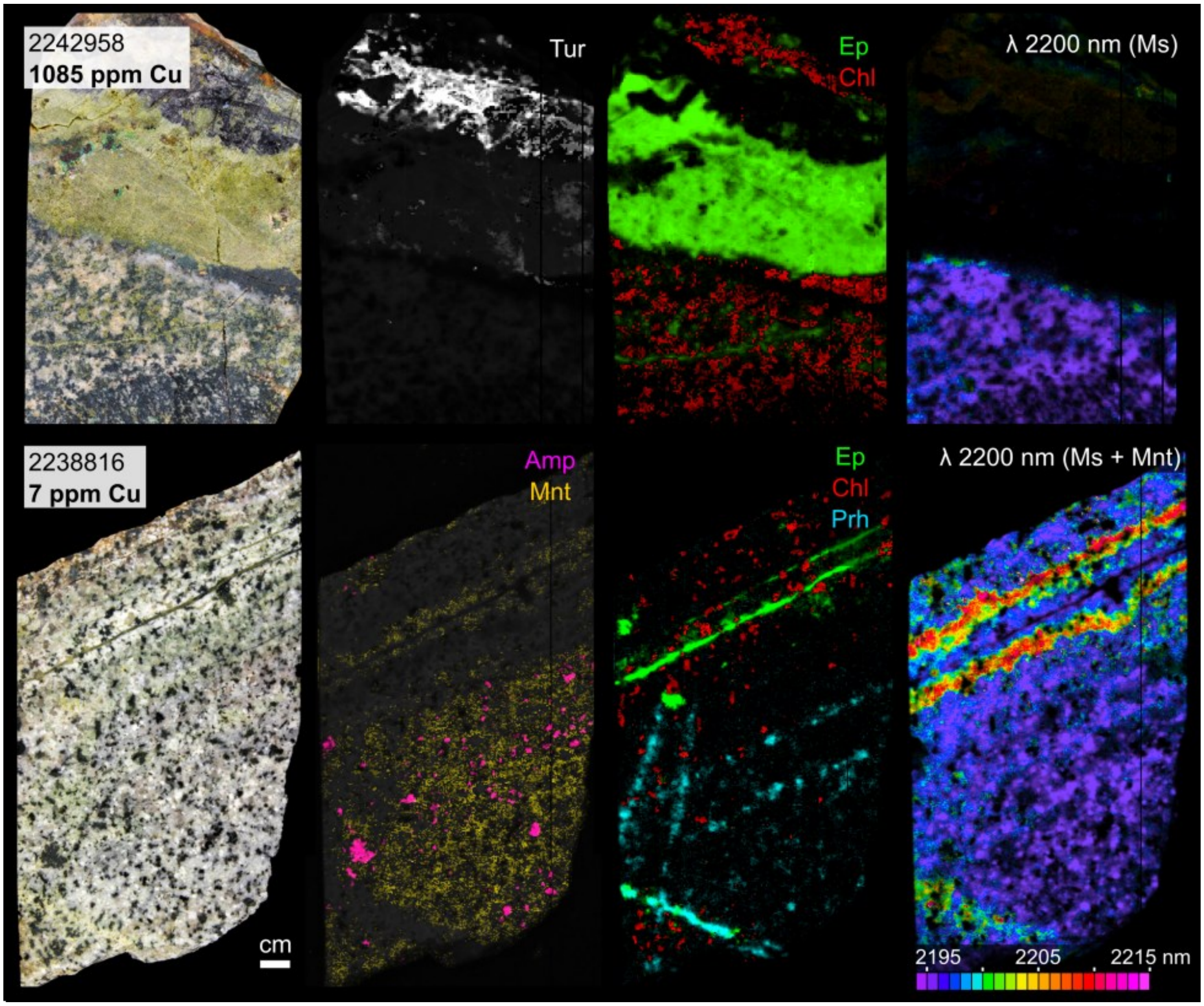

Figure 4-15 *Photographs and processed hyperspectral imagery of samples from the Bethsaida deposit. Top: Sample 2242958, a mineralized sample from the Guichon facies; a) color photograph; b) distribution of tourmaline; c) distribution of epidote (green) and chlorite (red), and d) position of the 2200 nm absorption. Bottom: Sample 2238816, an unmineralized sample from 6 km away from the open pit, with 7 ppm Cu; e) color photograph; f) distribution of montmorillonite (yellow); g) distribution of chlorite (red), epidote (green), prehnite (blue), and amphibole (purple), and h) the absorption position of the 2200 nm* Al_2*-OH feature for white mica the mixture of white mica and montmorillonite.*

In the Bethlehem deposit (and in the Bethlehem or Highland Valley facies rock) mineralization occurs in the presence of tourmaline veins (or breccia, Appendix A, sample 2234423), often associated to significant amounts of epidote (Figure 4-15, top), but generally lack the coarse-grained grey muscovite (Al-rich) that is characteristic of mineralization in the Bethsaida and Skeena facies. In vein selvages, chlorite is abundant, and gives way to amphibole in unaltered portions of the samples (Figures 5f and g). The felsic mineral matrix consists of fine-grained Al-rich muscovite (absorption near 2195 nm, Figure 4-15d), generally without montmorillonite (no absorption near 1460 nm). In unmineralized (but partially altered) samples (Figure 5, bottom), small epidote veins or veinlets are widespread, and present centimeter-sized selvages that may contain intermediate to coarse-grained (0.2 to 0.5 mm) phengitic white mica (long absorption positions, near 2215 nm). In many samples, however, phengitic alteration is weak, and appears to either not have developed, or to have been partially or completely overprinted by short-wavelength (2195 nm) white mica, illite and/or montmorillonite (e.g., Figure 5f). Prehnite is common in the least altered samples (it is present in over half the samples in this group), and can variably occur as overprinting veinlets, as relict veinlets overprinted (cross-cut) by epidote veinlets, as vein selvages, or as dissemination. The general alteration pattern in the Bethlehem deposit therefore ranges from tourmaline and epidote veins with proximal chlorite (± phengite) selvages, to more distal prehnite (± montmorillonite) selvages or groundmass alteration, and finally to unaltered protolith amphibole.

4.4.3 Mineral chemistry of epidote

Epidote group minerals are important alteration minerals in porphyry-Cu systems, as they are one of the most conspicuous indicators of alteration, often presenting an easily identifiable pistachio-green color. Epidote is ubiquitous at HVC, particularly in the Bethlehem and more mafic lithofacies. As for several other minerals investigated using hyperspectral imaging, the mineral chemistry of the epidote-clinozoisite solid solution can be estimated from the position of the characteristic absorption near 1550 nm. Epidote endmember, with an $X_{Fe} = [Fe^{3+}/(Fe^{3+}, Al)]$ of ≈ 0.33 has its main absorption near 1542 nm, while endmember clinozoisite ($X_{Fe} = 0$) has its main absorption near 1558 nm, and variations in this position were recorded to vary within various alteration zones in an Australian Archean gold deposit (Roache et al., 2011). This metric was investigated here as a potential vector to mineralization, with inconclusive results. Zonations in the absorption position (i.e., changes in mineral chemistry) were noted to occur within single veins, and multiple veins within the same sample could present markedly different compositions. Both patterns are illustrated in Figure 4-16. Here, the left epidote vein shows a central portion with absorptions near 1551 nm, grading to 1545 nm near the edges of the vein. The second vein, on the right side of the sample, shows a main absorption position between 1552 nm and 1555 nm. Because of the potential for variable epidote chemistry within any given sample, no systematic alteration patterns emerged on the 755 slab samples either from epidote relative modal abundances, or from epidote chemistry (note that Byrne, 2019, reported systematic changes in trace element in epidote with distance to mineralization, but these are not detectable using SWIR hyperspectral imaging).

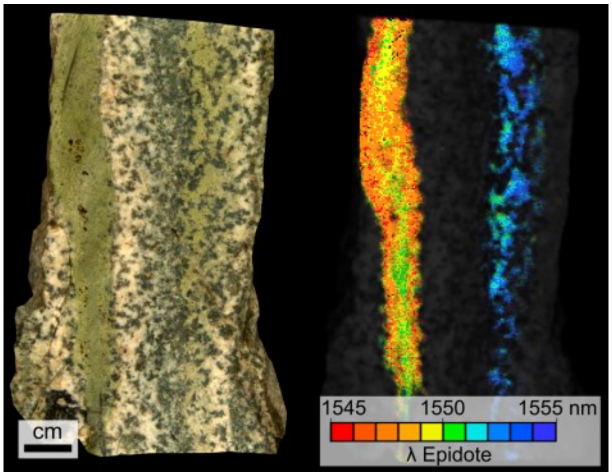

Figure 4-16 *Non-mineralized sample 2015KB102 (21 ppm Cu) from the propylitic alteration zone of the Guichon lithofacies, 3 km east of the Bethlehem deposit. a) Sample photograph. b) Hyperspectral imagery processed to display the position of the 1550 nm absorption feature of epidote.*

4.4.4 Alteration score and detection of mineralized samples

Based on the detectable changes in mineralogy described in sections 4.4.1 and 4.4.2, a spectral alteration score can be defined to estimate the degree of alteration in a given sample (the methodology was described in section 4.3.7). This metric relies on the presence or absence of a given set of minerals in each sample, where the presence of a mineral above (or below) a given modal abundance threshold yields a score of one (or two in certain cases). Table 4-6 presents a set of minerals that can serve to determine the degree of alteration in each of the rock groups in the Guichon Creek batholith and can also be used to distinguish between mineralized and unmineralized samples, as defined by a grade of 1000 ppm Cu.

Table 4-6 *Mineralogical parameters used for the spectral alteration score**

Group	Qz >5%	Kaol. >5%	Coarse Ms >5%	Prh <5%	Ep <0.5%	Ep >20%	Tur. >5%	Sulf. >0.1%
Bethsaida + Dykes (N=331)	1	1	1	1				
Skeena			1	1	1	1		

(N=118)								
Bethlehem and more mafic (N=306)				1	1	1	2	2
Global (N=755)	1	1	1	1	1	1	2	2

*For each mineral, the modal percentage shown is the cut-off above (or below) which a sample will obtain the indicated score. Qz = quartz, Kaol = kaolinite, Coarse Ms = coarse grained white mica, Prh = prehnite, Ep = epidote, Tur = tourmaline, Sulf. = sulfides.

For the Bethsaida facies and associated felsic dykes, the presence of over 5% of quartz, kaolinite, or coarse-grained muscovite (using a threshold of 1 mm), or the presence of less than 5% prehnite in a given sample each give a value of one to the alteration score. For the Skeena variety, the presence of over 5% of coarse-grained muscovite, less than 5% prehnite, and either less than 0.5% or over 20% epidote each give a value of one. For the Bethlehem and more mafic facies, less than 5% prehnite, less than 0.5% or over 20% epidote each give a value of one, and the presence of over 5% tourmaline or over 0.1% sulfides each give a value of two. Note that the exact abundance threshold is not critical to the good performance of the metric, but may serve to fine-tune results.

A scatter plot between the alteration score (obtained using the global metric defined in Table 2) and Cu concentration for the 755 slab samples is presented in Figure 4-17. Samples scoring two or above are considered mineralized. That is, samples with two minerals above (or below) the set threshold are classified as mineralized, while samples with tourmaline or sulfides (each giving a score of two) are always considered to be mineralized. The performance of this metric is reported for each rock group in the lower right side of Figure 4-17, and the last row reports the performance for the global set of mineralogical parameters, used to classify the 755 rock slabs regardless of lithofacies. Here, sensitivity refers to the true positive rate (i.e., the percentage of mineralized samples correctly identified as such), and specificity refers to the true negative rate (i.e., the percentage of unmineralized samples identified as such). For example, for the Bethsaida and associated felsic dykes, 87% of the mineralized samples obtain an alteration score at or above two, and 80% of the unmineralized samples obtain a score of zero or one. Importantly, by varying the abundance thresholds presented in Table 4-6, the resulting sensitivity or specificity may easily be adjusted. For example, changing the threshold for prehnite from 5% to 0.5%, decreases sensitivity in the Bethsaida facies from 87% to 85%, but increases specificity from 80% to 85%.

Generally, increasing spectral alteration scores are linked to higher Cu concentrations within a given sample. Determining the exact Cu content of a given sample, however, is not possible, as Cu concentrations can vary by orders of magnitude within a given score value. For example, samples with a score of zero can have a Cu content between 1 and 1000 ppm, while those with a spectral alteration score of five can have Cu concentrations between 300 to 10000 ppm.

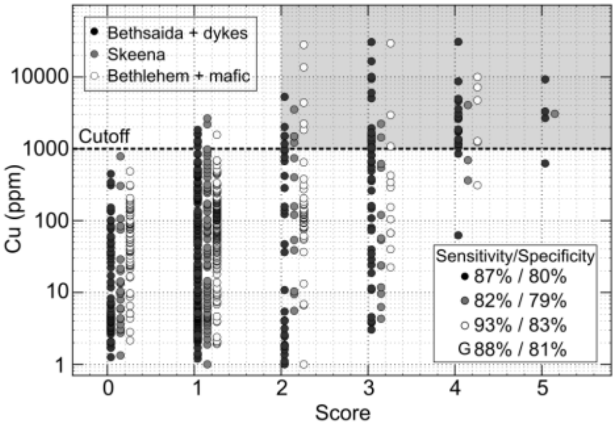

Figure 4-17 *Correlation between the Cu concentration and the spectral alteration score obtained for the 755 slabs using the common mineralogical parameters. Samples scoring 2 or above are considered mineralized (>1000 ppm Cu). Classification results (sensitivity/specificity) are listed in the lower right for each rock group, as well as for the entirety of the dataset (G).*

4.4.5 Mineralogical patterns on drill core scales

Hyperspectral imaging allows analyzing large samples (e.g., drill cores), which may reveal decimeter- to meter-scale mineralogical patterns that would otherwise not be detectable on smaller scales. It may also provide insights into the continuity (or discontinuity) of hydrothermal alteration around mineralized intervals. The mineralogical patterns previously identified from hand samples and the resulting spectral alteration score are employed here to delineate potentially mineralized intervals directly on 400 meters of continuous drill core.

Figure 4-18 presents summary downhole plots for drill core V15-021, drilled into the Bethsaida granodiorite, 900 meters southwest of the Valley deposit. The core intersects both mineralized and unmineralized intervals, and ore grades, as assayed by the mining company, are reported in Figure 4-18j. The main ore zone is highlighted by the red dashed outline. Within this particular drill hole, the most obvious change in mineralogy within nearly the entirety of the mineralized interval is the presence of intense quartz veins (Figure 4-18g), with sulfides detected within restricted intervals (Figure 4-18h, several cm-sized sulfide veins are present in the core at these locations). Intense quartz veining, however, is not always indicative of mineralization at HVC, as barren quartz-rich zones (the barren core) are known to occur in portions of the deposit. On the other hand, coarse-grained white mica (generally above 1 mm in thickness, from the spectral metric defined in section 3.5), is nearly always indicative of mineralization, and is abundant within and immediately surrounding the quartz vein (Figure 4-18f). Low abundances of kaolinite can also occur within the mineralized zone, but the largest amounts occur over several hundred meters immediately surrounding the main ore zone (Figure 4-18e). Distally, where kaolinite alteration is less intense, prehnite veins become sporadically apparent (Figure 4-18d). Together, these minerals define the spectral alteration score (Table 4-6). The effectiveness of this metric can be assessed from downhole data, where all intervals assayed above 0.3% Cu (between 250 m and 300 m), and most intervals above 0.1% Cu show a score at or above two (Figure 4-18i). Note that, although in this particular drill core, the spectral alteration score appears to be particularly dependent on white mica grain size, the other minerals defining this metric are nonetheless essential to obtain adequate classification results in other HVC samples.

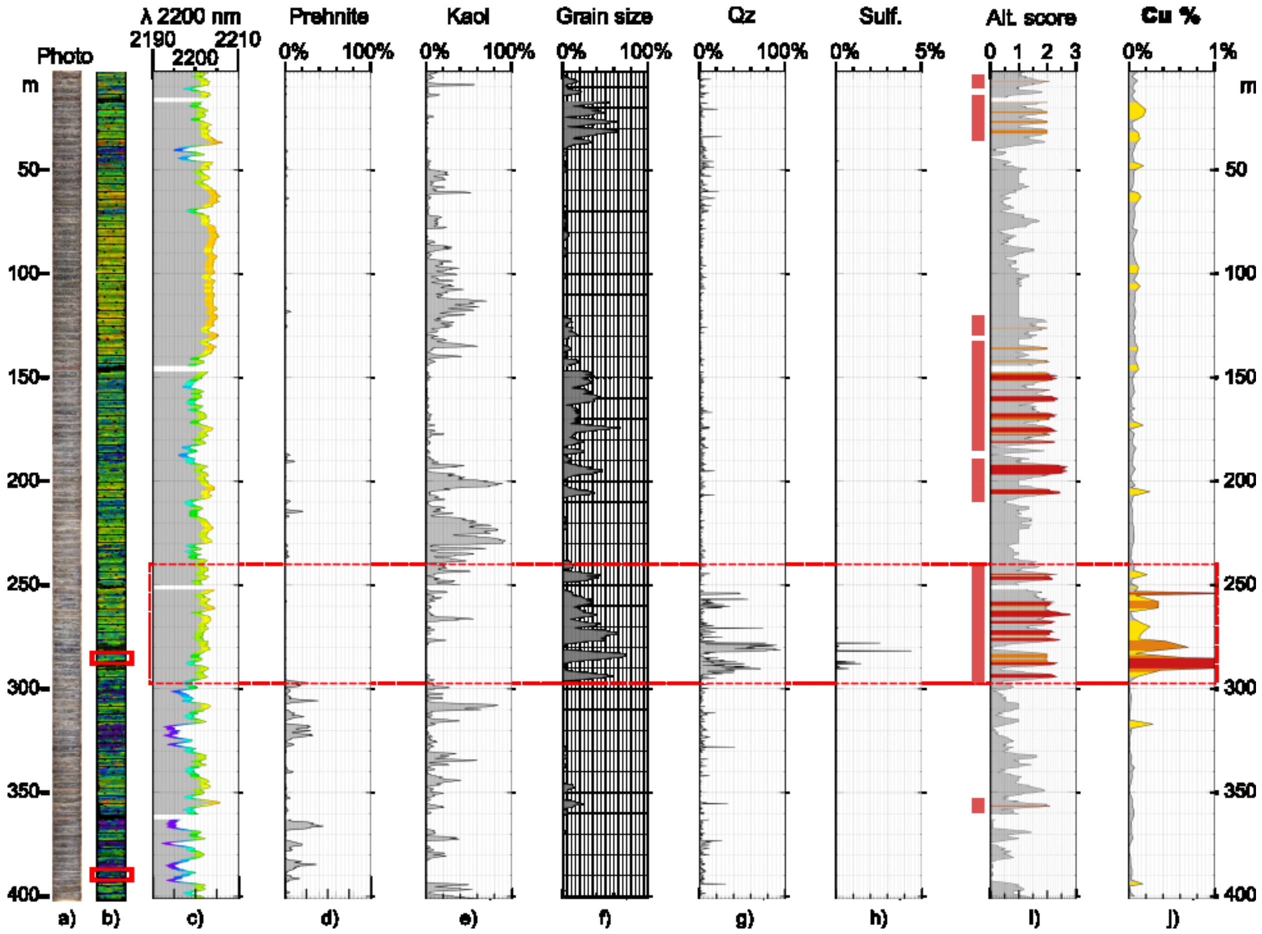

Figure 4-18 *Downhole data from 400 m of drill core V15-021. a) Stacked photographs of 111 core boxes. b) Color-coded hyperspectral imagery displaying the position of the 2200 nm absorption feature (not filtered by mineralogy). The locations of boxes shown in* Figure 4-19 *are indicated. c) Downhole graph of the 2200 nm absorption position, for every 20 cm interval of core, smoothed using a 2 m moving average. The following plots are smoothed downhole modal abundances of d) prehnite; e) kaolinite; f) coarse-grained white mica, and non-smoothed modal abundances of g) quartz; h) sulfides; i) Spectral alteration score. Intervals of core with a score above 2 are shaded in red, and red outlines immediately to the left provide a*

3 m buffer on either side of any altered zone. j) Downhole Cu grade. The plot is capped at 1% Cu, with areas above this grade highlighted in red (the maximum grade is 2.1% Cu). Zones above 0.3% Cu are highlighted in orange, and zones above 0.1% Cu in yellow.

Figure 4-19 presents close-up imagery of two core boxes selected from the continuous drill core (location highlighted in Figure 4-18b), showcasing typical mineralogical patterns in both a strongly mineralized interval (Figure 4-19 left, 0.78% Cu), and a weakly altered but barren interval (Figure 4-19, right, 0.03% Cu), 100 meters away from the mineralized zone.

The mineralogical changes seen over several hundred meters of drill core surrounding the ore zone are repeated here on smaller spatial scales (Figure 4-19b). A sulfide vein (3 centimeters) is present within or directly adjacent to a wide quartz vein-rich zone (30 centimeters), which is then surrounded by coarse-grained white mica (a 3 meters zone) that is muscovitic in composition (low wavelength, 2195 nm within the coarsest grains on Figure 4-19c). Kaolinite may be present throughout, and may interfere with the estimation of white mica chemistry. Prehnite and kaolinite occur sporadically in barren intervals in the form of veins of varying orientations, with centimeter- to decimeter-scale selvages. As veins are generally 10 to 50 cm apart, these could not fully be captured on a single hand sample scales (10 cm by 10 cm). Outside of the vein haloes, background, fine-grained white mica (Figure 4-19h, variably with or without montmorillonite, not shown) always shows Al-rich composition (low-wavelengths, below 2195 nm, Figure 4-19g). In transitional areas between the kaolinite veins and white mica background (i.e., in the vein haloes), the apparently intermediate 2200 nm absorptions positions (yellow-green-blue colors, 2204 nm to 2196 nm) are likely caused by mixing between the 2195 nm absorption of background, Al-rich white mica and the 2205 nm absorption of kaolinite (note how all areas above 2195 nm on Figure 4-19g show some amounts kaolinite in Figure 4-19f).

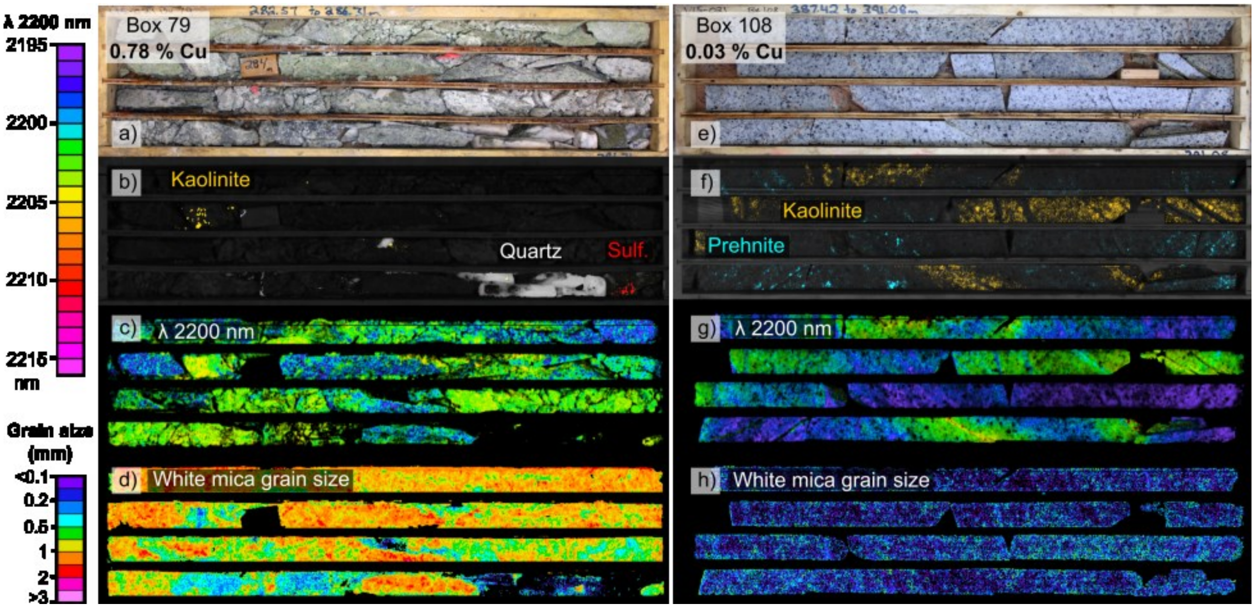

Figure 4-19 *Left: Core box 79 from a mineralized interval. a) Color photograph. Hyperspectral imagery processed to display; b) the distribution of kaolinite (orange), quartz (white) and sulphides (red); c) the position of the 2200 nm absorption feature; d) white mica grain size. Right: Core box 108 from a barren interval. e) Color photograph. Hyperspectral imagery processed to display; f) the distribution of kaolinite (orange) and prehnite (blue); g) the position of the 2200 nm absorption feature; h) white mica grain size.*

4.4.6 Regional scale mineralogical patterns

The 755 slab samples investigated in this study span a roughly 20 km by 40 km area surrounding the Highland Valley deposits, and encompass a large portion of the Guichon Creek batholith. Regional mapping of the mineralogy related to hydrothermal alteration described in sections 4.1 through 4.5 can potentially highlight (or allow vectoring to) mineral deposits. Figure 4-20 presents regional scale geochemical and spectral data for all slab samples, with Cu concentration presented in Figure 4-20a. Most samples above 1000 ppm Cu occur within, or close to the open pits (Valley, Lornex, Bethlehem and Highmont), but several small showings also occur at the periphery of the batholith. Individually, several minerals serve to indicate proximity to mineralization. Gypsum occurs exclusively in mineralized areas within the limits of the open pits, while tourmaline occurs with mineralization in the individual showings. Kaolinite can occur up to 2 km outside the pits, and coarse-grained white mica (above 1 mm in thickness, determined from the spectral metric defined in section 3.5) can be detected up to 4 km away from the deposits. Within the open pits, coarse-grained white mica is muscovitic (high-Al) in composition, showing absorptions near 2195 nm (this corresponds to the grey muscovite referenced in Alva-Jimenez, 2011; Byrne et al. 2013). Prehnite is the most distant spectrally detectable alteration mineral, defining an annular alteration zone extending from 4 km to 8 km around the deposits.

In many cases, prehnite veinlets present selvages of coarse-grained, green-colored phengitic white mica (low-Al, long absorption wavelengths near 2215 nm), while background white mica (which may variably contain illite and/or montmorillonite) always shows small grain sizes (below 0.2 mm, Figure 4-14g) and low absorption wavelengths (near 2195 nm, Figure 4-14h). These mineralogical parameters define the spectral alteration score (as defined in Table 4-6 and Figure 4-17). Samples with high spectral alteration scores are spatially related to the mineralized zones, both within the open pits and in individual showings. Samples also generally show increasingly higher score as mineralization is approached (e.g., immediately southwest of the Valley open pit, from a score of zero at 5 km, to a score of four within the pit). This score could therefore serve as a vector to mineralization on regional scales.

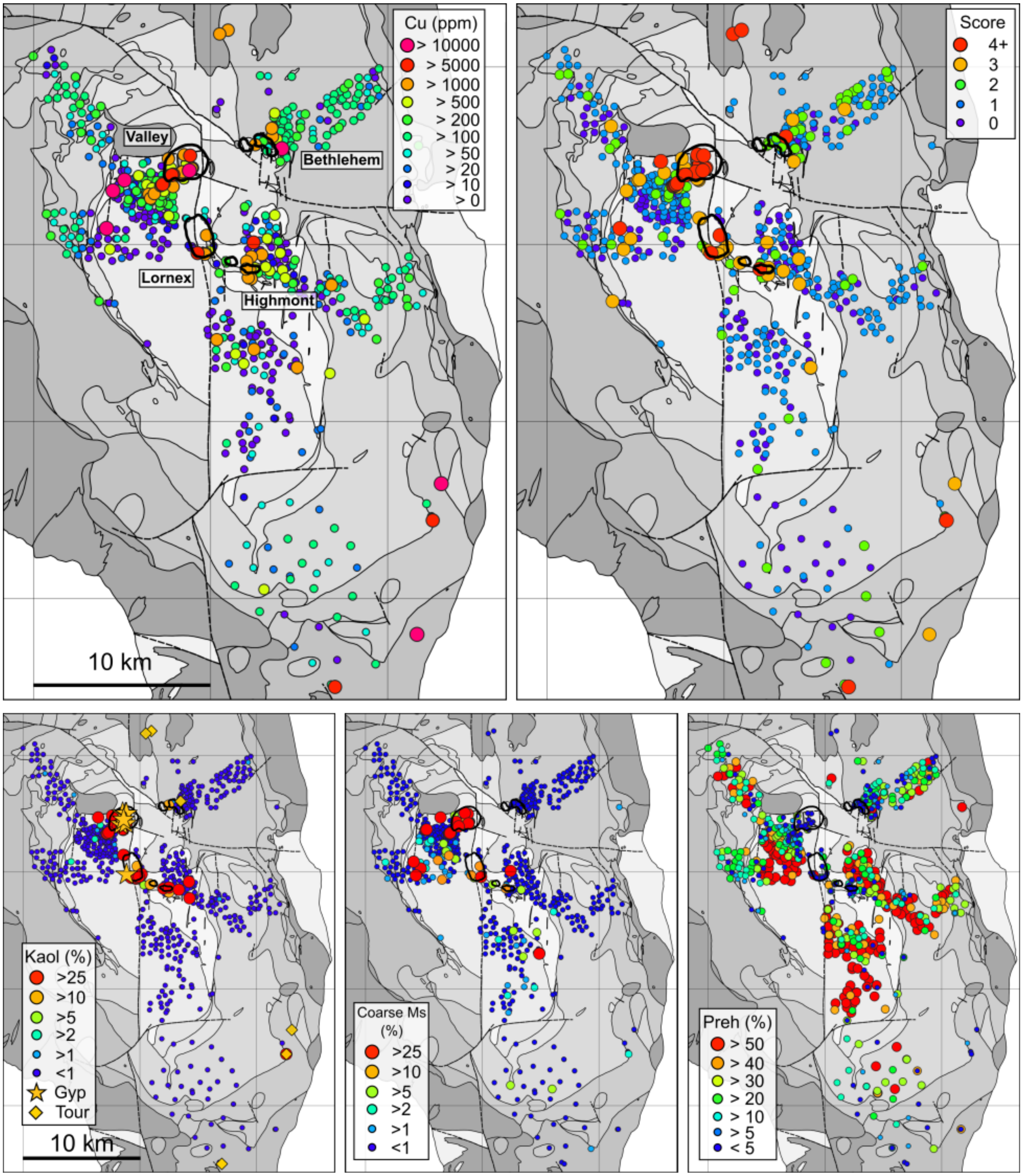

Figure 4-20 *Regional map of the Guichon Creek batholith presenting data obtained from the 755 slab samples. a) Copper concentration (in ppm) for all samples. Several small showings are present at the periphery of the batholith. b) Spectral alteration score as defined in Table 2 (using all minerals). Spectrally derived relative modal abundance of; c) kaolinite, with the presence of*

gypsum and tourmaline (>5%) indicated by stars and diamonds, respectively, d) coarse grained white mica (>1 mm), and e) prehnite. Geology and contacts after Figure 4-1.

4.4.7 Regional scale variability of the 2200 nm feature

The exact position of the 2200 nm absorption of white mica varies with its mineral chemistry, and can therefore be used to estimate its Al^{VI} content (Post and Noble, 1993; Duke, 1994; Swayze et al., 2014). Absorption positions range from 2190 nm for Al-rich (muscovitic) white mica to 2215 nm for Al-poor white mica (phengitic, with substitution of Al^{VI} by Fe or Mg). In many hydrothermal deposits, white mica often presents chemistry that is distinct from background compositions, and can therefore serve as an effective vector towards mineralization. The use of this metric has been investigated at numerous mineral deposits, for example, Harraden et al. (2013) reported that white mica at the Pebble Cu-Au-Mo porphyry was muscovitic (low-wavelength) near mineralization. In Archean gold deposits, white mica is reported to either be muscovitic (Archean Sunrise Dam gold deposit, Wang et al., 2017) or phengitic (Kanowna Belle gold deposit, Wang et al., 2017; Canadian Malartic gold deposit, Lypaczewski et al., 2019) near mineralization. However, other factors, such as protolith composition or metamorphic grade may also affect white mica chemistry and need to be taken into consideration. Variation in the 2200 nm absorption position have been used to map regional metamorphic gradients, where increasingly Al-rich (muscovitic, shorter wavelengths) white mica indicated higher metamorphic grades (Duke 1994; Duke and Lewis, 2010; Lypaczewski et al., 2019).

At HVC, spectral interference can also be problematic. Several minerals may present a potentially interfering absorption near the 2200 nm position, including kaolinite (2207 nm) and tourmaline (2208 nm). As a result, regional scale mapping of the average 2200 nm position for each sample (Figure 4-21) may yield misleading results, if the presence of these minerals is not identified. The data presented in Figure 4-21 illustrates both the effect of protolith control and spectral interference. Unaltered samples in the relatively felsic Bethsaida facies (69 wt% SiO_2) show white mica (muscovite ±illite ±montmorillonite) with absorptions near 2194 nm, while unaltered samples from the more mafic Guichon facies (62 wt% SiO_2) show slightly more phengitic compositions, with absorptions near 2196 nm. Near the open pits, the average absorption position appears to be shifted towards 2207 nm. However, this apparent shift is caused by interference of coexisting kaolinite, as evidenced by the close spatial association of kaolinite-bearing samples (Figure 4-20c), and the lack of white mica of intermediate composition detected on high-resolution hyperspectral imagery (e.g., Figure 4-14h, the background is at 2195 nm, while vein selvages show 2215 nm). Similarly, samples from isolated showings near the periphery of the batholith show absorptions near 2208 nm, caused by interference from tourmaline. Spectral interference therefore needs to be accounted for when obtaining low spatial resolution hyperspectral measurements (e.g., airborne data at 1m/pixel, or non-imaging data from a point spectrometer), which could not necessarily reveal the presence of small amounts of interfering minerals.

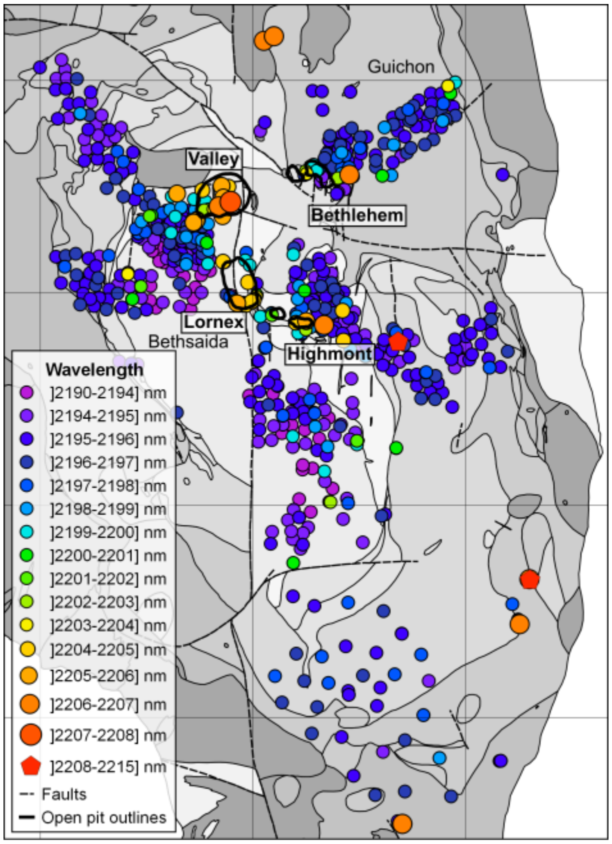

Figure 4-21 *Regional map of the Guichon Creek batholith presenting the average absorption position for each of 755 slab samples.*

4.5 Discussion

4.5.1 Mineralogical variability in the Highland Valley district

At least 10 spectrally active minerals and two spectrally inactive (but nonetheless identifiable) minerals were recognized in samples from the Highland Valley district (

Table **4-5**). Other minerals identified in a few samples include malachite, carbonates, and biotite. These minerals however are difficult to detect in the SWIR in the current sample suite, either due to low modal abundances (e.g., malachite, or non-chloritized, fresh biotite), spectral mixing (i.e., for carbonates, the 2330 nm absorption is difficult to detect in the presence of a number of spectrally active minerals), low signal-to-noise ratios due to the dark nature of the minerals (e.g., large, unaltered biotite books), or most likely a combination of these factors. Minerals presenting an ambiguous, weak, or interfering spectral response may be underestimated in their relative abundance, and spectrally inactive minerals, for the most part, cannot be detected (e.g., feldspars). The use of midwave infrared (MWIR) or longwave infrared (LWIR) hyperspectral instruments may be better suited to investigate some of these minerals. Carbonates, for example, present several absorptions between 3300 nm and 4000 nm (Kokaly et al. 2017) that may mitigate issues of spectral interference seen in the SWIR. Similarly, feldspars can be identified and characterized in the LWIR (e.g., Hecker et al., 2010, Cudahy, 2016), which may provide additional details on the extent of potassic (K-feldspar) or sodic-calcic (albite) alteration. The integration of those additional spectral ranges would likely benefit hyperspectral studies in obtaining a comprehensive understanding of mineralogical changes across ore deposits.

With these constraints in mind, SWIR hyperspectral imaging nonetheless provides novel information on alteration mineralogy in the Highland Valley district. The most conspicuous change related to hydrothermal alteration at the Valley and Lornex deposits is the presence of coarse-grained white mica, as defined from the ratio of its 2125 nm and 2200 nm absorptions. In hand samples, coarse-grained white mica was seen to be limited to a few centimeters around mineralized vein (e.g., Figure 4-14c). Continuous drill core imagery, however, revealed that zone of coarse-grained white mica may occur over several meters within and around strongly mineralized intervals (Figure 4-19d). Kaolinite, when detected during regional exploration, could be indicative of potential mineralization. On deposit-scales, however, downhole imagery reveals that the largest kaolinite abundances occur immediately adjacent to, but not within, strongly mineralized intervals (Figure 4-18e). The use of interpreted mineralogy must therefore take into account the scale of observation. In a regional exploration context, kaolinite would be a targeted mineral as its presence could be indicative of a nearby (less than a few hundreds of meter) deposit. In a production environment, however, the presence of large amounts of kaolinite could indicate that the mineralized target was missed. Prehnite is ubiquitous in hand samples collected from 4 km to 8 km away from the deposits, and its abundance decreased dramatically in samples near (< 4 km) and within the deposits. Prehnite is the most distant spectrally detectable alteration mineral at HVC. Because of its distinctive spectral response (no other common mineral shows an absorption near 1477 nm), it is easily identified in mineral mixtures, and may therefore serve as an effective distal indicator of mineralization on regional scales.

4.5.2 Spectral alteration score and implications for the mining industry

In addition to sulfides, minerals generally associated to mineralization at the Valley, Lornex and Highmont deposits include quartz, coarse-grained white mica, and kaolinite. In the Bethlehem deposit, tourmaline and abundant epidote are also common alteration minerals. Prehnite and minor epidote occur in the distal alteration halo in all cases and are not expected to occur within mineralized samples. Together, these seven key minerals produce a spectral alteration score that is valid across the entirety of the Guichon Creek batholith. Several other minerals may also be either positively or negatively associated with mineralization and may be used to improve the spectral alteration score developed in this study. For example, gypsum occurs exclusively within the Valley and Lornex deposits (Figure 4-20c), and its presence could indicate potentially mineralized samples. Amphibole, on the other hand, is a primary magmatic mineral and is generally chloritized in altered zones (Figure 4-15 e and f). Its presence would therefore indicate unaltered samples (i.e., a value of one could be subtracted to the spectral alteration score for amphibole bearing samples).

Although additional minerals could increase the accuracy of the spectral alteration score, the intended goal of the metric presented here is to serve as a proof-of-concept that could easily be implemented by the mining industry. This metric could be employed, for example, as an exploration tool during regional-scale sampling (Figure 4-20b), or could potentially be utilized for resource characterization as part of a suite of measurements for ore-sorting (e.g., with a hyperspectral camera installed atop a conveyor belt transporting bulk-ore, or integrated within existing ore-sorting equipment). This would require the metric to be computationally inexpensive, and to perform well on the entirety of the Guichon Creek batholith rock samples (rather than to be limited to a sample subset). For these reasons, a minimal set of minerals or spectral parameters are preferred over a complex set of spectral metrics. The oft-used position of the 2200 nm absorption feature (representing white mica chemistry) was not included in the current spectral alteration score, as it would require interpolation of the spectral data, which would be computationally intensive and may be difficult to implement (as detailed in Lypaczewski et al. 2018). Rather, the proposed metric relies exclusively on the presence or absence of a set of key minerals that occur within altered zone, all of which can potentially be identified by computationally simple methods such as band ratios. Importantly, the metric also does not rely on complex, statistically derived parameters. If needed, the metric can therefore easily be modified with geological knowledge available to mine geologists, (e.g., in specific portions of a given mine, another set of minerals may perform better than those presented here).

With these considerations in mind, the spectral alteration score performs adequately on the entirety of the sample suite. The global metric, utilizing all minerals listed in Table 2, achieves a detection of 88% of the mineralized samples, and 81% of the barren samples, over a total of 755 slabs (regardless of lithofacies). The misidentified mineralized samples generally contain low Cu abundances, near the 1000 ppm Cu cut-off grade. Of a total of 72 mineralized samples, 63 were correctly identified, and the nine were misidentified as unmineralized. Of those, seven contained between 1045 and 1827 ppm Cu, below the mineral reserve grade of 0.3% Cu (Teck Resources Limited, 2019), and two had 2191 and 2651 ppm Cu, still below the mineral reserve grade at HVC. Generally, samples with a higher spectral alteration score contain greater Cu concentrations (Figure 4-17). However, because mineralization may be concentrated in a few veins and alteration selvages are generally more extensive, it is not possible to determine the exact Cu concentration for any given sample based on alteration mineralogy alone (e.g., Bethsaida rocks with a score of five can have Cu contents of between 300 and >10000 ppm).

4.5.3 Quartz veining and alteration in continuous drill core

In the continuous drill core presented here, the spectrally estimated abundance of quartz (*Figure* 4-18g; and associated sulfides in *Figure* 4-18h) was found to be closely correlated to assayed Cu grades. However, the presence of quartz alone is not necessarily an indicator of mineralization, as quartz veins are known to be barren in the central portions of the deposit (the barren core). It is therefore likely that the correlation between spectrally detected quartz abundance and mineralization is valid only in certain sections of the open pits, but not across the entirety of the deposit. Still, as the barren core was not sampled in this study, it may yet present spectrally detectable differences to quartz from mineralized zones. Barren quartz may, for example, lack the associated spectrally detectable sulfides, could have fewer fluid inclusions, resulting in weaker water-related absorptions, or could be associated to minerals that are not closely associated to mineralization (e.g., prehnite).

The spectral alteration score, taking into account several minerals indicative of alteration, is a generally more inclusive estimator of mineralization across all deposits in the HVC district, and accurately identifies alteration and potential mineralization both in hand samples and in drill core. Although in the particular drill core section shown in this study, the spectral alteration score appears to be mainly dependent on the presence of coarse-grained white mica, the other minerals are nonetheless required to obtain a reliable metric over all samples in the district.

4.5.4 Interference Al-phyllosilicates in estimating white mica chemistry

Although high-resolution hyperspectral imaging allows identification of mineralogy on small areas (e.g., 1 mm^2), which minimizes spectral mixing often encountered in point measurements (covering, for example, 1 cm^2), certain minerals occur as intimate mixtures (on micron-scales) and, when presenting overlapping absorptions, pose a challenge in their analysis. A commonly occurring mixture that is spectrally difficult to investigate involves the Al-bearing phyllosilicates muscovite (i.e., white mica with an interlayer occupancy ≈ 1 apfu), illite (i.e., with an interlayer occupancy <0.85 apfu), smectites (i.e., montmorillonite), and kaolin group minerals. In this study, spectra of background mineralogy in unaltered samples nearly always shows an absorption near or below 2195 nm, indicating Al-rich white mica, but often show variably developed 1460 nm and 1900 nm absorptions, which may respectively indicate coexisting montmorillonite and/or illite. As the 1460 nm absorption of montmorillonite is relatively weak and overlaps with the 1430 nm absorption of free water (e.g., as fluid inclusions in coexisting quartz grains), montmorillonite can only be reliably detected when present in relatively large abundances. For this reason, the background, unaltered Al-phyllosilicate mineralogy is referred to as fine-grained white mica, being a possible mixture of Al-rich (low wavelength, ≈2195 nm) muscovite, illite, and/or montmorillonite.

The presence of kaolinite is also problematic for the estimation of white mica (muscovite) mineral chemistry, as the 2207 nm absorption of kaolinite fully overlaps with, and overshadows, the Al_2-OH absorption of white mica near 2200 nm. Kaolinite can be reliably detected from the presence of a unique ≈ 2160 nm absorption, but, as with the 1460 nm absorption of montmorillonite, it is relatively weak and may be difficult to detect when kaolinite occurs in small abundances. The 2207 nm absorption of kaolinite is much stronger, and where coexisting with white mica, may influence the overall estimated position Al_2-OH near 2200 nm, even when kaolinite is present in such small abundance that it cannot reliably be detected from the 2160 nm absorption. As an example, *Figure 4-22* illustrates kaolinite interference on the 2200 nm absorption position near a kaolinite-rich vein and vein selvage. Background white mica shows absorptions near 2195 nm, while pure kaolinite shows an absorption feature at 2207 nm. The presence of kaolinite, as detected from the 2160 nm absorption, is presented in *Figure 4-22*c, and is masked in *Figure 4-22*d. While a large portion of interfering kaolinite was masked, at larger distances in the vein halo it is likely that trace amounts of kaolinite influence the position of the 2200 nm absorption. In the detailed spectra shown in *Figure 4-22*e, a slight inflection occurs near 2160 nm in spectrum 2, likely indicating the presence of trace amounts of kaolinite, but too weak to be reliably detected.

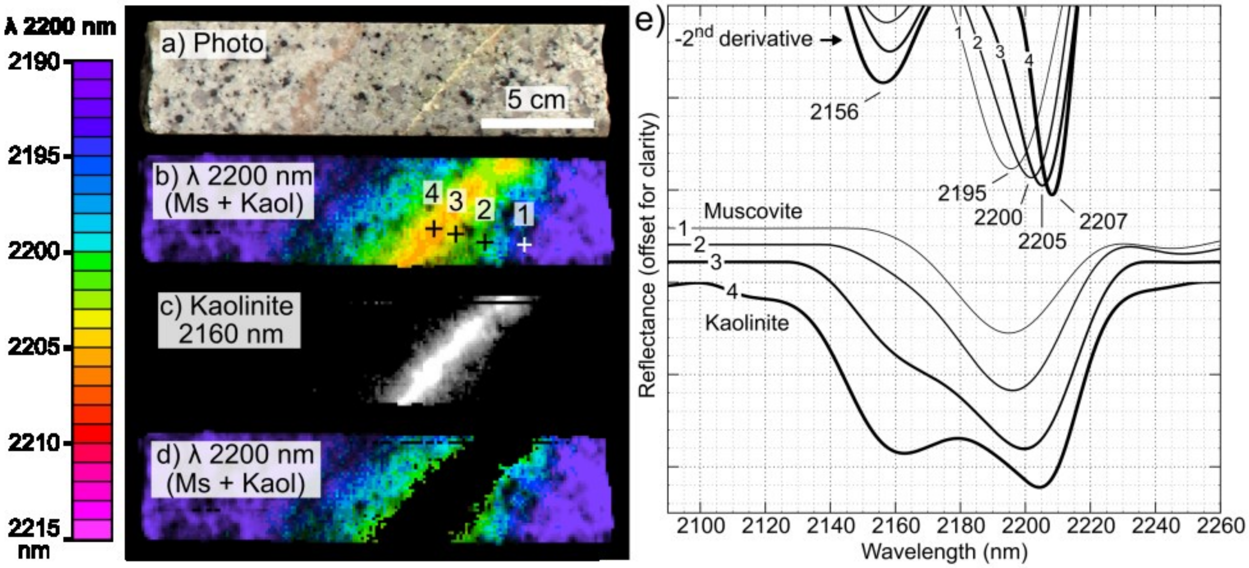

Figure 4-22 *Drill core interval from core presented in Figure 4-18. a) Core photograph. b) Hyperspectral imagery processed to display the position of the 2200 nm absorption feature, not filtered by mineralogy and including interference from kaolinite (c) Presence of kaolinite, derived from the presence of an absorption near 2160 nm. d) Image presented in a), with masking of the pixels showing the 2160 nm absorption. e) Detail of continuum removed and second derivative spectra extracted from the pixels highlighted in b).*

If spectral measurements are averaged on the scale of a sample (either from analysis on pulps, measurements performed using point spectrometers, or from low-spatial resolution, airborne imagery), because of the interference of kaolinite, the commonly investigated 2200 nm white mica absorption position must be carefully interpreted. The apparent 2200 nm absorption position may reflect white mica chemistry, but at HVC would mostly be dependent on the amount of interfering kaolinite, as shown in *Figure 4-21*. Samples from the core of the deposits (which may have kaolinite present) show an absorption near 2207 nm, while distal samples (with no kaolinite) present an average absorption near 2195 nm. White mica chemistry, from high resolutions hyperspectral imagery, is muscovitic (low-Al, 2195 nm) within the deposit (*Figure 4-14*d), but may sit within a kaolinite-rich matrix (*Figure 4-14*b). Nonetheless, a detectable shift in the apparent 2200 nm absorption may prove to be an effective tool to vector towards mineralization in regional exploration campaigns, whether from real changes in muscovite composition or from interference from kaolinite as either could be indicative of hydrothermal alteration.

4.6 Conclusions

Shortwave infrared hyperspectral imaging was shown to be an effective method to characterize complex, fine-grained mineralogy in the Highland Valley porphyry district. Over twelve minerals can be spectrally identified and quantified, and physical parameters, such as white mica grain size can be spectrally estimated. At the Valley, Lornex and Highmont deposits, in addition to sulfides, quartz, and kaolinite, the most conspicuous change related to mineralization is the presence of coarse-grained white mica (> 1mm) that is muscovitic (2195 nm) in composition. Prehnite is the most distant spectrally detectable alteration minerals (defining an annular alteration zone, up to 8 km from the deposits), and often presents selvages of coarse-grained phengitic (2215 nm) white mica. At the Bethlehem deposit, and in individual showings at the periphery of the batholith, tourmaline and large amounts of epidote form with sulfide mineralization. Collectively, the presence of these seven minerals are used to define a spectral alteration score that performs well in the entirety of the Guichon Creek batholith and can discriminate between mineralized and unmineralized samples. As the alteration score exclusively relies on the presence or absence of these key minerals, which can be identified by computationally simple methods, it could serve to enhance core logging methodologies, as an effective proxy for geometallurgical performance, or as a metric that could be employed for resource characterization to facilitate ore sorting. On regional scales, as acquiring hyperspectral data is rapid and requires little to no sample preparation, SWIR spectroscopy could serve as a rapid regional exploration tool in prospective environment.

References

Agus, A.J.L., 2011. Mapping white mica in milled porphyry copper pebbles using hyperspectral imagery: an exploratory study: M.Sc. thesis, Enschede, University of Twente, Faculty of Geo-Information and Earth Observation (ITC), 57 p.

Alva-Jimenez, T.R., 2011, Variation in hydrothermal muscovite and chlorite composition in the Highland Valley porphyry Cu-Mo district, British Columbia, Canada: M.Sc. thesis, Vancouver, University of British Columbia, 233 p.

Bierwirth, P.N., 2008. Laboratory and imaging spectroscopy of tourmaline – A tool for mineral exploration. *14th Australasian Remote Sensing & Photogrammetry Conference.* Darwin, Australia, September 27 - October 4, 2008.

Bishop, J.L., Lane, M.D., Dyar, M.D. and Brown, A.J., 2008. Reflectance and emission spectroscopy study of four groups of phyllosilicates: smectites, kaolinite-serpentines, chlorites and micas. Clay minerals, 43(1), pp.35-54.

Byrne, K., 2019. Diagnostic Features of the Rocks and Minerals Peripheral to the Highland Valley Copper District, British Columbia, Canada: Implications for the genesis of porphyry Cu systems and their footprints: Ph.D. thesis, Edmonton, University of Alberta, 211 p.

Byrne, K., Lesage, G., Gleeson, S.A. and Lee, R.G., 2017. Large-Scale Sodic-Calcic Alteration Around Porphyry Copper Systems: Examples from the Highland Valley Copper District, Guichon Batholith, South-Central British Columbia. Geoscience BC Summary of Activities, pp. 2017-1.

Byrne, K., Lesage, G., Morris, W.A., Enkin, R.J., Gleeson, S.A. and Lee, R.G., 2019. Variability of outcrop magnetic susceptibility and its relationship to the porphyry Cu centers in the Highland Valley Copper district. Ore Geology Reviews, 107, pp. 201-217.

Byrne, K., Stock, E., Ryan, J., Johnson, C., Nisenson, J., Alva-Jimenez, T., Lapointe, M., Stewart, H., Grubisa, G. and Sykora, S., 2013. Porphyry Cu-(Mo) deposits in the Highland Valley district, south central British Columbia. Porphyry systems of central and southern British Columbia: Tour of central British Columbia porphyry deposits from Prince George to Princeton. Society of Economic Geologists, Field Trip Guidebook, Series, 43, pp.99-116.

Clark, R.N., 1981. The spectral reflectance of water-mineral mixtures at low temperatures. Journal of Geophysical Research: Solid Earth, 86(B4), pp. 3074-3086.

Clark, R.N., King, T.V., Klejwa, M., Swayze, G.A. and Vergo, N., 1990. High spectral resolution reflectance spectroscopy of minerals. Journal of Geophysical Research: Solid Earth, 95(B8), pp.12653-12680.

Cudahy, T.J., Wilson, J., Hewson, R., Linton, P., Harris, P., Sears, M., Okada, K. and Hackwell, J.A., 2001, July. Mapping porphyry-skarn alteration at Yerington, Nevada, using airborne hyperspectral VNIR-SWIR-TIR imaging data. In IGARSS 2001. Scanning the Present and Resolving the Future. Proceedings. IEEE 2001 International Geoscience and Remote Sensing Symposium (Cat. No. 01CH37217) (Vol. 2, pp. 631-633). IEEE.

Cudahy, T., 2016. Mineral mapping for exploration: An Australian journey of evolving spectral sensing technologies and industry collaboration. Geosciences, 6(4), p.52.

Dalm, M., Buxton, M.W.N. and van Ruitenbeek, F.J.A., 2017. Discriminating ore and waste in a porphyry copper deposit using short-wavelength infrared (SWIR) hyperspectral imagery. Minerals engineering, 105, pp.10-18.

D'Angelo, M., 2016, Geochemistry, petrography and mineral chemistry of the Guichon Creek and Nicola batholiths, southcentral British Columbia Michael: M.Sc. Thesis, Lakehead University, 435 p.

D'Angelo, M., Miguel, A., Hollings, P., Byrne, K., Piercey, S. and Creaser, R.A., 2017. Petrogenesis and magmatic evolution of the Guichon Creek batholith: Highland Valley porphyry Cu±(Mo) district, south-central British Columbia. Economic Geology, 112(8), pp.1857-1888.

Duke, E.F., 1994. Near infrared spectra of muscovite, Tschermak substitution, and metamorphic reaction progress: Implications for remote sensing. Geology, 22(7), pp.621-624.

Duke, E.F., Lewis, R.S., 2010. Near infrared spectra of white mica in the Belt Supergroup and implications for metamorphism. Am. Mineral. 95 (7), 908–920.

Entezari, I., Rivard, B., Geramian, M. and Lipsett, M.G., 2017. Predicting the abundance of clays and quartz in oil sands using hyperspectral measurements. International Journal of Applied Earth Observation and Geoinformation, 59, pp.1-8.

Graden, R., 2013, NI 43-101 Technical Report Teck Highland Valley Copper. Vancouver, BC, Canada. Teck Ressources Limited Inc.

Graham, G.E., Kokaly, R.F., Kelley, K.D., Hoefen, T.M., Johnson, M.R. and Hubbard, B.E., 2018. Application of imaging spectroscopy for mineral exploration in Alaska: A study over porphyry Cu deposits in the Eastern Alaska Range. Economic Geology, 113(2), pp.489-510.

Harraden, C.L., Mcnulty, B.A., Gregory, M.J. and Lang, J.R., 2013. Shortwave infrared spectral analysis of hydrothermal alteration associated with the Pebble porphyry copper-gold-molybdenum deposit, Iliamna, Alaska. Economic Geology, 108(3), pp.483-494.

Harrison, T.N., 2012. Experimental VNIR reflectance spectroscopy of gypsum dehydration: Investigating the gypsum to bassanite transition. American Mineralogist, 97(4), pp.598-609.

Hecker, C., van der Meijde, M. and van der Meer, F.D., 2010. Thermal infrared spectroscopy on feldspars—Successes, limitations and their implications for remote sensing. Earth-Science Reviews, 103(1-2), pp.60-70.

Hunt, G.R.,Salisbury, J.W., 1970. Visible and near-infrared spectra of minerals and rocks: I Silicate minerals. Modern Geology, 1, pp. 283-300

Hunt, G.R., 1977. Spectral signatures of particulate minerals in the visible and near infrared. Geophysics, 42(3), pp.501-513.

Kokaly, R.F., Clark, R.N., Swayze, G.A., Livo, K.E., Hoefen, T.M., Pearson, N.C., Wise, R.A., Benzel, W.M., Lowers, H.A., Driscoll, R.L. and Klein, A.J., 2017. *USGS spectral library version 7* (No. 1035). US Geological Survey.

Laukamp, C., Termin, K.A., Pejcic, B., Haest, M. and Cudahy, T., 2012. Vibrational spectroscopy of calcic amphiboles–applications for exploration and mining. European Journal of Mineralogy, 24(5), pp.863-878.

Lee, R.G., Byrne, K., Alfaro, M., D’Angelo, M., Hart, C.J., Hollings, P. and Gleeson, S.A., 2017. Assessing the zircon compositional evolution from the Guichon Creek Batholith and Highland Valley Copper deposit, south-central BC. In 14th Society for Geology Applied to Mineral Deposits Biennial meeting (pp. 1087-1090).

Lesage, G., Byrne, K., Lypaczewski, P., Lee, R.G., and Hart, C.J.R., 2016, Characterizing the district scale alteration surrounding a large porphyry Cu system: The footprint of Highland Valley Copper, British Columbia, in GAC-MAC Abstracts, June 1-3, 2016, v. 39, Whitehorse, Yukon, p. 52.

Lesage, G., Byrne, K., Morris, W.A., Enkin, R.J., Lee, R.G., Mir, R., and Hart, C.J.R., 2019, Interpreting regional 3D fault networks from integrated geological and geophysical data sets: An example from the Guichon Creek batholith, British Columbia. Journal of Structural Geology, v. 119, p. 93–106.

Lypaczewski, P. and Rivard, B., 2018. Estimating the Mg# and AlVI content of biotite and chlorite from shortwave infrared reflectance spectroscopy: Predictive equations and recommendations for their use. International Journal of Applied Earth Observation and Geoinformation, 68, pp.116-126.

Lypaczewski, P., Rivard, B., Gaillard, N., Perrouty, S., Piette-Lauzière, N., Bérubé, C.L. and Linnen, R.L., 2019. Using hyperspectral imaging to vector towards mineralization at the Canadian Malartic gold deposit, Québec, Canada. Ore Geology Reviews, 111, 102945.

McLeod, R.L., Gabell, A.R., Green, A.A., Gardavski, V., 1987. Chlorite infrared spectral data as proximity indicators of volcanogenic massive sulphide mineralization. Pac. Rim Congr. 87, 321–324.

McMillan, W.J. 1976, Geology and genesis of the Highland Valley ore deposits and the Guichon Creek batholith: in Sutherland Brown, A., ed., Porphyry Deposits of the Canadian Cordillera: Canadian Institute of Mining and Metallurgy, Special Volume 15, p. 85-104.

McMillan, W.J., 1985, Geology and ore deposits of the Highland Valley camp: in Sinclair A.J., ed., Mineral Deposits Division field guide and reference manual series, n. 1, Geological Association of Canada, 121 p.

McMillan, W.J., Anderson, R.G., Chen, R., and Chen, W., 2009, Geology and mineral occurrences (MINFILE), the Guichon Creek batholith and Highland Valley porphyry copper district, British Columbia: Open file 6079, Geological Survey of Canada, 2 p.

Neal, L.C., Wilkinson, J.J., Mason, P.J. and Chang, Z., 2018. Spectral characteristics of propylitic alteration minerals as a vectoring tool for porphyry copper deposits. Journal of Geochemical Exploration, 184, pp.179-198.

Post, J.L. and Noble, P.N., 1993. The near-infrared combination band frequencies of dioctahedral smectites, micas, and illites. Clays and clay minerals, 41(6), pp.639-644.

Roache, T.J., Walshe, J.L., Huntington, J.F., Quigley, M.A., Yang, K., Bil, B.W., Blake, K.L. and Hyvärinen, T., 2011. Epidote–clinozoisite as a hyperspectral tool in exploration for Archean gold. Australian Journal of Earth Sciences, 58(7), pp.813-822.

Seedorff, E., Dilles, J.H., Proffett, J.M., Einaudi, M.T., Zurcher, L., Stavast, W.J.A., Johnson, D.A., and Barton, M.D., 2005, Porphyry Deposits: Characteristics and Origin of Hypogene Features, in Hedenquist, J.W., Thompson, J.F.H., Goldfarb, R.J., and

Richards, J.P. eds., Economic Geology 100th Anniversary Volume, Society of Economic Geologists, p. 251–298.

Sillitoe, R.H., 1973. The tops and bottoms of porphyry copper deposits. Economic Geology, 68(6), pp.799-815.

Sillitoe, R.H., 2010. Porphyry copper systems. Economic geology, 105(1), pp.3-41.

Singer, D.A., Berger, V.I., and Moring, B.C., 2008, Porphyry copper deposits of the world: Database and grade and tonnage models: U.S. Geological Survey Open-File Report 2008−1155.

Taran, M.N., Lebedev, A.S. and Platonov, A.N., 1993. Optical absorption spectroscopy of synthetic tourmalines. Physics and Chemistry of Minerals, 20(3), pp.209-220.

Teck Ressources Limited Inc. (2019) Annual Information Form, Vancouver, BC, Canada. Teck Ressources Limited Inc.

Wang, R., Cudahy, T., Laukamp, C., Walshe, J.L., Bath, A., Mei, Y., Young, C., Roache, T.J., Jenkins, A., Roberts, M., Barker, A., 2017. White mica as a hyperspectral tool in exploration for the Sunrise Dam and Kanowna Belle Gold deposits Western Australia. Econ. Geol. 112 (5), 1153–1176.

Whalen, J.B., Davis, W.J. and Anderson, R.A., 2017. Temporal and geochemical evolution of the Guichon Creek Batholith and Highland Valley porphyry copper district, British Columbia: Implications for generation and tectonic setting of porphyry systems; Geological Survey of Canada, Open File 8334.

White, A.J., Laukamp, C., Stokes, M.A., Legras, M. and Pejcic, B., 2017. Vibrational spectroscopy of epidote, pumpellyite and prehnite applied to low-grade regional metabasites. Geochemistry: Exploration, Environment, Analysis, 17(4), pp.315-333.

Chapter 5 - Conclusions

5.1 Summary

In this thesis, results of both fundamental and applied hyperspectral research were presented. Fundamental research investigated the shortwave infrared reflectance spectroscopy of biotite, chlorite, and to a limited extent, of white mica. Novel correlations to mineral chemistry or physical parameters were reported for all minerals. Applied research focussed on the Canadian Malartic disseminated gold deposit and the Highland Valley Copper porphyry district. Few studies to date have made use of high-resolution hyperspectral imaging at these types of deposits, and new insights as to the scale of alteration were presented on sample-scales (cm-sizes, vein selvages), deposit-scales (meter-sizes, continuous drill core imagery), and regional-scales (km-sizes, deposit halo). The main findings of this thesis are presented below.

5.1.1 Spectroscopy of biotite and chlorite

Shortwave infrared reflectance spectra of biotite and chlorite were investigated to establish quantitative relationships between spectral metrics and mineral chemistry. Regression equations between absorption position and Mg# were presented (e.g., the 2250 nm Al(Mg,Fe)-OH feature), and allowed the estimation of Mg# to ±3 Mg# and ±5 Mg# for biotite and chlorite, respectively. Correlations between absorption feature depths and Al^{VI} content were also presented, and allowed the estimation of Al^{VI} to ± 0.044 Al^{VI} (11 O) and ± 0.09 Al^{VI} (14 O), for biotite and chlorite, respectively. Importantly, as both minerals have absorptions at common positions (1400, 2250, 2330 nm), and spectral interference may occur in mineral mixtures, strategies for distinguishing these two spectrally similar minerals were presented. Because absorptions of chlorite are offset to 1–15 nm higher wavelengths relative to those of biotite (for an equivalent Mg#), correctly identifying the dominant mineral is critical to derive correct compositional data.

5.1.2 Canadian Malartic

High-resolution hyperspectral imagery has been acquired for a large number of samples (>500) and drill core (>2000 m) at the Canadian Malartic gold deposit, to investigate the practical use of these instruments in an industrial setting. Reflectance spectroscopy was shown to be an effective method to characterize mineralogy and to derive mineral chemistry, including in samples containing complex mineral mixtures of biotite, chlorite, and white mica. The Mg# of biotite could be estimated from the 2250 nm absorption to ± 1.7 Mg# for relatively chlorite-free samples (an improvement over the previously defined ± 3 Mg#), and additional regression equations were presented between the Al^{VI} content of white mica and the position of the 2200 nm feature. It was shown that Al^{VI} content could be estimated to ± 0.022 apfu, and regressions matched equations previously established using pure samples (crystal standards). It was therefore shown that mineral mixtures did not have a significant impact on the estimation of mineral chemistry in a practical setting.

High-resolution hyperspectral imagery was used to visualize and discriminate changes in mineralogy and mineral chemistry due to metamorphism and hydrothermal alteration. Unaltered metasedimentary rocks contained metamorphic white mica with Al^{VI} contents varying between 1.90 and 1.75 apfu (corresponding to absorption positions between 2195 and 2203 nm), depending on metamorphic grade. Hydrothermal alteration was characterized by white mica that becomes progressively more phengitic with increasing alteration intensity, with Al^{VI} contents ranging from 1.70 to 1.50 apfu (2204 to 2212 nm). Importantly, it was shown that phengitic white mica alteration extends from meters to tens of meters away from major mineralized zones, and can be used as a vector towards mineralization in an exploration setting, while on smaller scales, mica chemistry is correlated to Au content, and can be used to discriminate between unmineralized (<0.3 g/t Au, 2195-2204 nm), weakly mineralized (>0.3 g/t Au, 2205-2208 nm), and highly mineralized (> 1.0 g/t Au, >2208 nm) samples. This simple metric could directly be applied for ore sorting in a production environment. The Mg# (molar Mg/[Mg+Fe]) of biotite, on the other hand, was shown to be unaffected by metamorphic grade, and was consistently found to be between Mg# 55-60 (2251-2250 nm) in unaltered samples. In mineralized samples, biotite was Mg-rich (Mg# >65, <2249 nm), but rapidly graded into background compositions outside of the ore zones. Biotite chemistry can therefore be used to highlight the presence of the most intensely altered (and potentially mineralized) drill core intervals. Based on knowledge gained from sample imagery, over 1500 SWIR point measurements were acquired in a 50 km by 15 km area around the deposit, and were used to delineate metamorphic isograds on regional scales, and to delineate a large 12 km by 3 km hydrothermal alteration halo around the deposit. Finally, longwave infrared hyperspectral data was acquired for drill core to estimate the abundance of silicification. The strength of the 9200 nm peak was generally in good agreement with the silicification abundance estimated from core logging.

5.1.3 Highland Valley Copper

At the Highland Valley Copper porphyry district, high-resolution SWIR hyperspectral imaging was shown to be an effective method to characterize texturally complex, fine-grained mineralogy occurring in veins, veinlets, and vein selvages. Twelve minerals were spectrally detected and quantified. A novel metric was developed to estimate white mica grain size, and the most conspicuous change related to hydrothermal alteration was the presence of coarse-grained white mica (> 1mm) that is muscovitic (2195 nm) in composition. Prehnite, detected from its distinctive 1477 nm absorption, was shown to abound in the distal alteration halo, and defined an annular alteration zone up to 8 km from the deposits. The presence of seven key minerals was used to define a spectral alteration score that can discriminate between mineralized and unmineralized samples, and could therefore serve as an effective ore sorting metric.

5.1.4 Potential uses for the mining industry

The results presented in this study demonstrated that SWIR spectroscopy could serve to facilitate regional exploration in various geological environments. The Cadillac-Larder Lake Deformation zone, host to numerous gold deposits in Quebec, extends for nearly 200 km west of Canadian Malartic. Performing SWIR measurements and mapping mineral chemistry along this zone may enable the detection of other, potentially unknown mineralized areas. Importantly, as both highly phengitic (long wavelength, e.g., Canadian Malartic) and highly muscovitic (low wavelength, e.g., the Sunrise Dam gold deposit, Wang et al. (2017)) can be associated to mineralization, it is the gradient in chemistry in a region, rather than the presence of a particular mineral chemistry, that will allow vectoring towards mineralization on regional scales. Under glacial cover, where bedrock is inaccessible, using hyperspectral imaging to analyze till samples may reveal dispersion patterns that could also be used to vector to mineralization (e.g., Taylor et al., 2018). On smaller scales, within a known deposit, the use of hyperspectral imaging to scan drill core may enhance core logging accuracy, by allowing consistent characterization across the entirety of the deposit. In such cases, it may improve the delineation of mineralized intervals, for example by proxy of biotite chemistry, and could potentially reduce assaying costs by limiting sampling to highly altered intervals. Similar metrics (low wavelength biotite and/or long wavelength white mica) have the potential to be used for ore characterization as part of an ore sorting process, potentially reducing mining costs.

5.2 Avenues for future research

The spectral response of biotite and chlorite were characterized in Chapter 2, where regressions linking absorption position or strength to Al^{VI} and Mg# were provided for most absorptions. For certain samples with extreme mineral chemistries, however, outliers were present in several regression lines, the cause of which remains undetermined.

The regression between the Mg# of biotite and its 2250 nm absorption (Figure 2-3b) is only valid for samples with Al^{VI} contents >0.2 apfu, as absorptions are shifted to longer wavelengths with decreasing Al^{VI} content. Additionally, no samples above 0.31 Al^{VI} apfu were investigated. A more comprehensive study of biotite samples with variable Al^{VI} contents (to siderophyllite and eastonite end-members, at 1.0 Al^{VI} apfu) may reveal a predictable shift with Al^{VI} content.

In chlorite, the position of the 2250 nm absorption was also shifted to lower than expected values with decreasing Al^{VI} contents (Figure 2-5e), and two absorptions appeared to be superposed near 2330-2350 nm (Figure 2-4d, 2-5g) for high-Al samples. These could not be discriminated at the current spectral resolution. A higher resolution instrument may therefore reveal details in spectral features that are not detectable using the current equipment. In addition, the position of the 2000 nm absorption was shifted to lower than expected wavelengths for some, but not all, high-Mg# samples (Figure 2-5 c). The effects of variable Fe^{2+}/Fe^{3+} ratios, or the presence of trace elements could potentially explain this shift, but were not investigated in this thesis.

Chapter 3 characterized samples from the Canadian Malartic gold deposit mainly using SWIR hyperspectral imaging. Carbonates are known to occur as alteration minerals, and larger carbonate veins were detected in some samples. However, when present in low abundances, the only easily detectable absorption feature of carbonates (near 2330 nm) fully overlaps with absorptions of biotite, chlorite, and white mica, which are abundant in all samples. Carbonates have strong absorptions between 3000-4000 nm. The use of midwave infrared (MWIR, 3000-5000 nm) hyperspectral imaging may therefore reveal distal alteration patterns that could not be detected in the SWIR. The Highland Valley Copper deposits in Chapter 4 were investigated using the same SWIR instrument, and information on carbonates is similarly lacking.

For the Highland Valley Copper deposits, a generalized spectral alteration score was developed using the presence of seven key minerals, and performed well in the entirety of the Guichon Creek. In certain areas, however, a better correlation to mineralization was seen from the relative abundance of (sulfide-bearing) quartz (Figure 4-8g). In other areas, quartz is known to be barren (e.g., the silicic re-entrant) and lacks sulfides. This barren quartz was not sampled, and it is not known whether spectral metrics may be able to distinguish between barren and ore-bearing quartz. As only a few hundred meters of drill core were analyzed, a more extensive hyperspectral study (e.g., several thousand meters) may be appropriate.

Literature cited

Agus, A.J.L., 2011. Mapping white mica in milled porphyry copper pebbles using hyperspectral imagery: an exploratory study: M.Sc. thesis, Enschede, University of Twente, Faculty of Geo-Information and Earth Observation (ITC), 57 p.

Alva-Jimenez, T.R., 2011, Variation in hydrothermal muscovite and chlorite composition in the Highland Valley porphyry Cu-Mo district, British Columbia, Canada: M.Sc. thesis, Vancouver, University of British Columbia, 233 p.

Armstrong, J. T. 1995. Citzaf-a package of correction programs for the quantitative Electron Microbeam X-Ray-Analysis of thick polished materials, thin-films, and particles. Microbeam Analysis, 4(3), 177-200.

Arne, D., House, E., Pontual, S. and Huntington, J., 2016. Hyperspectral interpretation of selected drill cores from orogenic gold deposits in central Victoria, Australia. Australian Journal of Earth Sciences, 63(8), pp.1003-1025.

ASD Inc. (2010) FieldSpec® 3 User Manual, Boulder, CO, USA. ASD Inc.

Ayer, J.A., et al., 2005. Overview of results from the greenstone architecture project: discover Abitibi initiative. Ontario Geol. Surv. Open File Rep. 6154, 146.

Bailey, S. W. 1986. Re-evaluation of ordering and local charge-balance in Ia chlorite. The Canadian Mineralogist, 24(4), 649-654.

Beran, A. 2002. Infrared spectroscopy of micas. Reviews in Mineralogy and Geochemistry, 46(1), 351-369.

Bérubé, C.L., Olivo, G.R., Chouteau, M., Perrouty, S., Shamsipour, P., Enkin, R.J., Morris, W.A., Feltrin, L. and Thiémonge, R., 2018. Predicting rock type and detecting hydrothermal alteration using machine learning and petrophysical properties of the Canadian Malartic ore and host rocks, Pontiac Subprovince, Québec, Canada. Ore Geology Reviews, 96, pp.130-145.

Besson, G., & Drits, V. A. 1997a. Refined relationships between chemical composition of dioctahedral fine-grained mica minerals and their infrared spectra within the OH stretching region. Part I: Identification of the OH stretching bands. Clays and Clay Minerals, 45(2), 158-169.

Besson, G., & Drits, V. A. 1997b. Refined relationships between chemical composition of dioctahedral fine-grained micaceous minerals and their infrared spectra within the OH stretching region. Part II: The main factors affecting OH vibrations and quantitative analysis. Clays and Clay Minerals, 45(2), 170-183.

Biel, C., Subías, I., Acevedo, R. D., Yusta, I., & Velasco, F. 2012. Mineralogical, IR-spectral and geochemical monitoring of hydrothermal alteration in a deformed and metamorphosed Jurassic VMS deposit at Arroyo Rojo, Tierra del Fuego, Argentina. Journal of South American Earth Sciences, 35, 62-73.

Bierwirth, P., Huston, D. and Blewett, R., 2002. Hyperspectral mapping of mineral assemblages associated with gold mineralization in the Central Pilbara, Western Australia. *Economic Geology*, *97*(4), pp.819-826.

Bierwirth, P.N., 2008. Laboratory and imaging spectroscopy of tourmaline – A tool for mineral exploration. 14th Australasian Remote Sensing & Photogrammetry Conference. Darwin, Australia, September 27 - October 4, 2008.

Bishop, J.L., Lane, M.D., Dyar, M.D. and Brown, A.J., 2008. Reflectance and emission spectroscopy study of four groups of phyllosilicates: smectites, kaolinite-serpentines, chlorites and micas. Clay minerals, 43(1), pp.35-54.

Byrne, K., 2019. Diagnostic Features of the Rocks and Minerals Peripheral to the Highland Valley Copper District, British Columbia, Canada: Implications for the genesis of porphyry Cu systems and their footprints: Ph.D. thesis, Edmonton, University of Alberta, 211 p.

Byrne, K., Lesage, G., Gleeson, S.A. and Lee, R.G., 2016. Large-Scale Sodic-Calcic Alteration Around Porphyry Copper Systems: Examples from the Highland Valley Copper District, Guichon Batholith, South-Central British Columbia. Geoscience BC Summary of Activities, pp. 2017-1.

Byrne, K., Lesage, G., Morris, W.A., Enkin, R.J., Gleeson, S.A. and Lee, R.G., 2019. Variability of outcrop magnetic susceptibility and its relationship to the porphyry Cu centers in the Highland Valley Copper district. Ore Geology Reviews, 107, pp. 201-217.

Byrne, K., Stock, E., Ryan, J., Johnson, C., Nisenson, J., Alva-Jimenez, T., Lapointe, M., Stewart, H., Grubisa, G. and Sykora, S., 2013. Porphyry Cu-(Mo) deposits in the Highland Valley district, south central British Columbia. Porphyry systems of central and southern British Columbia: Tour of central British Columbia porphyry deposits from Prince George to Princeton. Society of Economic Geologists, Field Trip Guidebook, Series, 43, pp.99-116.

Chang, Z. and Yang, Z., 2012. Evaluation of inter-instrument variations among short wavelength infrared (SWIR) devices. Economic Geology, 107(7), pp.1479-1488.

Clark, R. N., 1981. The spectral reflectance of water-mineral mixtures at low temperatures. Journal of Geophysical Research: Solid Earth, 86(B4), pp. 3074-3086.

Clark, R. N., and Roush, T. L. 1984. Reflectance spectroscopy: Quantitative analysis techniques for remote sensing applications. Journal of Geophysical Research: Solid Earth, 89(B7), 6329-6340.

Clark, R. N., King, T.V., Klejwa, M., Swayze, G.A. and Vergo, N., 1990. High spectral resolution reflectance spectroscopy of minerals. Journal of Geophysical Research: Solid Earth, 95(B8), pp.12653-12680.

Clark, R.N., Swayze, G.A., Gallagher, A., King, T.V.V and Calvin, W. M. 1993. The U. S. Geological Survey, Digital Spectral Library: Version 1: 0.2 to 3.0 m, U.S. Geological Survey, Open File Report 93-592.

Corfu, F., Jackson, S.L., Sutcliffe, R.H., 1991. U-Pb ages and tectonic significance of late Archean alkalic magmatism and nonmarine sedimentation: timiskaming Group, southern Abitibi belt, Ontario. Can. J. Earth Sci. 28 (4), 489–503.

Cudahy, T.J., Okada, K. and Brauhart, C., 2000, November. Targeting VMS-style Zn mineralisation at Panorama, Australia, using airborne hyperspectral VNIR-SWIR HyMap data. In ERIM proceedings of the 14th international conference on applied geologic remote sensing (pp. 395-402).

Cudahy, T., 2016. Mineral mapping for exploration: An Australian journey of evolving spectral sensing technologies and industry collaboration. Geosciences, 6(4):52.

Cudahy, T.J., Wilson, J., Hewson, R., Linton, P., Harris, P., Sears, M., Okada, K. and Hackwell, J.A., 2001, July. Mapping porphyry-skarn alteration at Yerington, Nevada, using airborne hyperspectral VNIR-SWIR-TIR imaging data. In IGARSS 2001. Scanning the Present and Resolving the Future. Proceedings. IEEE 2001 International Geoscience and Remote Sensing Symposium (Vol. 2, pp. 631-633). IEEE.

D'Angelo, M., 2016, Geochemistry, petrography and mineral chemistry of the Guichon Creek and Nicola batholiths, southcentral British Columbia Michael: M.Sc. Thesis, Lakehead University, 435 p.

D'Angelo, M., Miguel, A., Hollings, P., Byrne, K., Piercey, S. and Creaser, R.A., 2017. Petrogenesis and magmatic evolution of the Guichon Creek batholith: Highland Valley porphyry Cu±(Mo) district, south-central British Columbia. Economic Geology, 112(8), pp.1857-1888.

Dalm, M., Buxton, M.W.N. and van Ruitenbeek, F.J.A., 2017. Discriminating ore and waste in a porphyry copper deposit using short-wavelength infrared (SWIR) hyperspectral imagery. Minerals engineering, 105, pp. 10-18.

Davis, D.W., 2002. U–Pb geochronology of Archean metasedimentary rocks in the Pontiac and Abitibi subprovinces, Quebec, constraints on timing, provenance and regional tectonics. Precambrian Research, 115(1-4), pp. 97-117.

De Souza, S., Dubé, B., McNicoll, V.J., Dupuis, C., Mercier-Langevin, P., Creaser, R.A., Kjarsgaard, I.M., 2015. Geology, hydrothermal alteration, and genesis of the worldclass Canadian Malartic stockwork-disseminated Archean gold deposit, Abitibi, Quebec. In: Dube, B., Mercier-Langevin, P. (Eds.), Targeted Geoscience Initiative 4: Contributions to the Understanding of Precambrian Lode Gold Deposits and Implications for Exploration. Geological Survey of Canada, pp. 113–126 Open File 7852.

De Souza, S., Dubé, B., McNicoll, V.J., Dupuis, C., Mercier-Langevin, P., Creaser, R.A., Kjarsgaard, I.M., 2016. Geology and hydrothermal alteration of the world-class Canadian Malartic gold deposit: genesis of an Archean stockwork-disseminated gold deposit in the Abitibi Greenstone Belt, Québec. Reviews in Economic Geology, 19, 29 p.

Deer, W. A., Howie, R. A., & Zussman, J. (Eds.). 2009. Rock Forming Minerals: Layered Silicates Excluding Micas and Clay Minerals, Volume 3B. Geological Society of London.

Duke, E.F. and Lewis, R.S., 2010. Near infrared spectra of white mica in the Belt Supergroup and implications for metamorphism. American Mineralogist, 95(7), pp.908-920.

Duke, E.F., 1994. Near infrared spectra of muscovite, Tschermak substitution, and metamorphic reaction progress: Implications for remote sensing. Geology, 22(7), pp.621-624.

Duke, E.F., Lewis, R.S., 2010. Near infrared spectra of white mica in the Belt Supergroup

Entezari, I., Rivard, B., Geramian, M. and Lipsett, M.G., 2017. Predicting the abundance of clays and quartz in oil sands using hyperspectral measurements. International Journal of Applied Earth Observation and Geoinformation, 59, pp.1-8.

Farmer, V. C. 1968.Infrared spectroscopy in clay mineral studies. Clay minerals, 7(4), 373-387.

Farmer, V.C. (Ed.). 1974. The Infra-Red Spectra of Minerals. Mineralogical Society, London.

Fleet, M. E., Deer, W. A., Howie, R. A., & Zussman, J. (Eds.). 2003. Rock-Forming Minerals: Micas, Volume 3A. Geological Society of London.

Gaillard, N., Williams-Jones, A.E., Clark, J.R., Lypaczewski, P., Salvi, S., Perrouty, S., Piette-Lauzière, N., Guilmette, C. and Linnen, R.L., 2018. Mica composition as a vector to gold mineralization: Deciphering hydrothermal and metamorphic effects in the Malartic district, Quebec. Ore Geology Reviews, 95, pp.789-820.

Graden, R., 2013, NI 43-101 Technical Report Teck Highland Valley Copper. Vancouver, BC, Canada. Teck Ressources Limited Inc.

Graham, G.E., Kokaly, R.F., Kelley, K.D., Hoefen, T.M., Johnson, M.R. and Hubbard, B.E., 2018. Application of imaging spectroscopy for mineral exploration in Alaska: A study over porphyry Cu deposits in the Eastern Alaska Range. Economic Geology, 113(2), pp. 489-510.

Guanter, L., Kaufmann, H., Segl, K., Foerster, S., Rogass, C., Chabrillat, S., Kuester, T., Hollstein, A., Rossner, G., Chlebek, C. and Straif, C., 2015. The EnMAP spaceborne imaging spectroscopy mission for earth observation. *Remote Sensing*, *7*(7), pp. 8830-8857.

Harraden, C.L., McNulty, B.A., Gregory, M.J., Lang, J.R., 2013. Shortwave infrared spectral analysis of hydrothermal alteration associated with the Pebble porphyry Copper-Gold-Molybdenum Deposit Iliamna, Alaska. Econ. Geol. 108 (3), pp. 483–494.

Harrison, T.N., 2012. Experimental VNIR reflectance spectroscopy of gypsum dehydration: Investigating the gypsum to bassanite transition. American Mineralogist, 97(4), pp. 598-609.

Hecker, C., van der Meijde, M. and van der Meer, F.D., 2010. Thermal infrared spectroscopy on feldspars—Successes, limitations and their implications for remote sensing. Earth-Science Reviews, 103(1-2), pp. 60-70.

Heiligmann, M., Williams-Jones, A.E. and Clark, J.R., 2008. The role of sulfate-sulfide-oxide-silicate equilibria in the metamorphism of hydrothermal alteration at the Hemlo gold deposit, Ontario. Economic Geology, 103(2), pp. 335-351.

Helt, K.M., Williams-Jones, A.E., Clark, J.R., Wing, B.A. and Wares, R.P., 2014. Constraints on the genesis of the Archean oxidized, intrusion-related Canadian Malartic gold deposit, Quebec, Canada. Economic Geology, 109(3), pp. 713-735.

Hunt, G. R. 1977. Spectral signatures of particulate minerals in the visible and near infrared. Geophysics, 42(3), 501-513.

Hunt, G.R., Salisbury, J.W., 1970. Visible and near-infrared spectra of minerals and rocks: I Silicate minerals. Modern Geology, 1, pp. 283-300

Institut de la statistique du Québec, 2019. Distribution of the number of metres drilled, total cost and cost per metre for core drilling, by expenditure category, Québec, 2006-2018, Gouvernement du Québec, accessed 26 September 2019 <http://www.stat.gouv.qc.ca/statistiques/mines/forage-carottier/forage-cat-depense_an.htm>

Jones E, Oliphant E, Peterson P, et al. SciPy: Open Source Scientific Tools for Python, 2001-, http://www.scipy.org/ [Online; accessed 2019-04-04]

Jones, S., Herrmann, W. and Gemmell, J.B., 2005. Short wavelength infrared spectral characteristics of the HW horizon: Implications for exploration in the Myra Falls volcanic-hosted massive sulfide camp, Vancouver Island, British Columbia, Canada. Economic Geology, 100(2), pp. 273-294.

King, T. V., & Clark, R. N. 1989. Spectral characteristics of chlorites and Mg-serpentines using high-resolution reflectance spectroscopy. Journal of Geophysical Research: Solid Earth, 94(B10), 13997-14008.

Kokaly, R.F., Clark, R.N., Swayze, G.A., Livo, K.E., Hoefen, T.M., Pearson, N.C., Wise, R.A., Benzel, W.M., Lowers, H.A., Driscoll, R.L. and Klein, A.J., 2017. USGS spectral library version 7 (No. 1035). US Geological Survey.

Laakso, K., Peter, J.M., Rivard, B. and White, H.P., 2016. Short-wave infrared spectral and geochemical characteristics of hydrothermal alteration at the Archean Izok Lake Zn-Cu-Pb-Ag volcanogenic massive sulfide deposit, Nunavut, Canada: Application in exploration target vectoring. Economic Geology, 111(5), pp. 1223-1239.

Laakso, K., Rivard, B., Peter, J.M., White, H.P., Maloley, M., Harris, J. and Rogge, D., 2015. Application of airborne, laboratory, and field hyperspectral methods to mineral exploration in the Canadian Arctic: recognition and characterization of volcanogenic massive sulfide-associated hydrothermal alteration in the Izok Lake deposit area, Nunavut, Canada. Economic Geology, 110(4), pp. 925-941.

Laukamp, C., Cudahy, T., Thomas, M., Jones, M., Cleverley, J.S. and Oliver, N.H.S., 2011. Hydrothermal mineral alteration patterns in the Mount Isa Inlier revealed by airborne hyperspectral data. Australian Journal of Earth Sciences, 58(8), pp. 917-936.

Laukamp, C., Termin, K.A., Pejcic, B., Haest, M. and Cudahy, T., 2012. Vibrational spectroscopy of calcic amphiboles–applications for exploration and mining. European Journal of Mineralogy, 24(5), pp. 863-878.

Lee, R. G., Byrne, K., D’Angelo, M., Hart, C. J. R., Hollings, P., Gleeson, S. A., and Alfaro, M., (submitted) Using zircon trace element composition to assess porphyry copper potential of the Guichon Creek batholith and Highland Valley Copper deposit, south-central British Columbia: Mineralium Deposita.

Lee, R.G., Byrne, K., Alfaro, M., D’Angelo, M., Hart, C.J., Hollings, P. and Gleeson, S.A., 2017. Assessing the zircon compositional evolution from the Guichon Creek Batholith and Highland Valley Copper deposit, south-central BC. In 14th Society for Geology Applied to Mineral Deposits Biennial meeting (pp. 1087-1090).

Lesage, G., Byrne, K., Lypaczewski, P., Lee, R.G., and Hart, C.J.R., 2016, Characterizing the district scale alteration surrounding a large porphyry Cu system: The footprint of Highland Valley Copper, British Columbia, in GAC-MAC Abstracts, June 1-3, 2016, v. 39, Whitehorse, Yukon, pp. 52.

Lesage, G., Byrne, K., Morris, W.A., Enkin, R.J., Lee, R.G., Mir, R., and Hart, C.J.R., 2019, Interpreting regional 3D fault networks from integrated geological and geophysical data sets: An example from the Guichon Creek batholith, British Columbia. Journal of Structural Geology, v. 119, pp. 93–106.

Lypaczewski, P. and Rivard, B., 2018. Estimating the Mg# and Al^{VI} content of biotite and chlorite from shortwave infrared reflectance spectroscopy: Predictive equations and recommendations for their use. International Journal of Applied Earth Observation and Geoinformation, 68, pp. 116-126.

Lypaczewski, P., Rivard, B., Gaillard, N., Perrouty, S., Piette-Lauzière, N., Bérubé, C.L. and Linnen, R.L., 2019. Using hyperspectral imaging to vector towards mineralization at the Canadian Malartic gold deposit, Québec, Canada. Ore Geology Reviews, 111, 102945.

MacLean, W. H., & Kranidiotis, P. 1987. Immobile elements as monitors of mass transfer in hydrothermal alteration; Phelps Dodge massive sulfide deposit, Matagami, Quebec. Economic Geology, 82(4), pp. 951-962.

Martínez-Alonso, S., Rustad, J. R., and Goetz, A. F. 2002. Ab initio quantum mechanical modeling of infrared vibrational frequencies of the OH group in dioctahedral phyllosilicates. Part II: Main physical factors governing the OH vibrations. American Mineralogist, 87(8-9), pp. 1224-1234.

Mathieu, M., Roy, R., Launeau, P., Cathelineau, M. and Quirt, D., 2017. Alteration mapping on drill cores using a HySpex SWIR-320m hyperspectral camera: Application to the exploration of an unconformity-related uranium deposit (Saskatchewan, Canada). Journal of Geochemical Exploration, 172, pp. 71-88.

Mauger, A. J., Ehrig, K., Kontonikas-Charos, A., Ciobanu, C. L., Cook, N. J., & Kamenetsky, V. S. (2016). Alteration at the Olympic Dam IOCG–U deposit: insights into distal to proximal feldspar and phyllosilicate chemistry from infrared reflectance spectroscopy. Australian Journal of Earth Sciences, 63(8), 959-972.

Mauger, A.J., Ehrig, K., Kontonikas-Charos, A., Ciobanu, C.L., Cook, N.J. and Kamenetsky, V.S., 2016. Alteration at the Olympic Dam IOCG–U deposit: insights into distal to proximal feldspar and phyllosilicate chemistry from infrared reflectance spectroscopy. Australian Journal of Earth Sciences, 63(8), pp. 959-972.

McLeod, R. L., Gabell, A. R., Green, A. A., & Gardavski, V. 1987. Chlorite infrared spectral data as proximity indicators of volcanogenic massive sulphide mineralization. In Pacific Rim Congress 87, Gold Coast, 1987, Proceedings (pp. 321-324).

McMillan, W.J. 1976, Geology and genesis of the Highland Valley ore deposits and the Guichon Creek batholith: in Sutherland Brown, A., ed., Porphyry Deposits of the Canadian Cordillera: Canadian Institute of Mining and Metallurgy, Special Volume 15, pp. 85-104.

McMillan, W.J., 1985, Geology and ore deposits of the Highland Valley camp: in Sinclair A.J., ed., Mineral Deposits Division field guide and reference manual series, n. 1, Geological Association of Canada, 121 p.

McMillan, W.J., Anderson, R.G., Chen, R., and Chen, W., 2009, Geology and mineral occurrences (MINFILE), the Guichon Creek batholith and Highland Valley porphyry copper district, British Columbia: Open file 6079, Geological Survey of Canada, 2 p.

Miyashiro, A. and Shido, F., 1985. Tschermak substitution in low-and middle-grade pelitic schists. Journal of Petrology, 26(2), pp.449-487.

Naleto, J.L.C., Perrotta, M.M., da Costa, F.G. and de Souza Filho, C.R., 2019. Point and imaging spectroscopy investigations on the Pedra Branca orogenic gold deposit, Troia Massif, Northeast Brazil: Implications for mineral exploration in amphibolite metamorphic-grade terrains. Ore Geology Reviews, 107, pp. 283-309.

Neal, L.C., Wilkinson, J.J., Mason, P.J. and Chang, Z., 2018. Spectral characteristics of propylitic alteration minerals as a vectoring tool for porphyry copper deposits. Journal of Geochemical Exploration, 184, pp. 179-198.

Oliphant, T.E., 2006. A guide to NumPy (Vol. 1, p. 85). USA: Trelgol Publishing.

Perrouty, S., Gaillard, N., Piette-Lauzière, N., Mir, R., Bardoux, M., Olivo, G.R., Linnen, R.L., Bérubé, C.L., Lypaczewski, P., Guilmette, C. and Feltrin, L., 2017. Structural setting for Canadian Malartic style of gold mineralization in the Pontiac Subprovince, south of the Cadillac Larder Lake Deformation Zone, Québec, Canada. Ore Geology Reviews, 84, pp. 185-201.

Perrouty, S., Linnen, R.L., Lesher, C.M., Olivo, G.R., Piercey, S.J., Gaillard, N., Clark, J.R. and Enkin, R.J., 2018. Expanding the size of multi-parameter metasomatic footprints in gold exploration: utilization of mafic dykes in the Canadian Malartic district, Québec, Canada. Mineralium Deposita, pp.1-26.

Piette-Lauzière, N., Guilmette, C., Bouvier, A., Perrouty, S., Pilote, P., Gaillard, N., Lypaczewski, P., Linnen, R.L. and Olivo, G.R., 2019. The timing of prograde metamorphism in the Pontiac Subprovince, Superior craton; implications for Archean geodynamics and gold mineralization. Precambrian Research, 320, pp.111-136.

Post, J. L., & Crawford, S. M. 2014. Uses of near-infared spectra for the identification of clay minerals. Applied Clay Science, 95, 383-387.

Post, J.L. and Noble, P.N., 1993. The near-infrared combination band frequencies of dioctahedral smectites, micas, and illites. Clays and clay minerals, 41(6), pp. 639-644.

Powell, W.G., Carmichael, D.M. and Hodgson, C.J., 1995. Conditions and timing of metamorphism in the southern Abitibi greenstone belt, Quebec. Canadian Journal of Earth Sciences, 32(6), pp. 787-805.

Redhammer, G. J., Beran, A., Schneider, J., Amthauer, G. & Lottermoser, W. 2000. Spectroscopic and structural properties of synthetic micas on the annite-siderophyllite binary: Synthesis, crystal structure refinement, Mössbauer, and infrared spectroscopy. American Mineralogist, 85(3-4), pp. 449-465.

Roache, T.J., Walshe, J.L., Huntington, J.F., Quigley, M.A., Yang, K., Bil, B.W., Blake, K.L. and Hyvärinen, T., 2011. Epidote–clinozoisite as a hyperspectral tool in exploration for Archean gold. Australian Journal of Earth Sciences, 58(7), pp. 813-822.

Robert, F., 1989. Internal structure of the Cadillac tectonic zone southeast of Val d'Or, Abitibi greenstone belt, Quebec. Canadian Journal of Earth Sciences, 26(12), pp. 2661-2675.

Sansfaçon, R., Grant, M., and Trudel, P., 1987, Géologie de la mine Canadian Malartic -District de Val d'Or, Série des manuscripts bruts - Direction Générale de l'Exploration Géologique et Minérale, MB87-26.

Schodlok, M.C., Whitbourn, L., Huntington, J., Mason, P., Green, A., Berman, M., Coward, D., Connor, P., Wright, W., Jolivet, M. and Martinez, R., 2016. HyLogger-3, a visible to shortwave and thermal infrared reflectance spectrometer system for drill core logging: functional description. Australian Journal of Earth Sciences, 63(8), pp .929-940.

Seedorff, E., Dilles, J.H., Proffett, J.M., Einaudi, M.T., Zurcher, L., Stavast, W.J.A., Johnson, D.A., and Barton, M.D., 2005, Porphyry Deposits: Characteristics and Origin of

Hypogene Features, in Hedenquist, J.W., Thompson, J.F.H., Goldfarb, R.J., and Richards, J.P. eds., Economic Geology 100th Anniversary Volume, Society of Economic Geologists, pp. 251–298.

Selby, D., & Nesbitt, B. E. 2000. Chemical composition of biotite from the Casino porphyry Cu–Au–Mo mineralization, Yukon, Canada: evaluation of magmatic and hydrothermal fluid chemistry. Chemical Geology, 171(1), pp. 77-93.

Sillitoe, R.H., 1973. The tops and bottoms of porphyry copper deposits. Economic Geology, 68(6), pp.799-815.

Sillitoe, R.H., 2010. Porphyry copper systems. Economic geology, 105(1), pp.3-41.

Singer, D.A., Berger, V.I., and Moring, B.C., 2008, Porphyry copper deposits of the world: Database and grade and tonnage models: U.S. Geological Survey Open-File Report 2008−1155.

Speta, M., Gingras, M.K. and Rivard, B., 2016. Shortwave infrared hyperspectral imaging: A novel method for enhancing the visibility of sedimentary and biogenic features in oil-saturated core. Journal of Sedimentary Research, 86(7), pp. 830-842.

Speta, M., Rivard, B., Feng, J., Lipsett, M. and Gingras, M., 2015. Hyperspectral Imaging for the Determination of Bitumen Content in Athabasca Oil Sands Core Samples. AAPG Bulletin, 99(7), pp. 1245-1259.

Sun, Y., Seccombe, P. K., & Yang, K. 2001. Application of short-wave infrared spectroscopy to define alteration zones associated with the Elura zinc–lead–silver deposit, NSW, Australia. Journal of Geochemical Exploration, 73(1), 11-26.

Swayze, G.A., Clark, R.N., Goetz, A.F., Livo, K.E., Breit, G.N., Kruse, F.A., Sutley, S.J., Snee, L.W., Lowers, H.A., Post, J.L. and Stoffregen, R.E., 2014. Mapping advanced argillic alteration at Cuprite, Nevada, using imaging spectroscopy. Economic Geology, 109(5), pp.1179-1221.

Tappert, M., Rivard, B., Giles, D., Tappert, R. and Mauger, A., 2011. Automated drill core logging using visible and near-infrared reflectance spectroscopy: a case study from the Olympic Dam IOCG deposit, South Australia. Economic Geology, 106(2), pp. 289-296.

Tappert, M.C., Rivard, B., Fulop, A., Rogge, D., Feng, J., Tappert, R. and Stalder, R., 2015. Characterizing Kimberlite Dilution by Crustal Rocks at the Snap Lake Diamond Mine (Northwest Territories, Canada) using SWIR (1.90–2.36 μ m) and LWIR (8.1–11.1 μ m) Hyperspectral Imagery Collected from Drill Core. Economic Geology, 110(6), pp. 1375-1387.

Taran, M.N., Lebedev, A.S. and Platonov, A.N., 1993. Optical absorption spectroscopy of synthetic tourmalines. Physics and Chemistry of Minerals, 20(3), pp. 209-220.

Taylor, C.E., Ross, M., Perrouty, S., Lypaczewski, P., Rivard, B., Clark, J.R., Linnen, R.L., Olivo, G.R., and Taves, R., 2018. Defining the glacial dispersion of the Canadian

Malartic stockwork-disseminated Au deposit through hyperspectral imaging analysis of surficial clasts. PDAC, Toronto, March 4-7, 2018

Teck Ressources Limited Inc. (2019) Annual Information Form, Vancouver, BC, Canada. Teck Ressources Limited Inc.

Trudel, P., and Sauvé, P., 1992, Synthèse des caractéristiques géologiques des gisements d'or du district de Malartic, Direction Générale de l'Exploration Géologique et Minérale, MM 89-04.

Turner, D., Groat, L.A., Rivard, B. and Belley, P.M., 2017. Reflectance spectroscopy and hyperspectral imaging of sapphire-bearing marble from the Beluga occurrence, Baffin island, Nunavut. The Canadian Mineralogist, 55(4), pp. 787-797.

van den Boomgaard, R., & van der Weij, R. 2001. Gaussian convolutions numerical approximations based on interpolation. In Scale-Space and Morphology in Computer Vision: Third International Conference, Scale-Space 2001 Vancouver, Canada, July 7–8, 2001 Proceedings 3 (pp. 205-214). Springer Berlin Heidelberg.

van der Meer, F., Kopačková, V., Koucká, L., van der Werff, H. M., van Ruitenbeek, F. J., & Bakker, W. H. 2018. Wavelength feature mapping as a proxy to mineral chemistry for investigating geologic systems: An example from the Rodalquilar epithermal system. International journal of applied earth observation and geoinformation, 64, 237-248.

van Rossum, G., Python tutorial, Technical Report CS-R9526, Centrum voor Wiskunde en Informatica (CWI), Amsterdam, May 1995

van Ruitenbeek, F.J., Cudahy, T.J., van der Meer, F.D. and Hale, M., 2012. Characterization of the hydrothermal systems associated with Archean VMS-mineralization at Panorama, Western Australia, using hyperspectral, geochemical and geothermometric data. Ore geology reviews, 45, pp. 33-46.

Van Ruitenbeek, F.J., Debba, P., Van Der Meer, F.D., Cudahy, T., Van Der Meijde, M. and Hale, M., 2006. Mapping white micas and their absorption wavelengths using hyperspectral band ratios. Remote Sensing of Environment, 102(3-4), pp. 211-222.

Vedder, W. 1964 Correlations between infrared spectrum and chemical composition of mica. American Mineralogist, 49, pp. 736–768.

Vogt, C., Lauterjung, J., & Fischer, R. X. 2002. Investigation of the Clay Fraction (< 2µm) of the Clay Minerals Society Reference Clays. Clays and Clay Minerals, 50(3), pp. 388-400.

Wang, R., Cudahy, T., Laukamp, C., Walshe, J.L., Bath, A., Mei, Y., Young, C., Roache, T.J., Jenkins, A., Roberts, M. and Barker, A., 2017. White mica as a hyperspectral tool in exploration for the Sunrise Dam and Kanowna Belle Gold deposits, Western Australia. Economic Geology, 112(5), pp. 1153-1176.

Wells, M., Laukamp, C. and Hancock, E., 2016. Reflectance spectroscopic characterisation of mineral alteration footprints associated with sediment-hosted gold mineralisation at Mt

Olympus (Ashburton Basin, Western Australia). Australian Journal of Earth Sciences, 63(8), pp. 987-1002.

Whalen, J.B., Davis, W.J. and Anderson, R.A., 2017. Temporal and geochemical evolution of the Guichon Creek Batholith and Highland Valley porphyry copper district, British Columbia: Implications for generation and tectonic setting of porphyry systems; Geological Survey of Canada, Open File 8334.

White, A.J., Laukamp, C., Stokes, M.A., Legras, M. and Pejcic, B., 2017. Vibrational spectroscopy of epidote, pumpellyite and prehnite applied to low-grade regional metabasites. Geochemistry: Exploration, Environment, Analysis, 17(4), pp. 315-333.

Wilkinson, J.J., Chang, Z., Cooke, D.R., Baker, M.J., Wilkinson, C.C., Inglis, S., Chen, H. and Gemmell, J.B., 2015. The chlorite proximitor: A new tool for detecting porphyry ore deposits. Journal of Geochemical Exploration, 152, pp.10-26.

Wilkinson, L., Cruden, A.R., Krogh, T.E., 1999. Timing and kinematics of Timiskaming deformation within the Larder Lake - Cadillac deformation zone, southwest Abitibi greenstone belt, Ontario, Canada. Can. J. Earth Sci. 36 (4), pp. 627–647.

Witt, W.K., Hagemann, S.G., Villanes, C., Vennemann, T., Zwingmann, H., Laukamp, C. and Spangenberg, J.E., 2016. Multiple gold mineralizing styles in the Northern Pataz District, Peru. Economic Geology, 111(2), pp. 355-394.

Appendices

Appendix 1 - Microprobe data (wt %) of biotite and chlorite (Chapter 2)

BIOTITE Crystals Run 2	SiO2	Al2O3	TiO2	V2O3	Cr2O3	MnO	FeO	MgO	CaO	BaO	Na2O	K2O	F	Cl	ZrO2	TOTAL
Bt-8	34.1	15.72	2.42		0.01	0.47	25.39	5.66	0.01		0.07	9.36				93.21
Bt-9	38.33	11.08	2.16		0.02	0.5	16.56	14.2	0.01		0.34	9.62				92.81
Bt-12	37.99	10.97	2.22		0.01	0.88	16.56	13.77	0.01		0.56	9.09				92.06
Bt-13	33.88	15.57	2.63		0.01	0.46	25.26	5.61	0.01		0.09	9.3				92.81
Bt-14	40.36	11.38	1.2		0.01	0.15	8.04	21.16	0		0.46	9.69				92.47
Bt-15	38.64	11.7	1.94		0.01	0.3	12.89	17.3	0.01		0.41	9.5				92.71
Bt-16	38.28	11.03	2.22		0.03	0.88	17.01	13.67	0.01		0.51	9.34				92.96
Phl-1	42.17	12.35	0.09		0	0.01	0.53	27.89	0.01		1.4	8.76				93.21
Phl-2	41.57	11.87	0.29		0	0.07	3.03	25.06	0		0.31	10.22				92.42
Phl-3	39.74	14.11	0.82		0.01	0.05	2.88	24.08	0.01		0.15	10.28				92.13
Phl-5	39.69	13.91	0.86		0.01	0.06	3.44	23.73	0		0.13	10.31				92.14
Phl-6	41.88	11.87	0.26		0.01	0.08	3.17	25.35	0		0.25	10.36				93.22
Phl-7	37.79	15.84	1.09		0.08	0.05	5.84	21.64	0.01		0.61	9.25				92.19
Phl-8	39.67	14.02	0.65		0.01	0.03	2.71	24.73	0		0.29	10.12				92.25
BIOTITE Rocks Run 1	SiO2	Al2O3	TiO2	V2O3	Cr2O3	MnO	FeO	MgO	CaO	BaO	Na2O	K2O	F	Cl	ZrO2	TOTAL
K389048	37.35	16.88	1.68	0.13	0.1	0.25	14.74	13.97	0.02	0.07	0.08	9.5	0.35	0	0	95.13
K389084	36.5	17.24	1.61	0.07	0.14	0.25	17.92	11.94	0.07	0.06	0.13	8.99	0.27	0	0	95.21
K389056	40.42	16.7	1.52	0.06	0.02	0.09	9.92	14.73	0.03	0.31	0.08	10	0.4	0.01	0	94.28
K389090	36.34	16.8	1.94	0.07	0.11	0.21	17	12.15	0.03	0.34	0.09	9.19	0.21	0	0	94.48
K389203	43.95	13	0.71	0.06	0.03	0.09	3.93	21.14	0.03	0.05	0.07	10.6	1.96	0	0	95.63
K389202	41.71	13.35	0.8	0.05	0.13	0.09	3.71	22.96	0.07	0.05	0.06	9.92	1.79	0	0	94.68
K389208	37.15	16.41	1.95	0.04	0.06	0.26	16.53	12.55	0.03	0.04	0.04	9.58	0.39	0.01	0	95.04
P0111	39.07	15.75	1.63	0.1	0.06	0.22	11.09	16.61	0.01	0.02	0.05	10.04	0.76	0	0	95.41
P0122	40.57	15.84	1.1	0.06	0.34	0.06	4.99	20.74	0.02	0.02	0.06	10.13	0.38	0	0	94.31
P0906	40.05	15.56	1.21	0.11	0.12	0.18	7.69	19.09	0.02	0.03	0.06	10.4	1.29	0	0	95.83
P0907	38.94	15.56	1.48	0.09	0.09	0.16	10.19	17.51	0.02	0.06	0.07	10.12	1.08	0	0	95.37
CHLORITE Run 2	SiO2	Al2O3	TiO2	V2O3	Cr2O3	MnO	FeO	MgO	CaO	BaO	Na2O	K2O	F	Cl	ZrO2	TOTAL
Chl-1	30.67	16.89	0.03		0.12	0.09	6.39	30.46	0.01		0.01	0.01				84.67
Chl-2	22.1	20.74	0.06		0.03	0.08	37.38	4.59	0.01		0.01	0.01				85.01
Chl-5	26.35	22.79	0.05		0.01	0.02	13.63	22.05	0.02		0.01	0.03				84.96
Chl-7	25.15	22.93	0.06		0.02	0.22	17.25	19.22	0.01		0	0				84.86
Chl-9	25.05	22.96	0.04		0.01	0.23	17.55	18.77	0.01		0.01	0.01				84.64
Chl-10	24.81	23.67	0.03		0.01	1.31	18.57	16.1	0.01		0	0				84.51
Chl-11	29.71	19.06	0.07		0.08	0.04	4.67	31.09	0.01		0.01	0				84.73
CHLORITE Run 1	SiO2	Al2O3	TiO2	V2O3	Cr2O3	MnO	FeO	MgO	CaO	BaO	Na2O	K2O	F	Cl	ZrO2	TOTAL
Chl-16	34.67	11.98	0.02		0.02	0.04	3.21	36.34	0.02		0.01	0				86.33
CHLORITE Run 0	SiO2	Al2O3	TiO2	V2O3	Cr2O3	MnO	FeO	MgO	CaO	BaO	Na2O	K2O	F	Cl	ZrO2	TOTAL
Cca-2	29.85	22.56	0.02			0.01	1.53	30.92	0.01		0.01	0.02				84.93
Seraphinite	34.4	13.04	0.02			0.01	2.84	34.31	0.01		0.01	0.01				84.65
Basalt_L	25.72	19.68	0.04			0.41	28.03	14.26	0.05		0.03	0.01				88.23
M10573	21.8	22.5	0.95			0.04	40.14	2.71	0.03		0.01	0				88.19
M-1391-1790	28.98	18.68	0.03			0.13	14.43	24.56	0.16		0.02	0.07				87.06
M-1391-1950	30.01	17.63	0.03			0.09	13.57	25.22	0.05		0.01	0.03				86.65
M-1771-0269	28.52	17.89	0.02			0.21	19.17	21.57	0.1		0.02	0.02				87.54
M-1771-0270	28.68	17.89	0.02			0.22	19.3	21.74	0.07		0.01	0.03				87.97
M-1771-0948	27.29	18.67	0.11			0.26	23.85	17.23	0.04		0.02	0.08				87.55
M-1771-1115	27.77	17.68	0.12			0.25	24.54	17.07	0.04		0.03	0.1				87.6
Pn1975	25.16	20.96	0.07			0.35	28.59	12.57	0.05		0.01	0.02				87.77
Pn1990	27.04	21.3	0.07			0.21	15.94	21.69	0.03		0	0.05				86.33
Pn1450	24.79	21.35	0.09			0.3	29.68	11.94	0.03		0.01	0.01				88.21

Appendix 2A – Photographs and spectral imagery of additional samples from Canadian Malartic (Chapter 3)

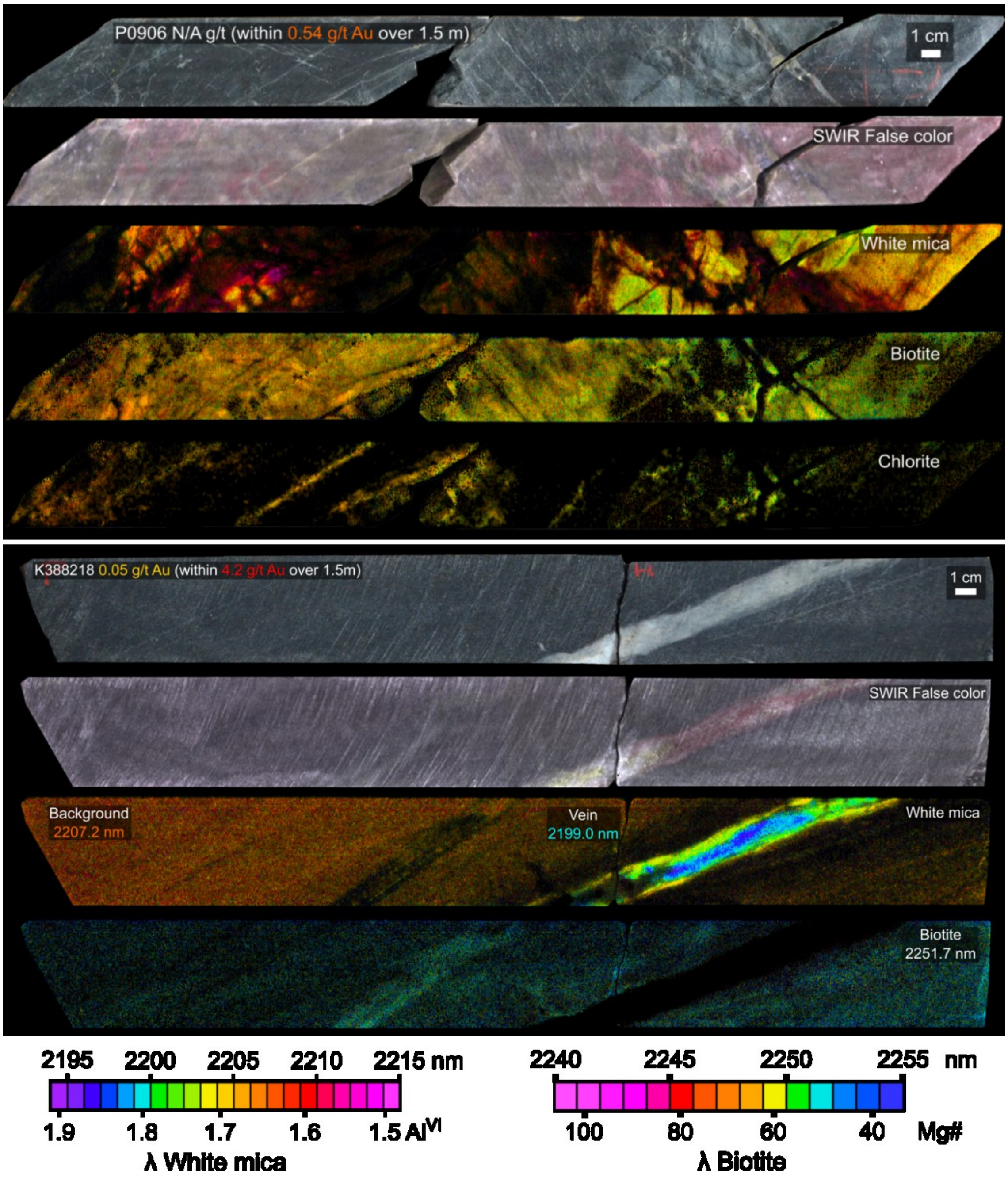

Appendix 2A.1) Top: P906 is a typical sample from the distal alteration zone, with texturally complex white mica composition varying from 2203 nm to 2212 nm. **Bottom**: K388218 is from the distal alteration zone, showing a homogeneous phengitic (2207 nm) background, cut by a late quartz vein with Al-rich white mica (2199 nm). Biotite composition is undistinguishable from background (2251.7 nm).

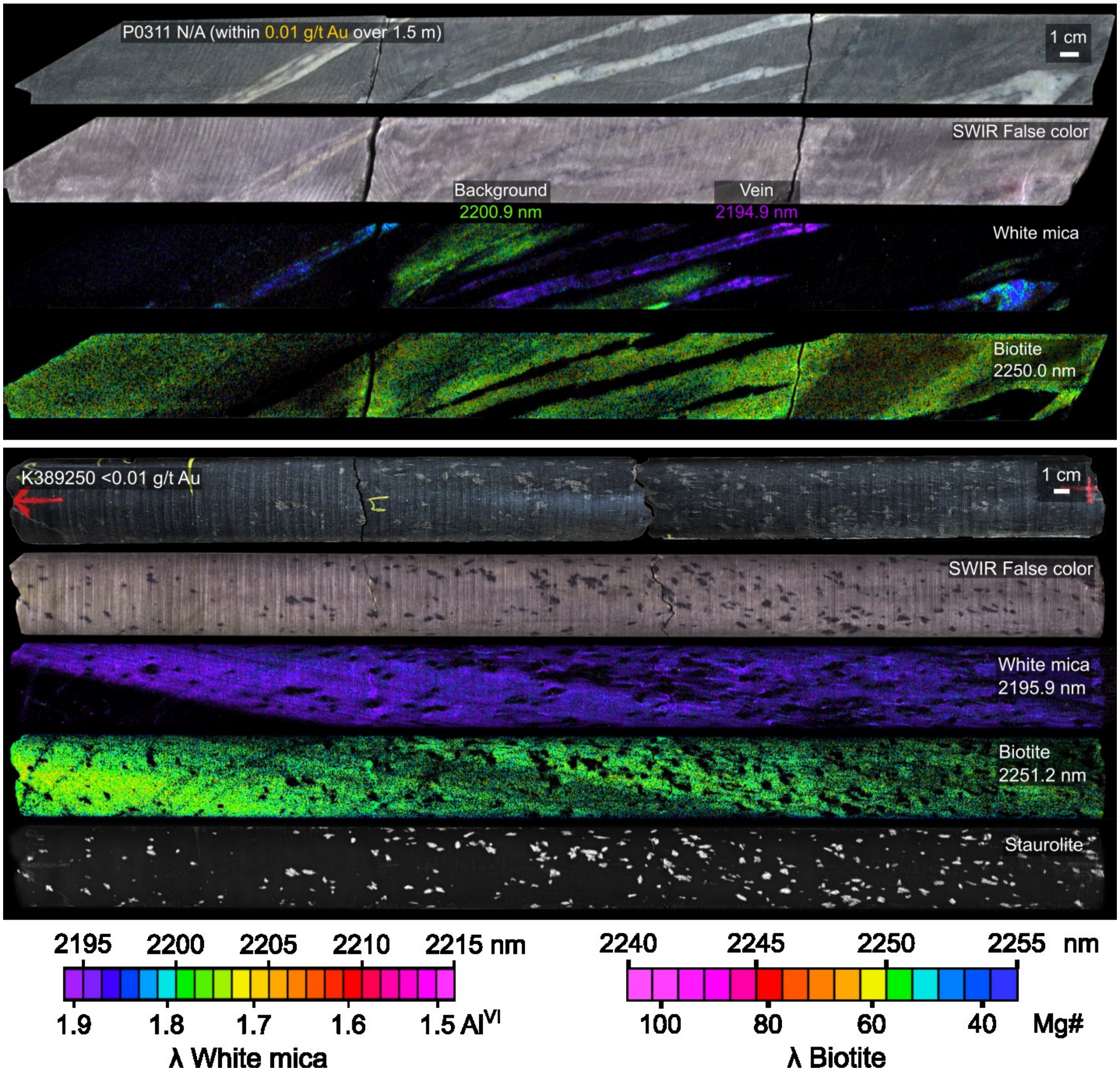

Appendix 2A.2) Top: Sample P311 is an unaltered sample, with background Al-rich white mica (2201 nm) cut by late quartz veins with Al-rich white mica (2195 nm). **Bottom**: K389250 is a distal sample (3 km) showing metamorphic Al-rich white mica (2196 nm) in most sedimentary layers (except far left side), and cm-sized staurolite crystals.

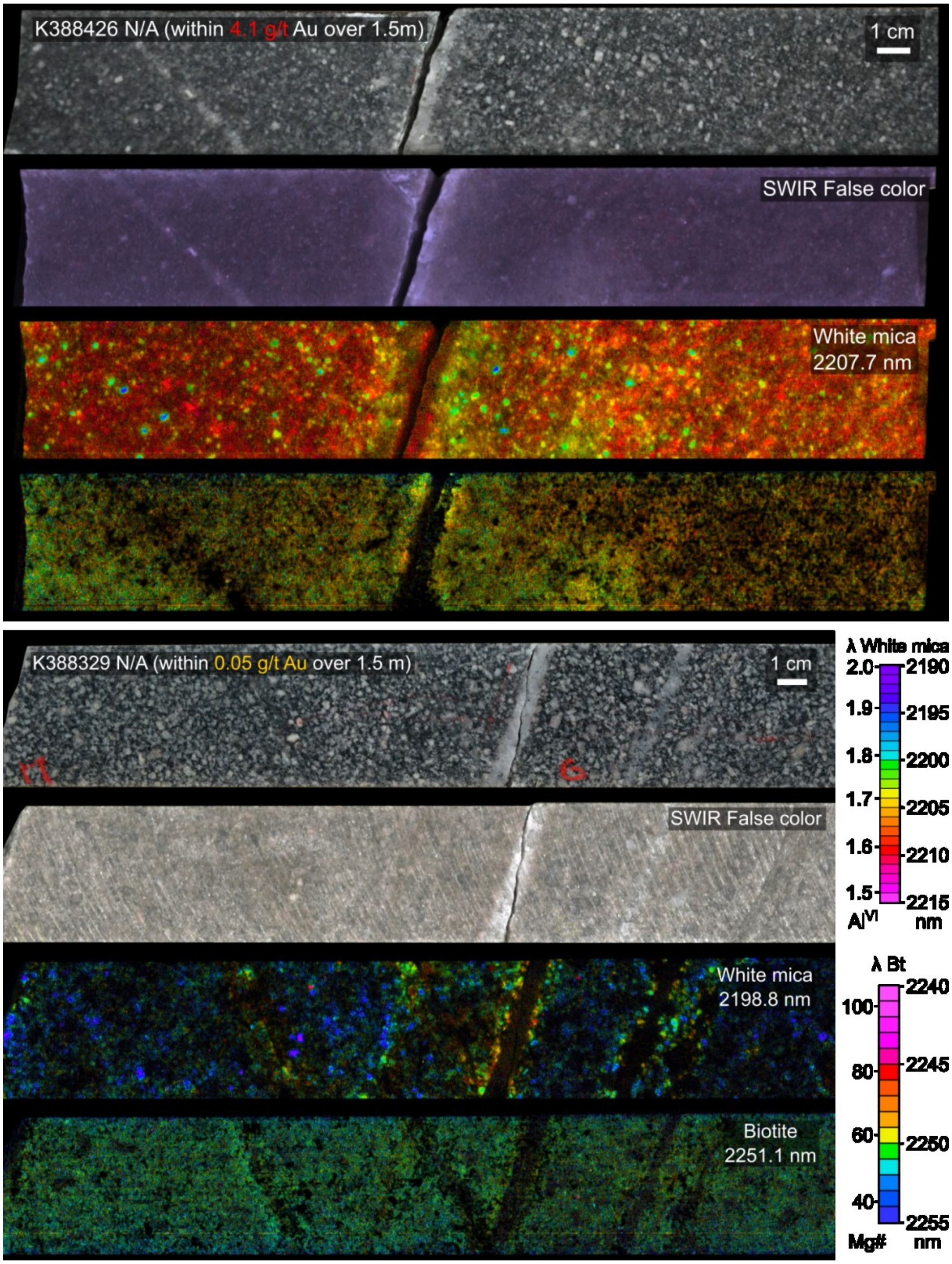

Appendix 2A.3) Top: K388426 is a strongly altered intrusive rock (quartz monzodiorite), with phengitic white mica (2208 nm) in the groundmass, and Al-rich white mica (2198 nm) in large feldspar phenocrysts. **Bottom**: K388329 is a weakly altered to unaltered equivalent quartz monzodiorite showing Al-rich (2199 nm) groundmass white mica, with phengitic alteration along quartz veins.

Appendix 2B - Spectral imagery of additional drill holes from Canadian Malartic

(Chapter 3)

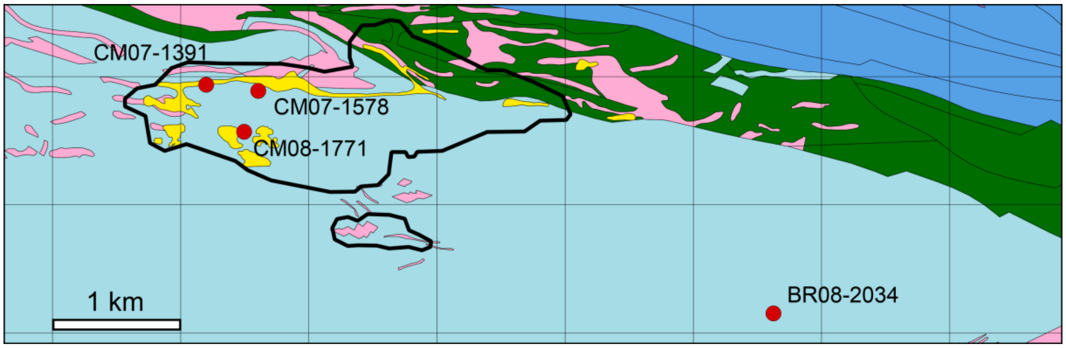

Appendix 2B.1) Map indicating the location of the drill holes presented in Appendix B.2-4 and in Figure 3-7 of the paper (CM07-1391).

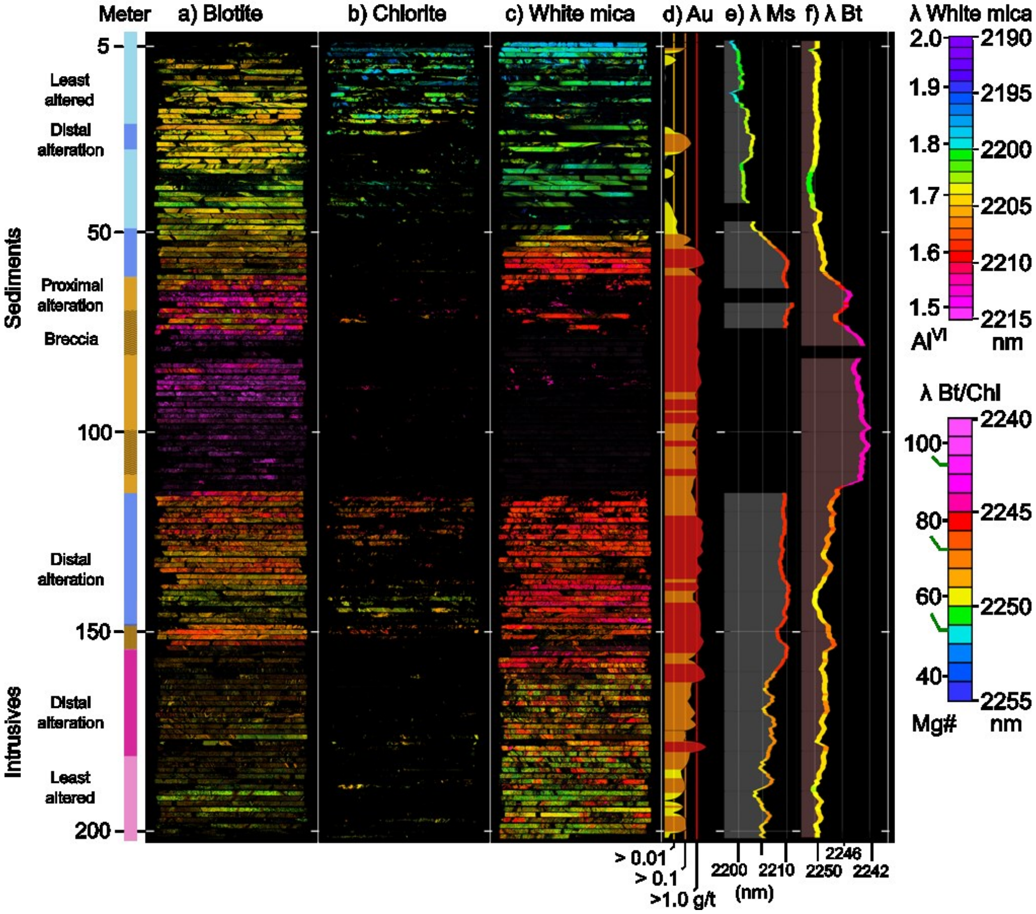

Appendix 2B.2) DDH CM07-1578 is from a similar location to CM07-1391 (Figure 3-7, location indicated on map above), depicting the typical hydrothermal alteration zonation adjacent to the Sladen fault.

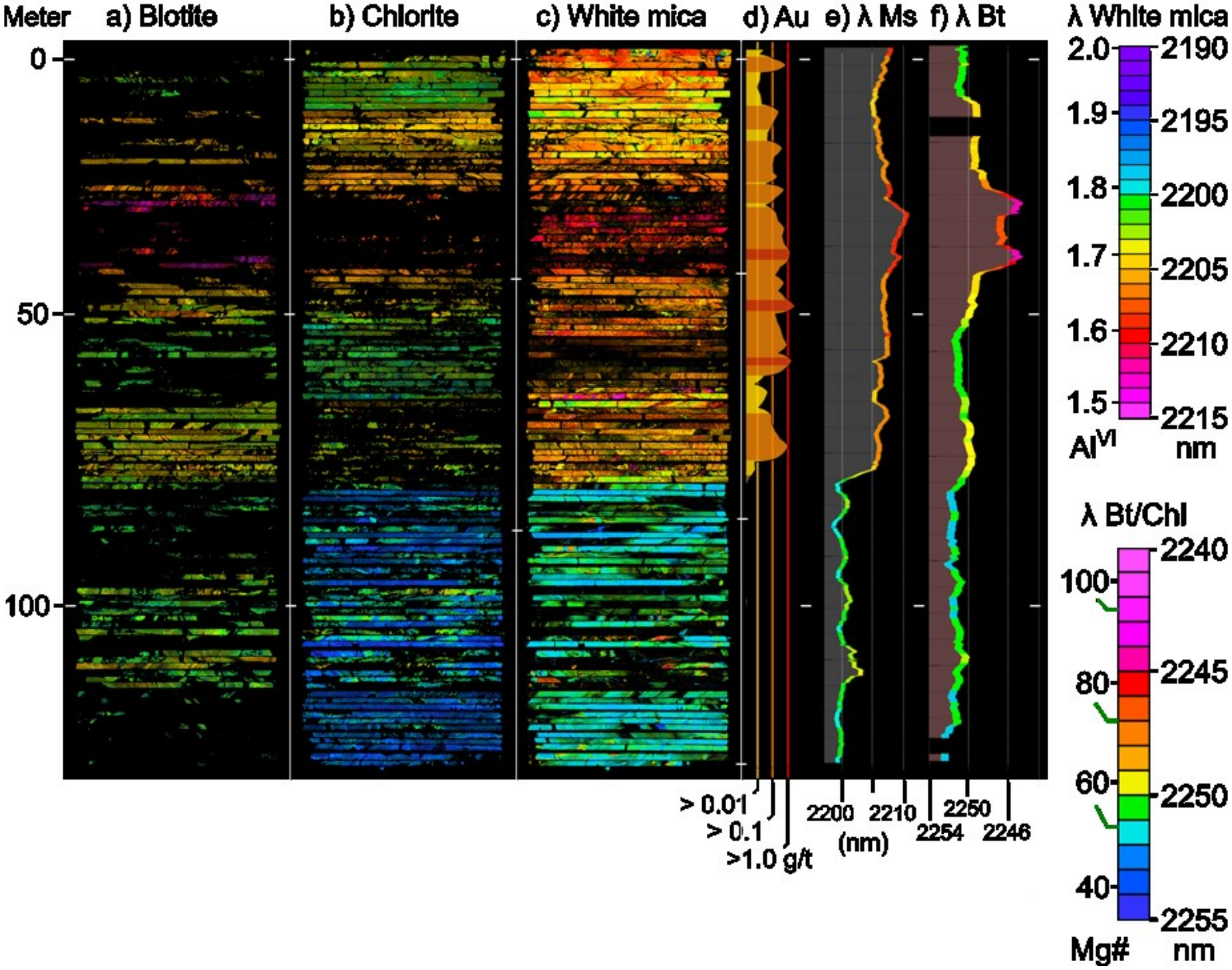

Appendix 2B.3) DDH CM08-1771 is from the NW-SE deformation zone (Gaillard et al., 2018), an additional mineralized area within the open pit.

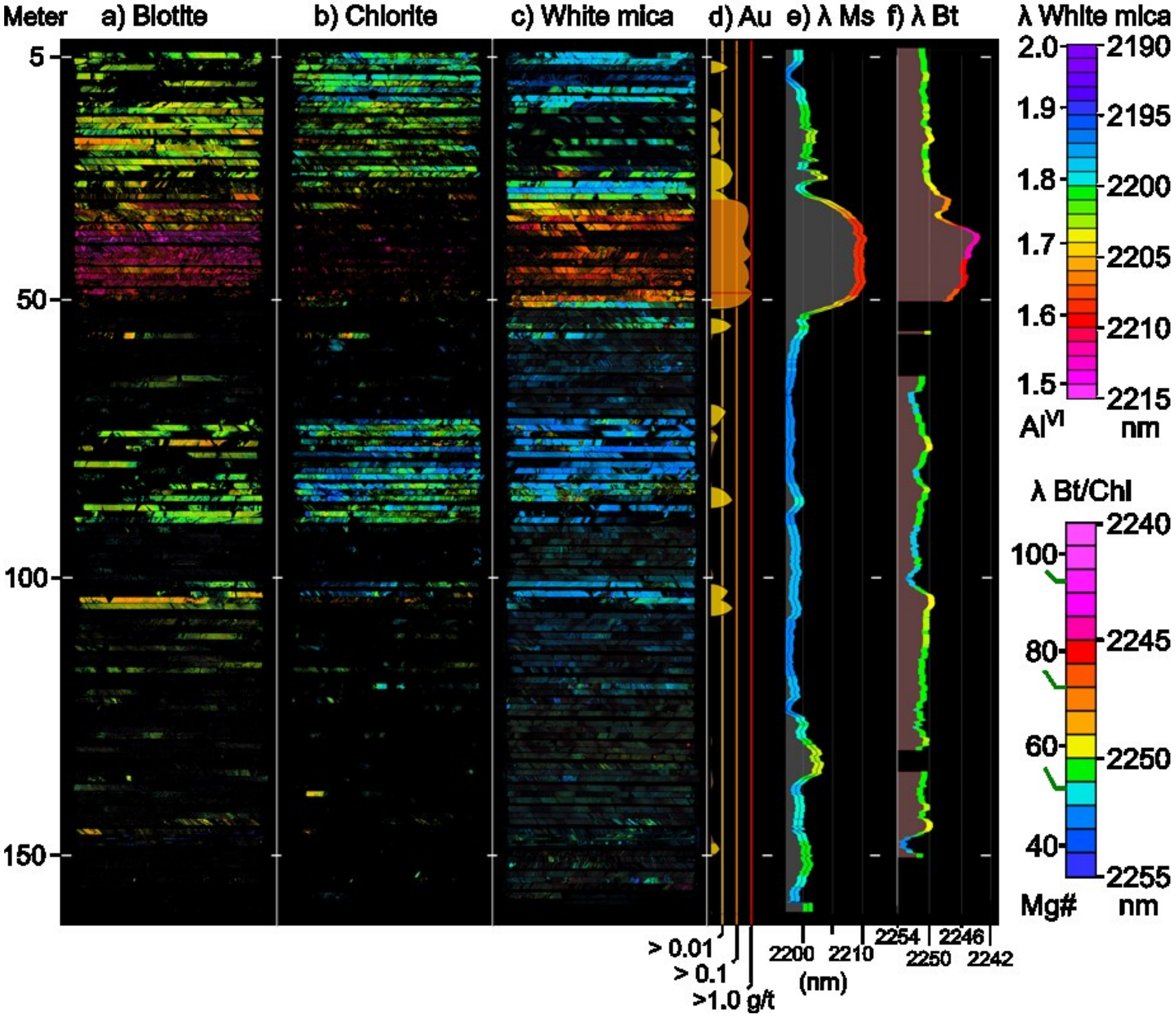

Appendix 2B.4) DDH BR08-2034 is from a weakly mineralized zone, 3 km SW of the open pit. This drill hole shows hydrothermal alteration patterns (Mg-rich biotite, phengite) similar to those at Canadian Malartic, but limited to a narrow, 20 m wide zone.

Appendix 3 - Imagery of additional samples from Highland Valley (Chapter 4)

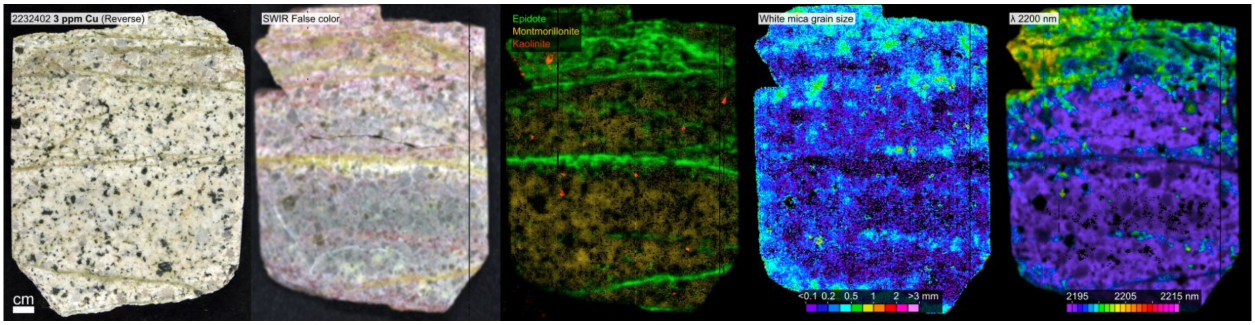

Appendix 3A: Sample 2232402, montmorillonite-rich matrix

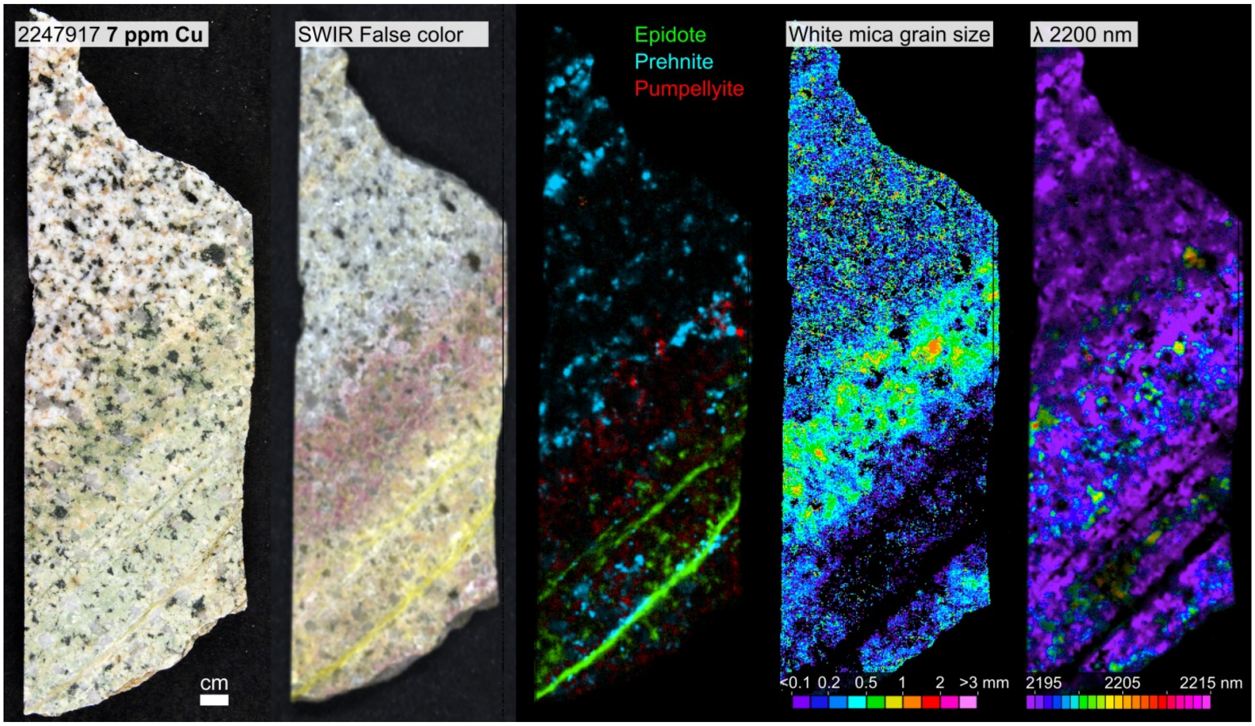

Appendix 3B: Sample 2247917, pumpellyite-rich zone

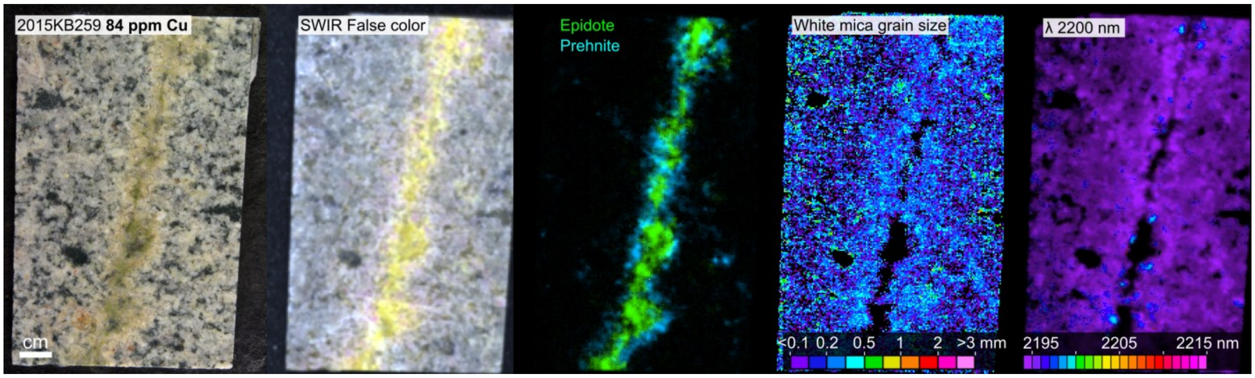

Appendix 3C: Sample 2015KB249, epidote vein with prehnite selvage

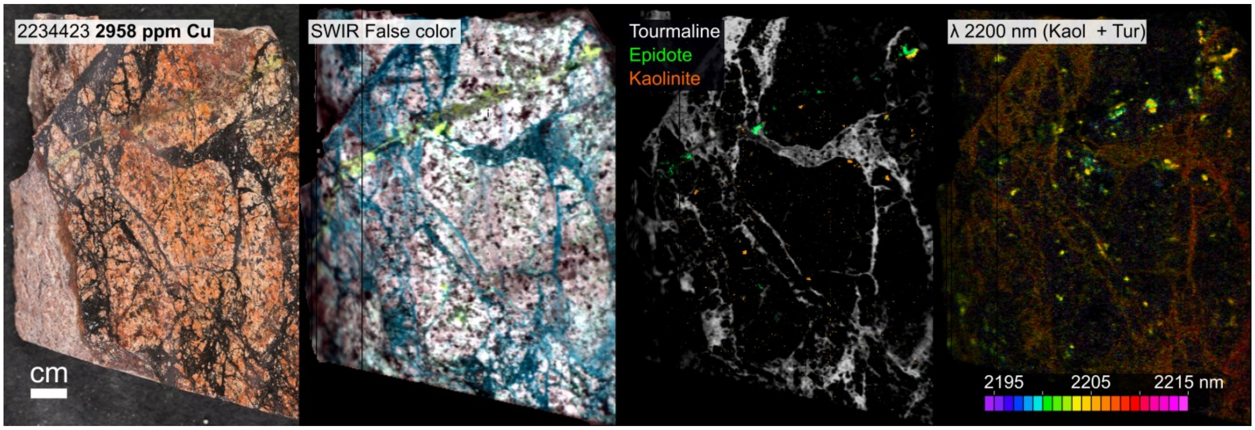

Appendix 3D: Sample 2234423, tourmaline breccia.